Inger Helen Khateeb

Event-Related Functional Magnetic Resonance Imaging (fMRI) of the Brain:

Models and Estimation of the Haemodynamic BOLD Response

Section for Medical Image Analysis and Informatics
Department of Physiology

Årstadveien 19, N-5009 Bergen, Norway

&

Department of Informatics

N-5020 Bergen, Norway

University of Bergen

Acknowledgments

This interdisciplinary work was carried out at the Section for Medical Image Analysis and Informatics, Department of Physiology, and the Department of Informatics at the University of Bergen.

Many people deserve thanks for their support and help during the work of this thesis. I would like to express my sincere gratitude to my supervisor Arvid Lundervold at the Section for Medical Image Analysis and Informatics. It is a pleasure to recognize his help and advice throughout the course of this study. His guidance and understanding are greatly appreciated. I thank him for introducing me to the fascinating field of medical imaging, giving me an opportunity to combine my background as a physiotherapist with the field of medical informatics.

I would also like to thank my co-supervisor Trond Steihaug, Department of Informatics, for his help and for many enlightening discussions, especially during the final stages of this project.

I am thankful to all members of the Bergen fMRI group for accepting me into their group. It has been a pleasure to work in such a multidisciplinary setting.

Finally, with all my heart, I owe more than I can express to my husband Akef for his patience and continuous encouragement. Without his positive attitude, this work would never have come to a completion. I thank my four wonderful children, Ahmed, Marie, Nadia and Josef. Their help and understanding during my long working hours the last 18 months are deeply appreciated. I hope that they will never stop asking "why" - in the words of Mahatma Gandhi: "Live as if your were to die tomorrow. Learn as if you were to live forever".
I also thank my highly loved parents for always having believed in me and for all their encouragement during difficult times.

Bergen, June 2001
Inger Helen Khateeb

Summary

Functional Magnetic Resonance Imaging (fMRI) produces brain images that reflect neuronal activity due to sensory, cognitive or motor tasks. *Event-related fMRI* is a technique for detection of neurovascular responses to very *brief*, randomly intermixed, stimuli and somato-sensory or cognitive events.

fMRI techniques depends upon the magnetic properties of oxygenated/deoxygenated blood as a source of contrast, the so called *Blood Oxygenation Level Dependent, BOLD-response*. The sensitivity of this contrast is such that experiments can be performed with a temporal resolution on the scale of a few hundreds of milliseconds to seconds, and a spatial resolution of 3 mm or less, in almost all areas of the brain.

Knowledge about the properties of the BOLD response is essential for the understanding of stimulus induced brain activation, e.g. to what extent can the underlying neuronal activation be inferred from its shape. The mechanisms of coupling between neuronal responses and haemodynamics are not well understood, and there is currently no exact model of the BOLD response. Several descriptive and/or physiological approaches have therefore been proposed for the modeling of the BOLD response. This work considers some models for its *detection* and *description* in event-related fMRI. The emphasis is on models for characterization of the evoked BOLD-responses. The signal *description* problem can be formulated in terms of introduction and estimation of physiologically interpretable parameters like *lag* (time to maximum response intensity), *dispersion* (duration of response) and *gain* (response intensity/strength) or vascular *transfer rates* of oxygen between different physiological tissue compartments. Each model's ability to model the BOLD-response in er-fMRI data, with increasing noise levels, have been explored. Experiments have been performed on synthetic as well as real fMRI data. We found the *Nonlinear Least Squares Model*, incorporating simple averaging of time locked single trials combined with Nonlinear Least Squares estimation of Gaussian model parameters, to be well suited for evaluating event-related fMRI data in terms of physiological interpretable parameters. For the Kruggel & Cramon Model [27] we successfully applied the Levenberg Marquardt Method for optimisation in parameter estimation, thereby approximately reducing computation times with a factor of two.

We extracted parameter feature vectors from realisations of single trial response models in order to bring our estimation of physiologically interpretable parameter into a statistical classification framework. By statistical classification of different haemodynamic response types (shapes) it should be possible to distinguish and characterize neural information processing in different brain locations during a given paradigm. Each classified response could then provide information about processing delay, number of neurons in the firing population and duration/asynchrony of firing at that particular brain location via neurovascular mechanisms which yield more information about functional anatomy than simple activation detection. From the experiments on real data, we were able to characterize differential responses in a *word* versus *non-word* discrimination task. To our knowledge, introduction of estimated haemodynamic response parameter feature vectors and discrimination between words and non-words in feature space, have not been reported elsewhere, and opens up for more detailed brain function studies in BOLD fMRI.

Contents

List of Figures

List of Tables

Part I

Introduction

Chapter 1

General Introduction

Tell me where is fancy bred,
Or in the heart or in the mind?
(Shakespeare, 1596, Merchant of Venice)

The human brain is undoubtedly the most fascinating, and yet least understood, organ in the body. By almost any measure the central nervous system is extraordinary. Foremost, we are whatever it is. It is the most complex organ of the body; directly or indirectly it controls almost every body function and all of human behaviour. The brain has been pondered and investigated scientifically more than any other organ, yet its essence remains a mystery. We have a good understanding of its morphology, and many of the physiological properties and functions of the nervous system have been unraveled to an exceptional degree. Yet, if you ask the most brilliant neuroscientist how the brain performs its highest functions, such as perception, thinking, emotion, memory or even sleep, you will find he or she must revert to speculation and philosophy. Such a mystery has an enormous attraction and so one is almost compelled to be curious about the brain. To understand how the brain works is therefore one of the most fundamental and exciting challenges we face.

The brain has, however, not always been held in high regard. The Greek philosopher, Aristotle, thought the heart, not the brain, was the location of both intelligence and thought. Also, the ancient Egyptians did not think much of the brain. In fact, when creating a mummy, the Egyptians scooped out the brain through the nostrils and threw it away whereas the heart and other internal organs were carefully removed and preserved. The prevailing idea in Antiquity was that the soul resided in the brain. Based on Galenius (129-199 a.c) anatomical illustrations and partitions of the function of the soul, the church

formulated the so called cell-doctrine which suggested that mental processes were located in the ventricles of the brain. Common sense and imagination were located in the lateral ventricles, the third ventricle was the seat of reasoning, judgement and thought, while memory was contained in the fourth ventricle [19].

In the 17th century Thomas Willis proposed that various areas of the cortex had specific functions. In the 19th century Franz Josef Gall developed two theories that were to become extremely important; (1) the brain is the seat of all intellectual and moral faculties, and (2) particular activities can be localized to some specific region of the cerebral cortex. The study of brain function have progressed steadily throughout the 20th century. Much of the progress has, however, come as a result of electro-physiological measurements on animals or from the observation and treatment of patients suffering from neurological disorders. It is only during the last decade or so that advanced imaging techniques have allowed extensive studies of healthy human subjects.

Medical imaging produces images of internal structures of the human body to aid in accurate diagnosis. The field of medical imaging dates back to the discovery of X-rays in 1895. The development of this medical field called radiology, grew steadily throughout the 20th century. During the last 3 decades the advent of digital computers and new imaging methods such as ultrasound and *Magnetic Resonance Imaging (MRI)* have combined to create an explosion of diagnostic imaging techniques. Each of these imaging modalities exploits some specific physical or chemical principle to obtain diagnostic information. MRI, considered one of the best diagnostic tools for imaging many types of soft-tissue, has been in widespread clinical use since 1984.

Primarily, MRI is a technique used for producing anatomical images. The observation of biological events such as heart beat or blood flow requires rapid, serial image acquisition. Fast dynamic imaging is also required in *functional Magnetic Resonance Imaging (fMRI)*, an area of research where MRI is used to noninvasively explore both elementary and higher level processes of the brain. Functional neuroimaging techniques such as fMRI are unique in that they provide experimental access to the intact living brain. This enables a large spectrum of studies that previously have been impossible. Functional MRI was first reported in 1991 by Belliveau et al. [3] and has steadily advanced from a purely brain activation mapping tool to a method for dynamically assessing the characteristics of brain function.

The first fMRI experiments explored the use of exogenous contrast agents, and stimulus were generally presented as continuous series of trials intermixed with rest periods. Dur-

ing the last decade, however, fMRI techniques have focused on the magnetic properties of (oxygenated/deoxygenated) blood as a source of contrast (*i.e. Blood Oxygenation Level Dependent, BOLD-contrast*). The sensitivity of this contrast is such that experiments can be performed with a temporal resolution on the scale of a few hundreds of milliseconds to seconds, and a spatial resolution of 3 mm or less, in almost all areas of the brain. These features have recently led to a more resolvable technique called *event-related functional Magnetic Resonance Imaging (er-fMRI)* which is the detection of brain activation to very brief and isolated stimuli or tasks, much like the experimental design used in electrophysiology (ERP). This method was first reported in 1996 [5].

A variety of studies, including visual processing, auditory sound and language processing, speech production and memory function, have been performed using fMRI. Other studies have explored the use of fMRI for clinical applications such as presurgical planning (e.g. identification of areas close to a tumor region which are involved in vital brain functions such as language processing, vision and motor function), exploration of mechanisms underlying Alzheimers disease, schizophrenia and affective disorders, multiple sclerosis, epilepsy, dyslexia, obsessive compulsive disorders, and pain. As a result of its wide area of application, fMRI has become an extremely powerful tool both within the field of neuroscience and in a variety of clinical and academic fields.

The future promises integration of fMRI with other modalities measuring brain activity. A combination of measuring EEG simultaneously with fMRI acquisitions has already been demonstrated. Thus, the excellent spatial resolution of fMRI can be combined with the millisecond temporal resolution of EEG [15].

In current fMRI studies the processing of the data is performed after completion of the scanning session on a computer remote from the MRI system. A complete processing procedure may take several hours. However, with the ever increasing performance of computer technology it should become possible to do "online" fMRI processing. This opens the opportunity to perform fMRI experiments in real time. In such cases the neurologist or psychologist could monitor the patients responses, adapting the stimuli accordingly, with important applications in presurgical planning and cognitive neuroscience.

Several technical factors are important for the use of fMRI to study brain function:

- the speed of the imaging method must be such that the data from the entire brain can be acquired in a time less than the duration of the brain states of interest
- considerable computer power is required for the acquisition, processing and storage of very large data sets.

The field of functional imaging is complex and there is an increasing tendency towards multidisciplinary collaboration at the radiological departments. Physicists, chemists, neuroscientists, psychologists and computer scientists work together with the radiologists on the various aspects concerning the different imaging modalities. Most modern medical imaging techniques are digital, and consequently the different processing steps, such as image acquisition, image reconstruction and image display, are all computer based.

Computer scientists are involved in several areas of medical imaging:

- fundamental and applied research on digital signal processing and imaging systems
- interaction between operator and computer
- noise suppression
- image registration
- geometric modeling
- spatiotemporal data analysis and obtaining solutions to inverse problems
- modeling of physiological phenomena such as blood flow, tissue perfusion, water diffusion, neurovascular responses, neuronal activation and functional connectivity of the brain
- simulation
- visualization

With my background as a physiotherapist, a thesis subject within medical informatics seemed particularly interesting. This thesis covers a number of methods concerning the *detection* and *description* of event-related activation in er-fMRI. For a proper understanding and evaluation of such measurements it is necessary to have the needed insight not only of informatics but also within related areas such as image processing, physiology, neuroscience as well as aspects of technical physics and radiology. This has been a very time consuming endeavour. There is an increasing number of publications dealing with different statistical models for the *detection* of brain activation associated with brief stimuli. However, the majority of investigations have been concerned with localization of brain activation, while much less research has attempted to describe the detailed signal properties and physiological modeling of observed activation. Understanding brain function requires information not only of localization of neuronal activity, but also features that characterize these responses. The main goal for the present work is therefore firstly, to describe how stimulus induced brain activation can be detected, and secondly, attempting to characterize the evoked responses (see Figures 1.1 and 1.2).

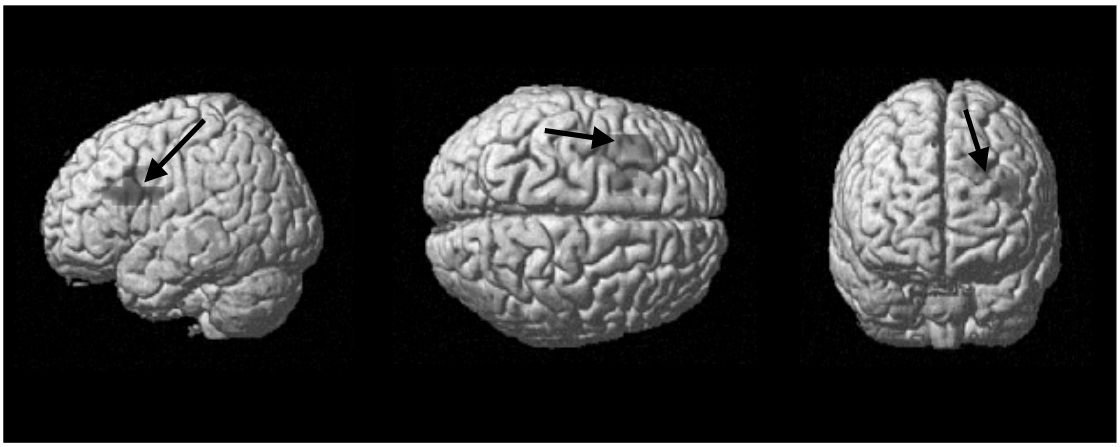

Figure 1.1: Detection of neuronal activation in functional Magnetic Resonance Imaging. Brain activation images relies on the concept that distinct regions "light up" during particular information processing tasks. These images illustrate the localization and (possibly) the degree of activation. To produce such images, statistical methods for detecting activated regions (i.e. voxels) are required.

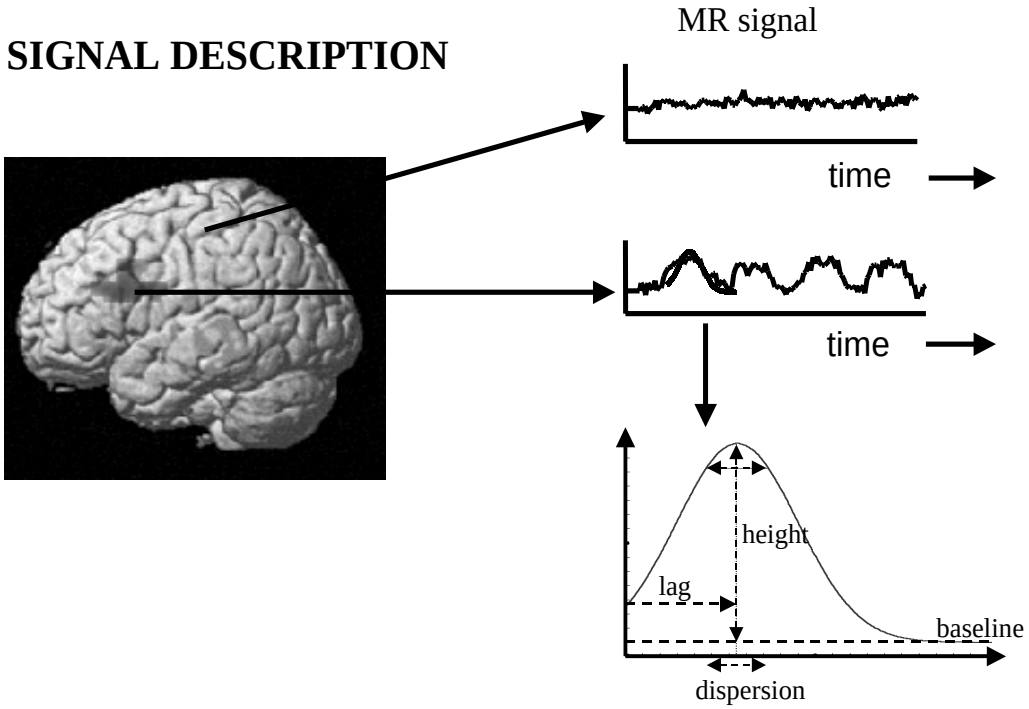

Figure 1.2: Description of neuronal activation in functional Magnetic Resonance Imaging. The neurovascular (haemodynamic) responses are approximated by a modeling function whose characteristics are parameterized.

Chapter 2

Functional Magnetic Resonance Imaging (fMRI) of the Brain

> *For a smart material to be able to send out a more complex signal it needs to be nonlinear. If you hit a tuning fork twice as hard it will ring twice as loud but still at the same frequency. That's a linear response. If you hit a person twice as hard they're unlikely just to shout twice as loud. That property lets you learn more about the person than the tuning fork.*
>
> -Neil Gershenfeld, When Things Start to Think,1999

MRI stands for Magnetic Resonance Imaging, originally called Nuclear Magnetic Resonance Imaging, first described by Purcell and Bloch in 1946 [4]. More than 40 years earlier Roentgen had discovered X-rays which was to play an important role in modern medicine. Over the years a number of imaging techniques have been developed:

- Magnetic Resonance Imaging (MRI)
- Single Photon Emission Computed Tomography (SPECT)
- Positron Emission computed Tomography (PET)
- Ultrasound
- Computerized Topography (CT / CAT)

X-rays, CT and MRI are primarily structural imaging techniques, whereas *functional* MRI, SPECT and PET are capable of detecting biochemical and physiological processes in the brain. Magnetic Resonance Imaging (MRI) is a relatively new neuro-imaging technique. The necessary technology was first available in the late seventies, but it was not until

1981 that MRI was introduced in clinical medicine. Over the last 10-12 years techniques that enable non-invasive whole brain measurement of physiological processes have been developed. These methods are known as *functional* MRI [34]. One exciting area in fMRI is *event-related* fMRI, which involves the development and application of methods based on the transient neuronal changes associated with individual cognitive, sensory and/or motor events [7].

The remainder of this chapter is organized as follows. The next section introduces the concept of digital images after which we give a short description of the general principles in MRI. Knowledge about basic MRI physics is important for the understanding of the methods applied in this thesis. Readers that are familiar with the MRI technique may skip this section. Finally, preprocessing of MRI-data will be briefly discussed before a section on functional MRI concludes the chapter.

2.1 Digital Images

Digital images can be viewed as arrays of grey values in which each array element represents one point in the image. Array elements of two-dimensional images are called *pixels* whereas *voxels* denote the volume elements in 3D. Digital volumetric images are stacks of 2-dimensional image arrays. A 2D array that is a part of a 3D image is called a *slice*. Slices in 3D images can be viewed in all of the 3 orthogonal directions, regardless of the orientation in which they originally were acquired (see Figure 2.1).

Indexing the rows and columns within each slice allows each voxel to be associated with a unique address. More formally, a volumetric image is the set of addresses:

$$\{(x, y, z) \mid 0 \leq x \leq nslices, 0 \leq y \leq nrows, 0 \leq z \leq ncolumns\}$$

where nslices, nrows and ncolumns denotes the number of slices, rows and columns, respectively [30]. An n-dimensional digital image can be viewed as a mathematical function

$$f : D_f \rightarrow V$$

in which D is a rectangular n-dimensional grid and V is a set of intensity (or grey-level) values (see Figure 2.2).

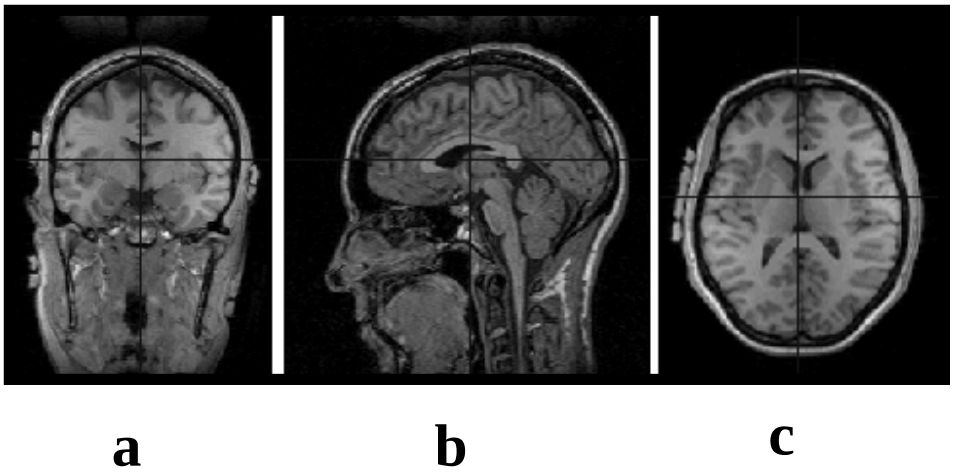

Figure 2.1: Cross-sections of MR image of the author. (a) coronal (vertical) slices, (b) sagittal (vertical) slices and (c) axial (horizontal) slices

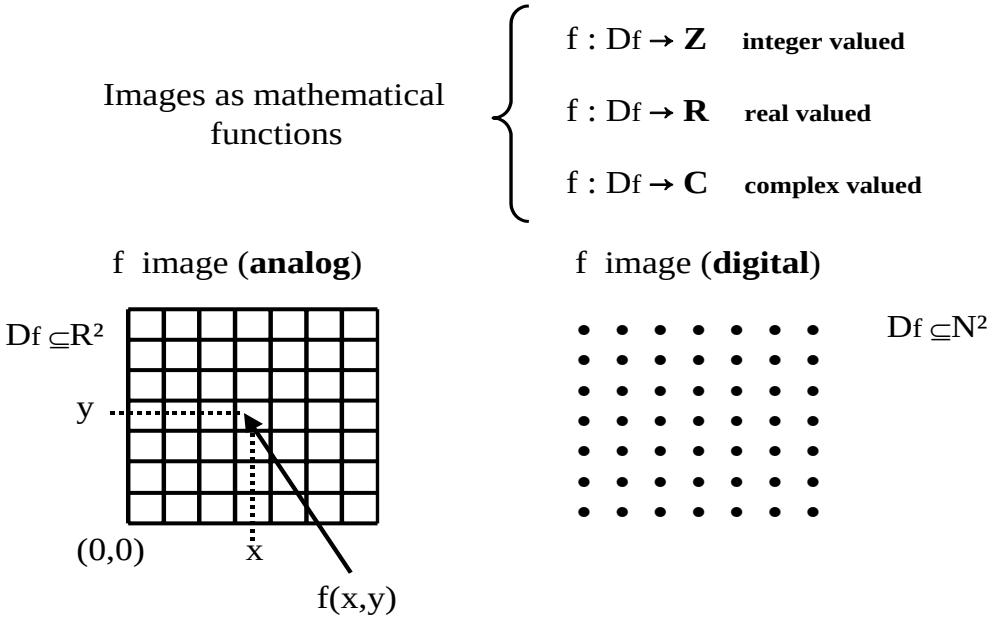

Figure 2.2: Images as mathematical functions. Images can be constructed from integer valued, real valued or complex valued array elements. In fMRI we have $D_f \subseteq N^3(\text{space}) \times N(\text{time})$. Modified from A. Lundervold 2000

2.2 Basic principles of MRI

In every form of X-ray imaging, a beam of X-rays passes through the body which itself becomes a source of secondary X-rays. The contrast between body parts in X-ray imaging is produced by the different scattering and absorption of X-rays by bones and tissues. A major limitation is, however, that exposure of body cells and tissue to large doses of X-rays constitutes a potential health hazard. In MRI we deal with much lower energies than in X-rays or even in visible light [21], and it is the body itself that generates the signals that is the basis for the image acquisition. In a simple way, MRI is an interaction between an external magnetic field, radio waves and nuclei in the body. Before explaining the imaging performed by MRI a few important phenomena, such as magnetization of the body, radio frequency excitation, and measurement of relaxation, need to be explained.

2.2.1 The Hydrogen Nucleus

Of all atoms in the body it is the hydrogen atom that produces the strongest MR signal. Hydrogen is also abundantly present in all body tissues. The hydrogen nucleus has one single spinning positively charged proton. The spin induces a magnetic field, in other words a small magnet is produced. Each nucleus thus have a magnetic moment, i.e. it has both intensity and direction(see Figure 2.3).

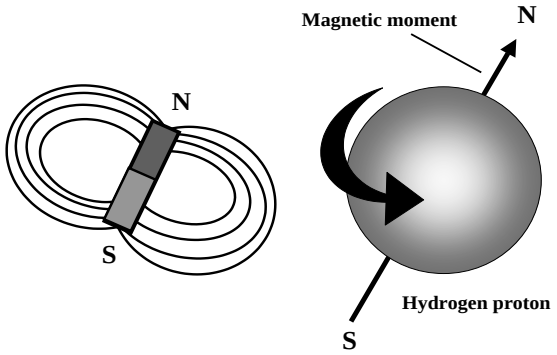

Figure 2.3: Magnetic moment of hydrogen nucleus. The spinning proton generates a small magnetic field.

Under normal circumstances the magnetic moments of hydrogen nuclei within the body are randomly oriented. If placed in a strong magnetic field (B_0), however, a weak (statistical)

alignment of proton spins will occur in the direction of B_0, while a (slightly) smaller number will align in the opposite direction (the "diamagnetic" contribution). Thus, there will be a slight net proton spin magnetization parallel to B_0 (net magnetization vector - $\mathbf{M}(\mathbf{r}, t)$ as a function of localization, $\mathbf{r}$ and time, t (see Figure 2.4)).

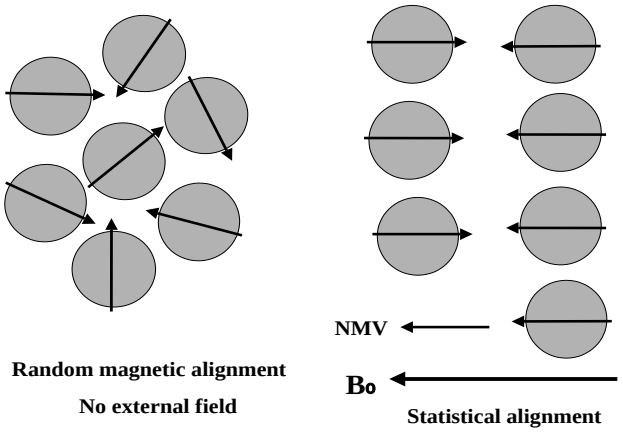

Figure 2.4: Spinning protons in a polarizing magnetic field. With no magnetic external field, the spinning direction is random and no net magnetization is produced (left). When placed in an external magnetic field, the spinning protons line up in a parallel or anti-parallel position (right). NMV = Net Magnetization Vector

Larmor Equation

Placed in an external magnetic field B_0, the protons not only rotates about their individual axes, but "wobbles" also around the direction of B_0 (see Figure 2.5). The frequency of this wobbling or precession is given by the Larmor equation:

$$\omega = \gamma B_0$$

where γ is the gyro-magnetic ratio, B_0 the external magnetic field and ω the Larmor frequency. The gyro-magnetic ratio is a material constant expressed by MHz/T (mega-Hertz per Tesla).

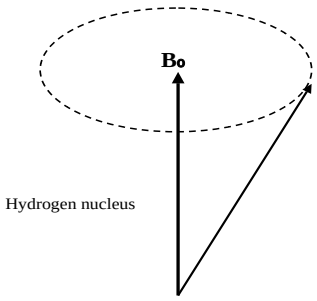

Figure 2.5: Proton precession. Spinning Protons "wobbles" around the direction of the external magnetic field

2.2.2 Resonance

If a hydrogen nuclei in the magnetic field B_0 is exposed to radio frequency radiation, RF (by convention called the B_1 field) at the Larmor frequency, the nuclei will "jump" into a higher energy state. This causes the net magnetization to spiral away from the B_0 field and into the transverse plane. It is in this position that the net magnetization can be detected in MRI. The orientation of the coordinate system of the MRI scanner in relation to the magnetic fields is depicted in Figure 2.6.

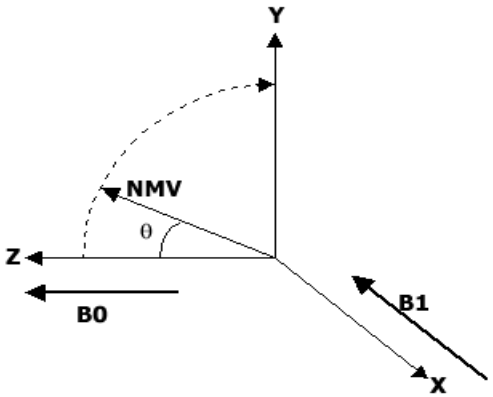

Figure 2.6: Orientation of coordinate system of the MRI scanner and magnetic fields. θ if the flip angle and NMV is the Net Magnetization Vector, $\mathbf{M}(\mathbf{r}, t)$.

The application of an RF-pulse that causes resonance is called excitation. The angle θ is the so called *flip angle*, and its magnitude depends on the amplitude and duration of the RF-pulse. Another result of the RF-pulse is that the magnetic moments of the nuclei within the transverse plane move in such a way that they are *in phase* with each other, i.e

they become synchronized. A receiver coil placed in an area with excitated in-phase nuclei, will receive a signal whenever the in-phase magnetization cuts the coil.

2.2.3 Imaging hardware

The MRI scanner consists of four components : the magnet, gradient coils, radio frequency transmitter and a computer. The magnet is of course the most important component of the equipment. Strong magnetic fields are required to produce good MR images. There are basically two ways of obtaining the required magnetic field, either by using a permanent magnet or an electromagnet. The last method is used for all scanners with a field strength above 0.5 Tesla. In addition to the coils that produce the main magnetic field, B_0, there are other coils that induce smaller magnetic fields, which are gradient coils for producing a gradient field (in B_0) in the X, Y, and Z directions. Within the gradient coils there is also the RF coil which produces the B_1 magnetic field. Finally, the computer controls all components of the scanner and the operator gives input to the computer through a control console. Figure 2.7 gives a schematic view of a MRI scanner.

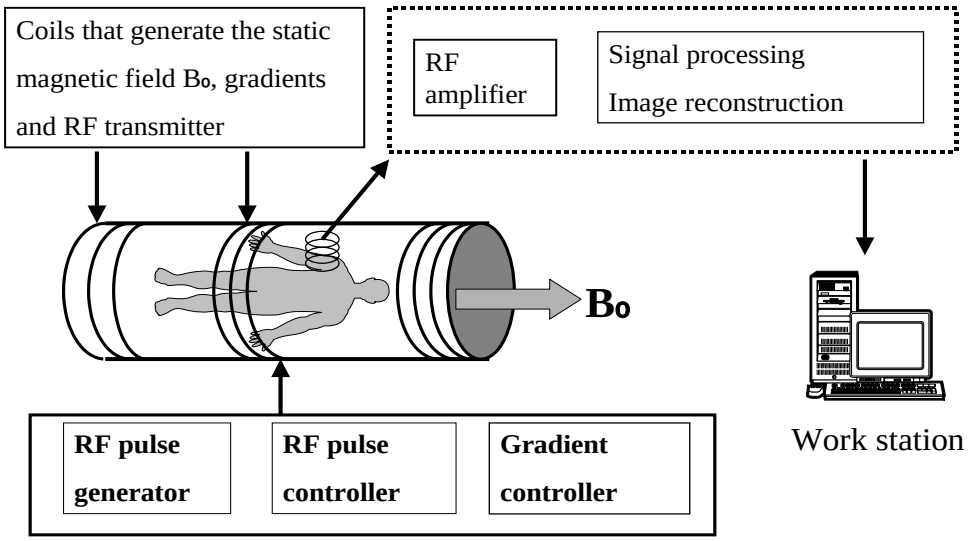

Figure 2.7: Schematic view of a MRI scanner

2.2.4 Gradients

The gradient coils produce the gradients in the B_0 magnetic field. A gradient is simply a magnetic field that changes, usually linearly, from point to point. Gradients in the magnetic field causes each of the regions of spin to experience a unique magnetic field, determining their position in the image. The symbols of the magnetic field gradient in the z, y, and x directions are G_z, G_y, and G_x. The three gradients are referred to as :

1. the **slice select** gradient
2. the **phase encoding** gradient
3. the **frequency encoding** gradient

In the following G_z refers to the slice select gradient, G_y to the phase encoding gradient, and G_x to the frequency encoding gradient. This will result in a tranverse view of the object. A unique property of MRI is, however, that the G_y and G_x also can be employed to select a slice, thereby producing images from other angles, including oblique views.

Slice selection

Slice selection is the excitation of spinning nuclei in a plane through the object. When the slice encoding gradient is switched on, the magnetic field strength is altered in a linear way such that each point along the z-axis has a specific precessional frequency. A slice can then be selected by transmitting an RF pulse with a bandwidth coincident with the Larmor frequency of a particular slice. The slice select gradient, G_z, is turned on during the period that the RF pulse is applied. The thickness of an image slice is determined by the range of frequencies (bandwidth) of the RF pulse.

Spatial encoding

After selecting a slice, we need to know how much signal comes from each voxel (volume element) in the slice. This is accomplished with frequency and phase encoding. We begin to locate the signal along the X-axis. By switching on the frequency encoding gradient a linear frequency difference along the X-axis occurs. We can now locate a signal along the axis according to its frequency. The frequency encoding gradient is switched on when the signal is received. We now need to perform the phase encoding which is the localization of the signal along the remaining y-axis. As with the frequency encoding gradient, the magnetic field strength along the axis of the gradient is altered when the phase encoding gradient is turned on. The gradient G_y is turned on for a short period prior to signal measurement.

The precessing protons which were phase-locked by the RF pulse now change their phase according to their position along the y-axis. When G_y is turned off, the protons are no longer in phase, see Figure 2.8. This procedure is repeated for as many times as there are rows in the image. The size of the spatial encoding area of the image is denoted *Field of View* (FOV), and is usually measured in mm^2.

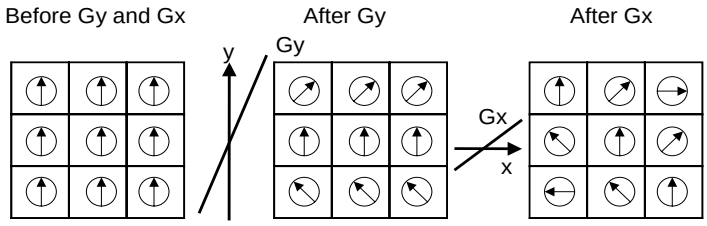

Figure 2.8: Frequency and phase encoding. Spatial information is derived from the frequency and phase of the spinning protons.

2.2.5 Image Reconstruction

Every time we do a phase encoding step we receive a signal, all of which are different because they have different phase shifts. Each one of these signals fills one line in a set of rows referred to as *data space*. In data space the coordinates are in the time domain and thus the signal that goes into each row is the *sum* of all the signals from individual voxels in the slice. *k-space* is a complex valued two-dimensional matrix derived from data space, and each line in it represents a sampled version of the received signal. k-space is in the spatial frequency domain, containing information about the frequency and origin of the signal. The x-axis of k-space (k_x) is the frequency encoding direction whereas the y-axis (k_y) is the phase encoding direction. The center line of k-space contains the phase encoding step with the weakest gradient and therefore the strongest signal. Each slice has its own k-space.

The process of converting the data held in k-space into an image is achieved by *Fast Fourier Transform (FFT)*. The Fourier transform decomposes the signals in the real and imaginary parts of k-space, producing two images: a *magnitude* image (real part) and a *phase* image (imaginary part). More formally, the Fourier transform of a spatial function $\rho(x, y)$, denoted by $\mathcal{F}\{\rho(x, y)\}$ or $S(k_x, k_y)$, is defined as :

$$\mathcal{F}\{\rho(x,y)\} = S(k_x,k_y) = \iint \rho(x,y)e^{-i2\pi(k_x x + k_y y)}dxdy$$

where k_y and k_x are given by

$$k_x = \frac{\gamma t}{2\pi} G_x, \quad k_y = \frac{\gamma t}{2\pi} G_y.$$

For our purpose $S(k_x, k_y)$ are the acquired experimental data measured in k-space while $\rho(x, y)$ is the desired image function representing for example the spin density function. Given $S(k_x, k_y)$, we can recover $\rho(x, y)$ using the inverse Fourier transform:

$$\rho(x, y) = \mathcal{F}^{-1}\{S(k_x, k_y)\} = \iint S(k_x, k_y) e^{-\imath 2\pi (k_x x + k_y y)} dk_x dk_y$$

The magnitude image is used for visual inspection while the phase image, which is more sensitive to moving spins and magnetic field inhomogeneities, is useful for cases in which the direction is important, such as when measuring flow (see Figure 2.9).

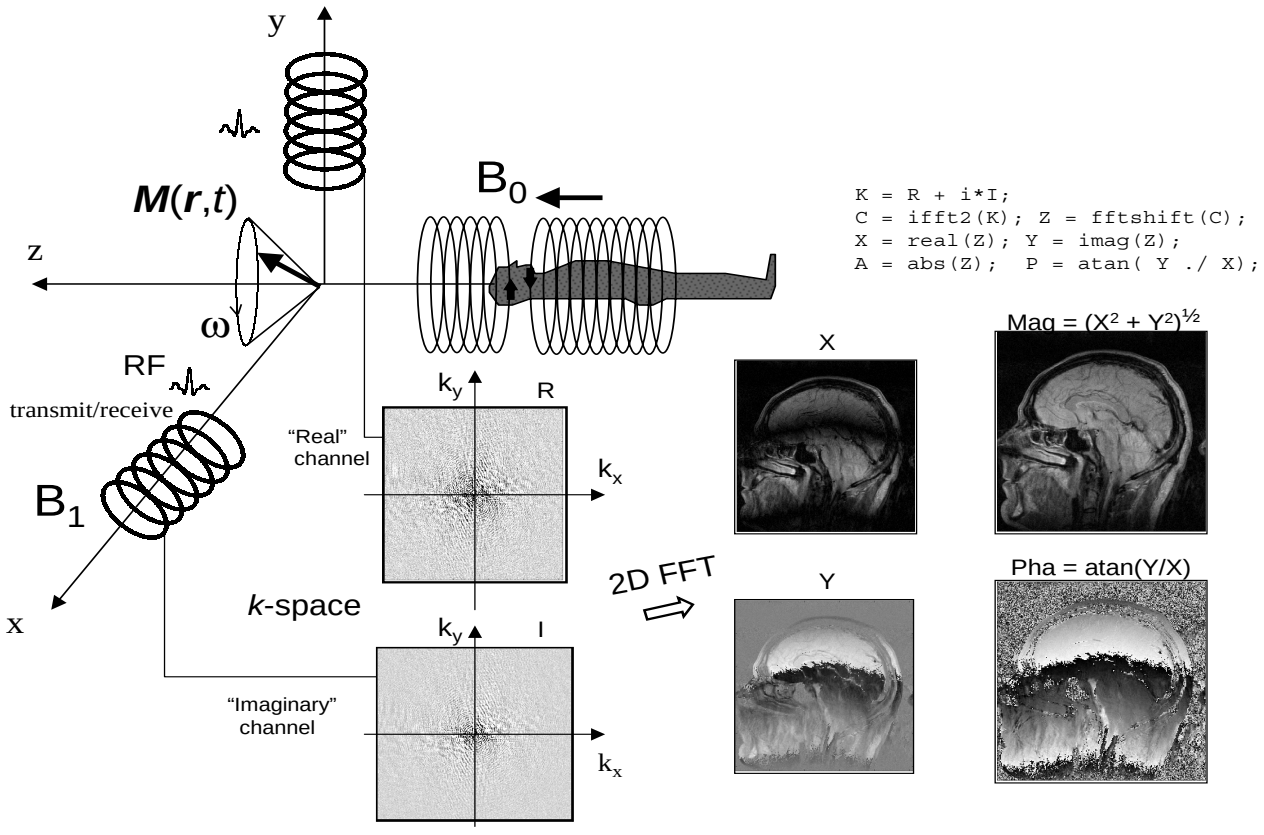

Figure 2.9: MR image formation. X is the real and Y is the imaginary part of the reconstructed image. Mag is the magnitude image whereas Pha is the phase image. In this thesis we shall use the magnitude image. x, y, z are scanner coordinates and k_x, k_y are spatial frequency coordinates. (Modified from A. Lundervold, 2000)

2.2.6 Relaxation and Tissue Contrast

Whenever the RF-pulse is cut off, B_0 will regain its dominating influence on the net magnetization. This process, in which the net magnetization looses its energy, is termed *relaxation*. Relaxation consists of two independent processes :

- **T1 recovery** is the process in which the net magnetization returns to its ground state in the direction of the main magnetic field B_0. In the process of returning to their initial energy level, the protons loose energy to the surrounding environment or lattice (spin-lattice relaxation). The rate of this recovery is an exponential process, with time constant T1.
- **T2 decay** is the loss of transverse magnetization. It occurs when the magnetic fields interact with each other (spin-spin interaction) and exchange energy, resulting in a spin de-phasing. Like in T1 recovery the rate of the T2 decay is characterized with a time constant T2.

During relaxation, signals can be detected by the receiver coil within the MR scanner. Since T1 and T2 relaxation times depend on the biological materials, tissues of different nature will emit different signals. A tissue with a high signal has a large transverse component of magnetization and is displayed as white areas in the image. In contrast, a small transverse component will result in a low signal and appear therefore as dark areas in the image. The two substances that differ the most are fat and water. The T1 recovery and T2 decay of fat is short, whereas both T1 and T2 of water are long. T1-weighted images will thus display water as dark areas and fat as white areas. In T2-weighted images, however, fat will produce a low signal resulting in dark areas whilst water with the stronger signal, will appear as white areas. A list of T1 and T2 relaxation times of brain tissues are listed in Table 2.1.

Tissue	T1 (ms)	T2 (ms)
Grey Matter	1000	106
White Matter	650	69
Fat	260	60
Cerebrospinal Fluid	4000	2300

Table 2.1: T1 and T2 relaxation times of brain tissues at 1.5 Tesla

In order to create images, we need a sequence that appropriately alternates between an RF pulse and relaxation. The time between two successive RF pulses is denoted TR, while TE is the time interval between the RF pulse and the signal measurement. Both TE and TR are conventionally measured in milliseconds. We can obtain T1 weighted or T2 weighted images by choosing appropriate settings for TR and TE. Short TE and short TR will produce a T1 weighted image, whereas long TE and long TR will produce a T2 weighted image.

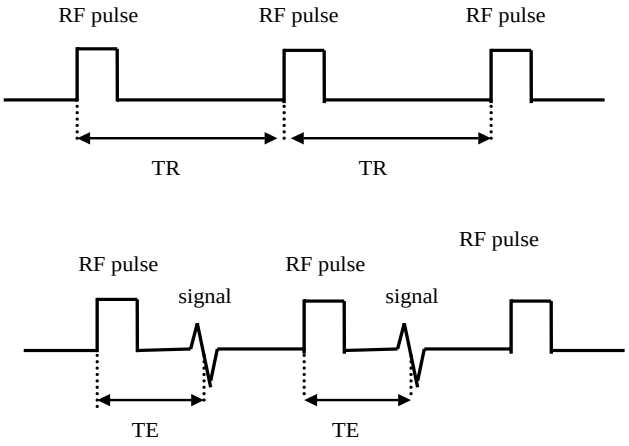

Figure 2.10: TE (echo time) and TR (repetition time). The repetition time is the time interval between each RF cycle whereas echo time is defined as the time interval between the RF pulse and the signal measurement.

T2* weighted images

T2 decay depends on the spin-spin interaction in the tissue (internal inhomogeneities). There is another phenomenon that makes spin get out of phase, namely inhomogeneity of the external magnetic field. T2* decay depends on both the external magnetic field and on the spin-spin interactions. T2* relaxation time is always shorter than T2.

2.2.7 Pulse Sequences

A pulse sequence is a sequence of RF-pulses and gradients applied repeatedly during the process of producing an MR image. The choice of the parameters TE and TR determines the weighting of the images, whereas the quality of the images depends on several factors:

- Signal to Noise Ratio (SNR)

- Contrast to Noise Ratio (CNR)
- spatial resolution
- scan time

SNR is the ratio of the amplitude of the received signal to the average amplitude of the noise. CNR is defined as the difference in the SNR between two adjacent areas. Both SNR and CNR will be discussed in Section 2.2.8. The spatial resolution is controlled by voxel size, small voxels give a good spatial resolution since small structures can be easily differentiated. The scan time is the time it takes to complete image acquisition. A long scan time increases the chance of the patient moving inside the scanner, thereby reducing image quality.

Spin Echo Sequences (SE)

As described earlier, the T2* relaxation has two components, inhomogeneities caused by the external magnetic field and inhomogeneities on the molecular level. It is this last component that is interesting from a medical view. Consequently, we seek to produce an image that reflects only the differences in T2 contrast, disregarding the external component of T2*. The external magnetic inhomogeneities are constant over time, and are therefore simple to eliminate. In the SE sequence a 90° RF pulse is followed by a 180° RF pulse. After the 90° pulse we will detect a signal which gradually decays due to the T2* relaxation effect. After the 180° pulse, however, the signal gradually returns as the protons move back in phase with each other. This signal is called an *echo* and the pulse sequence is therefore called a Spin-Echo sequence. The purpose of the SE sequence is to separate the two components of T2*. Due to the microscopic component of T2*, which varies over time, the protons does not fully return back in phase with each other after the 180° pulse. This means that the echo-signal will rely on the microscopic, tissue-dependent T2 values and not on the external magnetic field inhomogeneities. The intensity of the signal will thus be a function of the tissue's T2 values and the time between the 90° pulse and the 180° pulse.

If the TE's are close to zero, the signal will be sampled directly after the 90° pulse. At this point the T2 relaxation has no effect on the signal, and differences in signal intensity depend therefore primarily on the proton density of the tissue. A voxel with many protons will result in a stronger signal (and consequently also a stronger echo signal) than a voxel with a smaller number of protons. MR images that display differences in proton density are called proton density images.

An MR image that emphasizes the differences in the echo signal due to T1 differences of the tissue, is a T1 weighted image. To produce a T1 weighted image from the SE sequence, two criteria need to be satisfied. First, TR must be relatively short, such that there is a marked difference between available net magnetic moments for different types of tissue (this usually means a TR of 300-800 milliseconds). Secondly, TE must be short in order to avoid T2 contrast in the image.

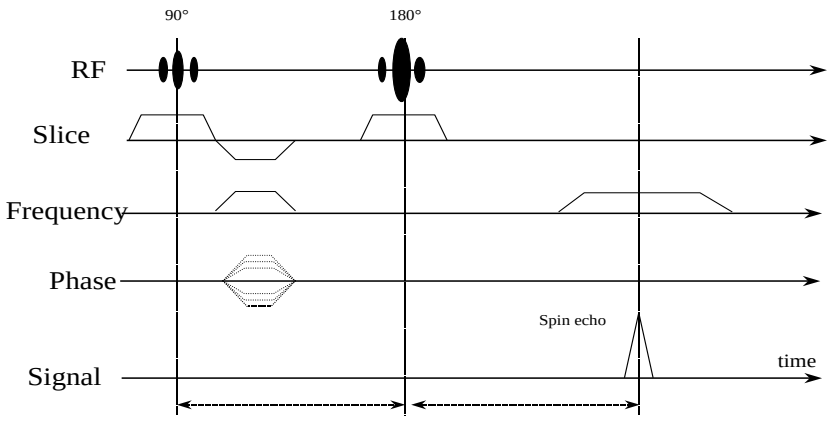

Figure 2.11: Spin Echo sequence

Gradient Echo Sequences (GRE)

A major drawback with the SE sequence is that it is time consuming. The overall acquisition time is directly proportional to the length of TR, which therefore should be reduced to a minimum. The challenge is to produce an echo without the 180° RF pulse, and as the name (Gradient Echo Sequences) implies, the gradients are also used for this purpose. Consider a gradient that is kept constant after the 90° RF pulse; the protons are de-phasing and the NMR signal decreasing. If the gradient after a time t is "reversed", the protons will move back in phase, and an echo is produced. This echo does, however, depend on both components of T2*, and as such it is not a "true" T2 contrast. The reason for not using the original signal is that the echo signal contains more information than a NMR signal, and is therefore better suited for image construction. Another characteristic of the GRE sequence is an RF pulse yielding a smaller *flip angle* than the usual 90° RF pulse. Short TR and a flip angle $< 90°$ results in a small net magnetism, and subsequently a

smaller signal than in a SE sequence. As a result, one should expect a poor Signal to Noise Ratio. This is compensated, though, by the higher temporal resolution in the GRE sequence, which makes it possible to increase the number of scans and thereby enhancing the statistical power.

Advanced Imaging Techniques

Most available imaging techniques are modifications of Spin Echo and/or Gradient Echo procedures. In some fast scanning techniques, multiple echoes with individual phase encoding within each TR are generated(examples are *Turbo* or *Fast* spin echo sequences and Echo Planar Imaging - EPI). Single-shot techniques allow for all the lines of K space to be acquired in one TR, thereby reducing scan times even further.

Within the gradient echo (GRE) sequences there is a wide range of variations compared to the spin echo (SE) sequences. Not only is the basic sequence varied by adding dephasing or rephasing gradients at the end of the sequence, but there are also the TR, TE and the flip angle to consider. For the gradient echo sequence *FLASH* (Fast low-angle Shot), a larger flip angle give more T1 weighting to the image, whereas a smaller flip angle give more T2 or actually T2* weighting to the images. The contrast between different tissues in FLASH images is such that they are well suited for anatomical inspection(see Figure 2.13).

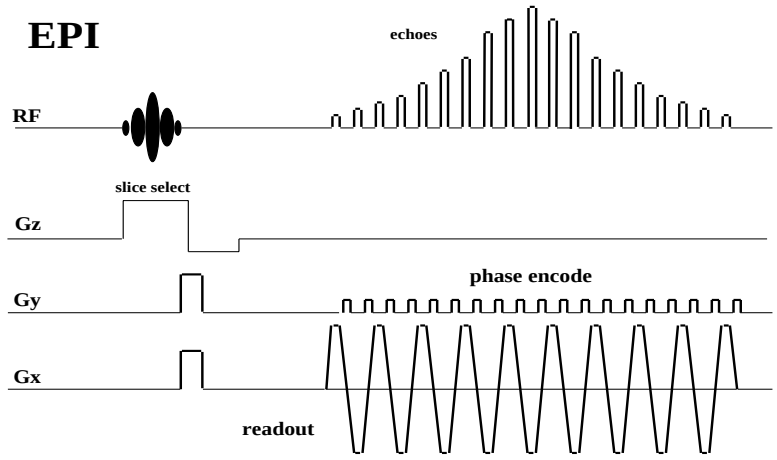

Figure 2.12: Echo Planar Imaging Sequence

Echo planar imaging (EPI)(see Figure 2.12) is another gradient echo technique related to fast gradient echo imaging. In EPI the entire set of phase steps is acquired during

one acquisition TR. To accomplished this, the frequency encoding gradient is rapidly and repeatedly reversed. EPI sequences may use only gradient echoes or combine a spin echo with the train of gradient echoes. Echo planar images can be acquired in the order of $100ms$ or less and are therefore useful for detecting rapidly changing processes like those of the brain. Whole brain volumes, consisting of multiple 2-dimensional images (slices), may thus be acquired in 1-2 seconds depending on the number of slices (see Figure 2.14). In all, most of the imaging methods used for functional MRI are based on the principles of EPI.

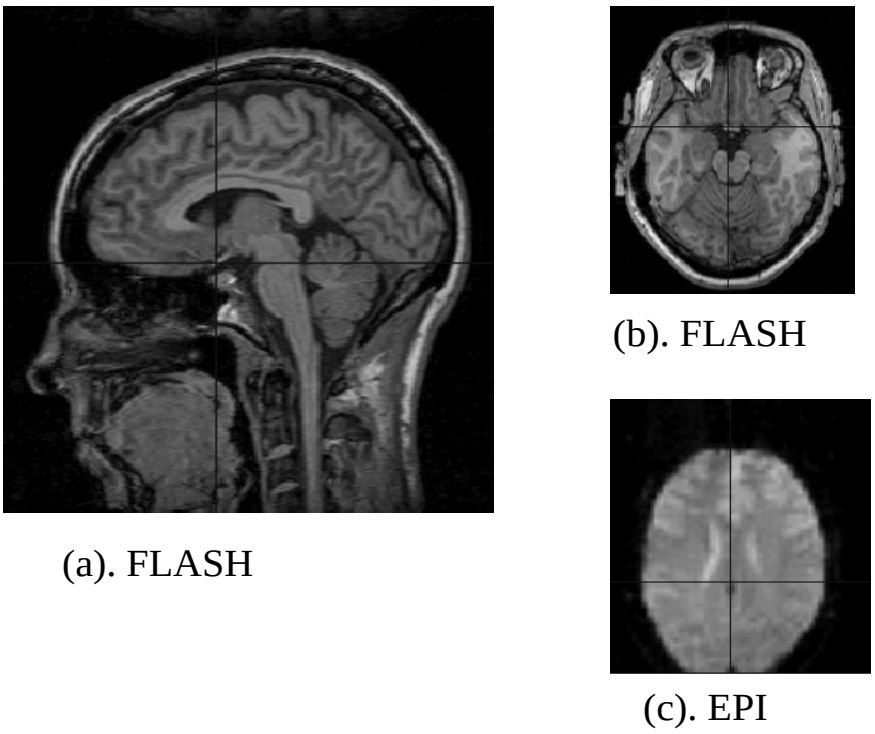

Figure 2.13: FLASH versus EPI. (a) FLASH image, sagittal slice, (b) FLASH image, axial slice, (c) EPI, axial slice

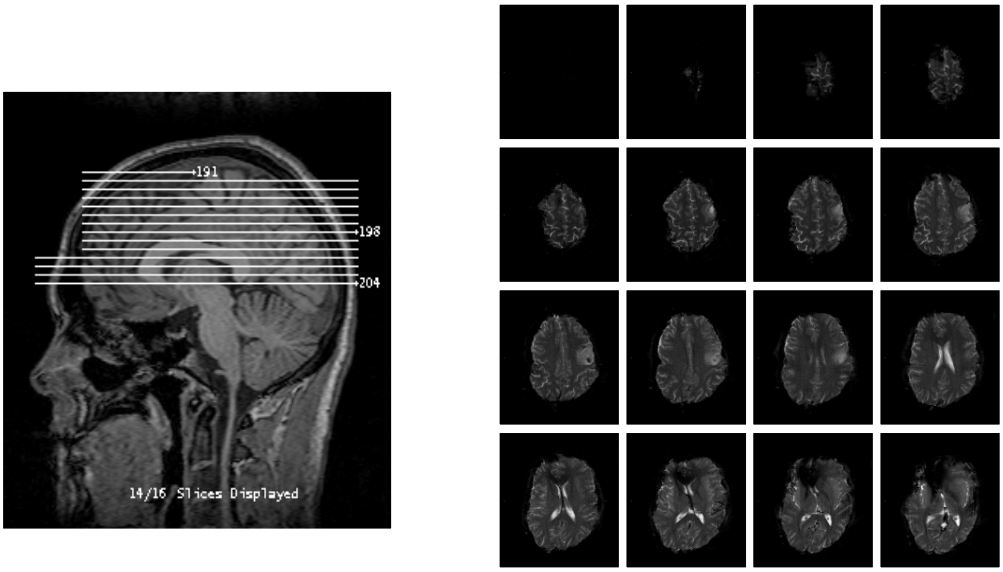

Figure 2.14: Multislice EPI

2.2.8 Image Noise and Artifacts

There are two main sources of image noise, random noise, and structured noise [23]. Random noise is time invariant and occurs at all frequencies. For k-space values (k_x, k_y) the measured signal, s_m, can be described as:

$$s_m(k_x, k_y) = s_t(k_x, k_y) + \varepsilon(k_x, k_y)$$

where s_t is the true signal. The noise term, $\varepsilon(k_x, k_y)$, derives from random fluctuations generated by the subject within the scanner as well as background noise from the equipment. The noise variance is given by :

$$\sigma^2_{therm}(k_x, k_y) = \sigma^2_{bodytissue}(k_x, k_y) + \sigma^2_{coil}(k_x, k_y) + \sigma^2_{electronics}(k_x, k_y)$$

Signal to Noise Ratio

Signal to Noise Ratio (SNR) is the ratio of the amplitude of the received signal to the amplitude of the noise. The signal, S, is dependent on the stimuli and is therefore increased

or decreased relative to the noise. Signal to Noise Ratio can be formulated as :

$$SNR \equiv \frac{S}{\sigma_0}$$

where σ_0 denotes the *noise standard deviation*. There are a number of parameters that influence the Signal to Noise Ratio, and they should be chosen so that SNR is maximized. The relationship between SNR and these parameters is given by :

$$SNR \propto (voxelvolume)\sqrt{(N_y)(NEX)/(BW)}.$$

SNR is thus increased by an increase in voxel volume, the number of acquisitions per phase encoding step (N_y) or the number of scans/excitations (NEX), or decreased bandwidth (BW).

Contrast to Noise Ratio

Contrast to Noise Ratio (CNR) depends on the same factors as SNR. The SNR is defined by the difference in SNR between two neighbouring areas. A high CNR is essential for the ability to distinguish pathology from normal tissue. A measure of σ_0 can be achieved by computing the mean of a region outside the object.
Contrast between tissue A and B and the CNR is given by the formulas :

$$C_{AB} \equiv S_A - S_B$$

and

$$CNR_{AB} \equiv \frac{C_{AB}}{\sigma_0} = \frac{S_A - S_B}{\sigma_0} = SNR_A - SNR_B$$

Image artifacts

Image artifacts, which to some degree are present in all MR images, arise from a variety of causes, including the imaging technique itself and natural processes or properties of the human body. Some artifacts may be avoided, while others can only be reduced. A brief description of the most common artifacts is given below.

- Motion

  Motion artifact is caused by the subject within the scanner. These are either voluntary (random) or involuntary (periodic). *Random motion* such as breathing, coughing, swallowing and changing position generally causes blurring in the images.

  Periodic motion, which produces an artifact known as *ghosting*, arises from periodic pulsation, for example from vessels or cerebrospinal fluid. Mechanical vibrations, receiver coil and fluctuations of the magnetic field may also produce ghosts.

- Geometrical distortions

  The various processes that distort the magnetic field strength also lead to geometrical distortions of the image. Sources of geometrical distortion include inhomogeneity in the external magnetic field, spatial variations in magnetic susceptibility and nonlinearity in the magnetic field gradients [45]. The fMRI method of choice, EPI (see Section 2.2.7), produces images that contain a significant amount of T2* decay. The technique is thus sensitive to the field inhomogeneities found in tissue, air and bone. Difference in magnetic susceptibility between air and body tissue and between different body tissues cause signal loss and distortion at the boundaries of the tissues. The EPI technique is especially subject to geometrical distortions because of the long read-out time after each RF pulse.

- Wrap around

  Anatomy outside the selected imaging area (FOV) produces signals which will be detected if the distance to the receiver coil is small. Wrap around or aliasing artifact arise when these structures are mapped inside the FOV. The part of the anatomy that lies outside the FOV is projected on to the other side of the image. Anti-aliasing methods can be applied to compensate for this wrapping effect.

This concludes the MR physics section. Further reading on the subject can be found in [21] and [43].

2.3 Preprocessing of fMRI data

Before the sampled image time series can be subject to statistical analysis, a few preprocessing steps are required.

- *Image registration* is the process of geometrical transformations applied to an image when aligning it spatially to another image. This procedure is necessary to minimize the effects of motion in series of images, as in fMRI where a single session may consist of several hundred EPI images. Aligning images acquired of a subject in *different* MR sessions is another important area of application.

- *Normalization* maps a brain image into a standardized reference space. The most commonly used coordinate system within brain imaging is that described by the atlas of Talairach and Tournoux [42]. Normalization is useful for the comparison of different subjects and databases. Activations can be reported according to their

coordinates within the standard space. Due to the fact that there is no one-to-one mapping of cortical structures between subjects, matching is only possible on a coarse scale [1].

- *Smoothing* is a low pass filtering (e.g. Gaussian) which convolves the voxels in the EPI images with a kernel shaped according to the applied filter. Smoothing improves the image quality by increasing the Signal to Noise Ratio [46].

- *Slice-timing* is a procedure for correcting er-fMRI time series data for the differences in image acquisition time between slices.

Upon completing the preprocessing procedure the functional data-set can be submitted to statistical analysis and the results superimposed on a structural high resolution image. The datasets used in this thesis has been preprocessed with The Statistical Parametric Mapping (SPM99) software toolbox (see Appendix A.3).

2.4 Functional Magnetic Resonance Imaging (fMRI)

We are what we think.
All that we are arises with our thoughts.
With our thoughts, we make the world.
Buddha

Functional Magnetic Resonance Imaging (fMRI) produces brain images that reflect neuronal activity due to sensory, cognitive or motor tasks [16]. The fMRI technique, which is about to enter its second decade as a scientific discipline, has dramatically expanded the possibilities for the study of human brain function and pathology. Since it is non-invasive and has no significant risks, it is widely applicable and a considerable number of studies have been conducted in numerous MR laboratories. The first fMRI experiments used an exogenous contrast agent, but this was soon replaced by the so-called blood oxygenation level dependent (BOLD) contrast. A typical fMRI experiment measures the correlation between the BOLD response and a stimulus regime.

2.4.1 Blood Oxygenation Level Dependent (BOLD) Contrast

The BOLD-contrast arises form the magnetic properties of blood, first described by Pauling and Coryell in 1936 [37], and is the most widely used fMRI-method for detection of brain activation. Haemoglobin, the major component of the red blood cells, is an organic molecule that transports oxygen in the vascular system of the body. As blood perfuses from the arterial side of the capillary bed to the venous side, oxygen dissociates from the haemoglobin supplying the tissue with oxygen. Deoxyhaemoglobin (haemoglobin without oxygen) has, due to unpaired electrons, a relatively large magnetic moment. When oxygen binds to haemoglobin (oxyhaemoglobin), the unpaired electrons are transferred to the oxygen molecules, eliminating the magnetic moment. Oxyhaemoglobin is therefore diamagnetic, whereas deoxyhaemoglobin is paramagnetic, thus creating microscopic magnetic field gradients in its vicinity yielding different signal intensities (see Figure 2.15). This mechanism give rise to BOLD-contrast on T2* weighted images (see Section 2.2.6). At rest (periods of no stimuli) the amount of deoxyhaemoglobin and oxyhaemoglobin are similar, but during brain activity, both blood flow and metabolism are increased and more oxygen is extracted from the capillaries. The increase in delivered oxygen, however, exceeds the metabolic need, leading to an increase in the oxyhaemoglobin content and a relative

decrease in the fraction of deoxyhaemoglobin in the venous part of the micro-circulation of the capillary bed [34].

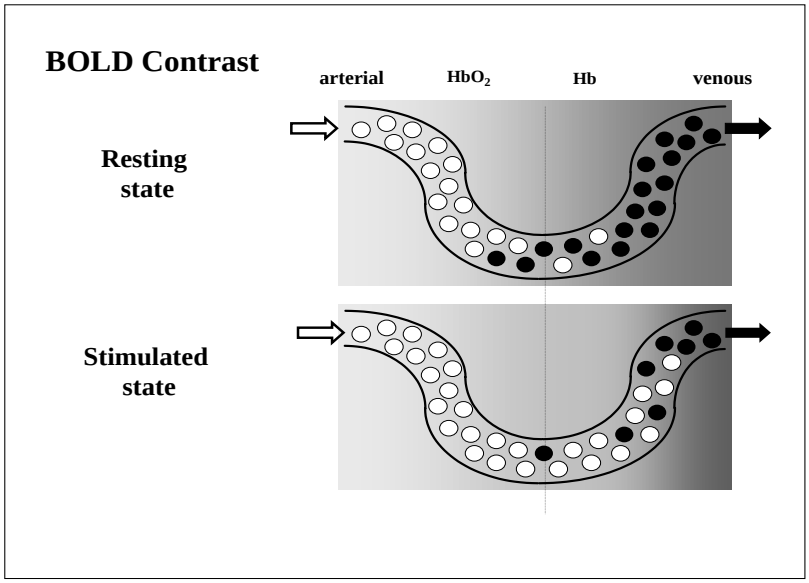

Figure 2.15: Haemoglobin concentration in blood during rest and activation. During stimulus induced activation there will be a higher proportion of oxyhaemoglobin (white) on the venous side of the capillary bed, thereby increasing the MR signal intensity from this region.

The amount of deoxyhaemoglobin thus depends on physiological factors such as the change in Cerebral Blood Flow (CBF), the rate at which oxygen is metabolized ($CMRO_2$) and the change in Cerebral Blood Volume (CBV). The ratio of deoxyhaemoglobin to oxyhaemoglobin is the basis for the BOLD contrast. Vessels that contain a significant amount of deoxyhaemoglobin creates, due to its paramagnetic nature, local field inhomogeneities causing increased spin-spin dephasing. During activity the relative amount of deoxyhaemoglobin decreases leading to a decrease in dephasing and hence an increase in signal intensity (see Figure 2.16). The mechanism behind the BOLD response are very complex and are subject to both underlying physiological processes and imaging physics events [24]. A voxel in an fMRI experiment usually has a size in the order of $3mm \times 3mm \times 3mm$, it is thus a problem that a large number of voxels contain vessels of varying sizes, ranging from small capillaries to larger draining veins. The exact relationship between this underlying vascular geometry, distribution of deoxyhaemoglobin and signal change has yet to be established.

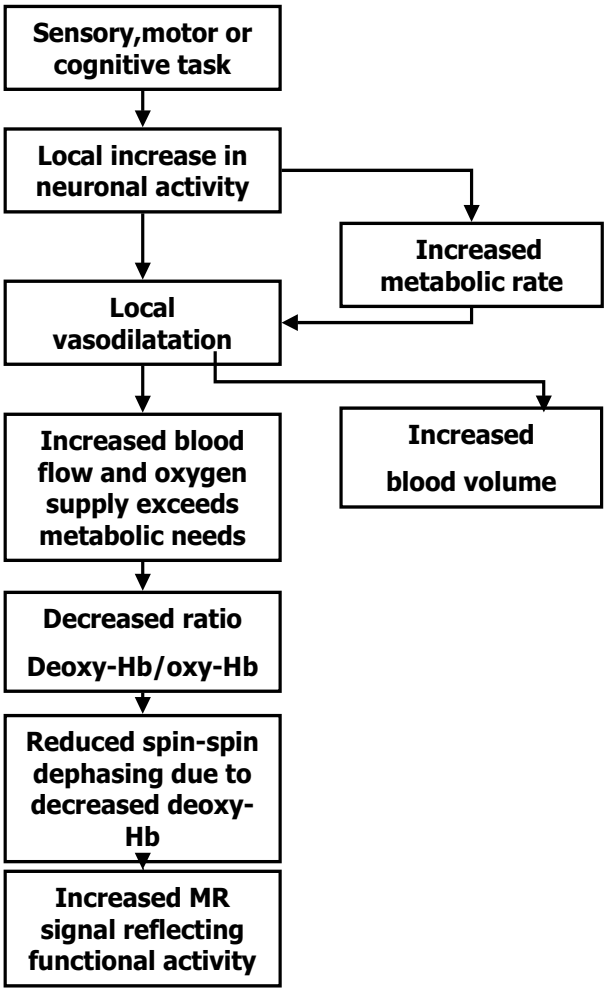

Figure 2.16: Hypothesized mechanism of BOLD contrast in fMRI, modified from DeYoe et al. [16]

2.4.2 Experimental design and image acquisition in fMRI

In human brain studies it is of vital importance that the image data are sampled rapidly. The aim is that activation states for the whole brain should be obtained as synchronously as possible. Most of the high speed imaging techniques used in fMRI, are based on the principles of Echo Planar Imaging (EPI see Section 2.2.7). The EPI technique has the necessary speed, a reasonable spatial solution and a good Signal to Noise Ratio (SNR). If the MR signal is made sensitive to differences in the rate of *proton spin* dephasing (T2* weighting), the images will reflect changes in the level of blood oxygenation. The collected fMRI data are processed to locate areas of the brain where signal intensity changes are consistent in time with the applied stimuli. Each voxel of the image thus has a one-

dimensional time series, with length equal to number of scans, associated with it. To detect stimulus related activity, each voxel time series can be compared with a predicted/expected response function.

During an experiment the subject lies within the scanner viewing a screen illuminated by an LCD video projector, listens to auditory input via headphones, or performs some other form of task, while a sequence of images are sampled. The presentation of stimuli and the scan sequence are synchronized, either manually or by a computer. Brain activation paradigms must be designed so that they reliably detect and isolate the neural changes associated with cognitive, sensory, or motor events. A typical fMRI experiment applies a specific set of assumptions to localize relative differences in brain activity between active and baseline tasks. fMRI designs are either *blocked*, with relatively long periods of stimuli followed by intervals of rest, or *event-related*, in which the individual trials are isolated.

2.4.3 Blocked vs. Event-Related design

The block design is traditionally the most common design in fMRI experiments. In blocked task paradigms the MR images are acquired continuously while subjects are presented with blocks of stimulation (duration of approximately 30 seconds each), intermixed with rest intervals. Blocks of trials, condition versus rest or condition 1 versus condition 2, are then compared using statistical tests.

More formally, in a blocked trial design, each voxel in the image is a function, $f(x, y, z, t) \in \mathbf{R}$, of location and time, where x denotes the column, y the row and z the slice in the volume sampled at time t. There are n blocks with k trials in each block where block i represents the condition $c_i \in \{1..m\}$, and $t \in \{t_{11}, ..., t_{1k}, ..., t_{n1}, ..., t_{nk}\}$ (see Figure 2.17).

Since fMRI noise is assumed to be normally distributed and stationary in time [27], averaging across trials in the blocked trial design increases the Signal to Noise Ratio (SNR, see Section 2.2.8). Time dependent behavior and brain function, such as learning, alterations in strategy and errors, or habituation (all which are common in cognition) may, however, change during a block of repeated trials. In such cases the averaging approach looses unique information due to the effects of learning and strategy [32].

Event-related (or single trial) functional Magnetic Resonance Imaging (er-fMRI) is a relatively new experimental design that allows different trials to be presented in arbitrary sequences, thereby eliminating the potential problems as mentioned above. Several studies, e.g. [5, 14, 29, 27, 11, 8, 38] has demonstrated that er-fMRI has the ability to detect activation from very brief periods of stimulation, in the order of ms. These procedures also

show that the BOLD response is delayed in relation to the neuronal activity, extending over several seconds. These findings represents a challenge to er-fMRI since BOLD responses to adjacent trials may overlap. A solution is to space the trials so far apart that the BOLD response has returned to baseline after each trial. This does, however, severely limit the total number of trials and hence the number of trials upon which to average, decreasing the Signal to Noise Ratio. It has been suggested that trials be spaced close together, only a few seconds apart, subsequently applying methods for removal of overlap between the BOLD responses[14].

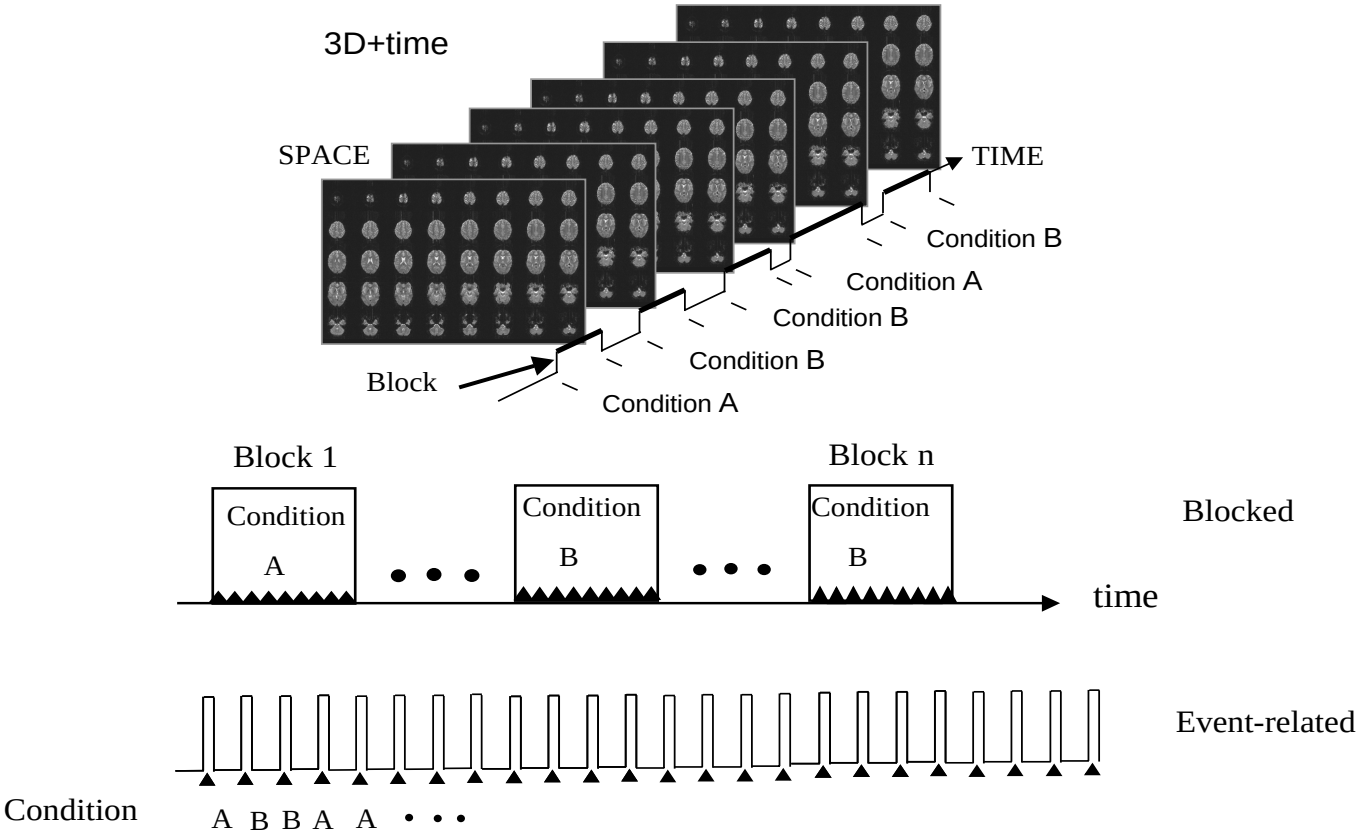

Figure 2.17: Blocked vs. Event-Related design. In fMRI experiments with a *block* design subjects are presented with blocks of stimulation intermixed with resting intervals whereas in *event-related* fMRI single trials are presented in arbitrary sequences.

Part II

Theory

Chapter 3

Physiological models of the BOLD response

Buckner et al. [7] gives two key characteristics of the BOLD response:

- it can be elicited following brief periods of neuronal activity, and
- it can be characterized by a well-behaved and reliable impulse function.

Knowledge about the properties of the BOLD response is essential to both experimental design and analysis of er-fMRI data.

3.1 Characteristics of the BOLD response

At the onset of neuronal activity the oxidative metabolism is immediately upregulated, the increase in cerebral blood flow, however, takes somewhat longer. This leads to an initial increase in the relative amount of venous deoxyhaemoglobin and thus increased spin-spin dephasing resulting in a decreasing MR signal [22, 27]. As the regional cerebral blood flow and subsequently the amount of oxyhaemoglobin increases, the ratio of deoxyhaemoglobin to oxyhaemoglobin decreases leading to reduced spin-spin dephasing and consequently an increasing MR signal (see Section 2.4.1). This is consistent with the observed BOLD response, which in the context of a brief fixed interval of stimulation has a small signal decrease of about 1 sec duration, after which it increases and reaches a peak after 4-8 seconds. Although complete return to baseline may take as long as 30 seconds, the robust response generally evolves over the first 10-12 seconds [7, 2, 16, 24, 9]. At the end of the response the signal has been observed to dip below baseline and remain depressed for several seconds [27, 9]. Buxton et al. [10] suggests that changes in the blood volume passively follows the blood flow changes and that the post-stimulus undershoot simply may

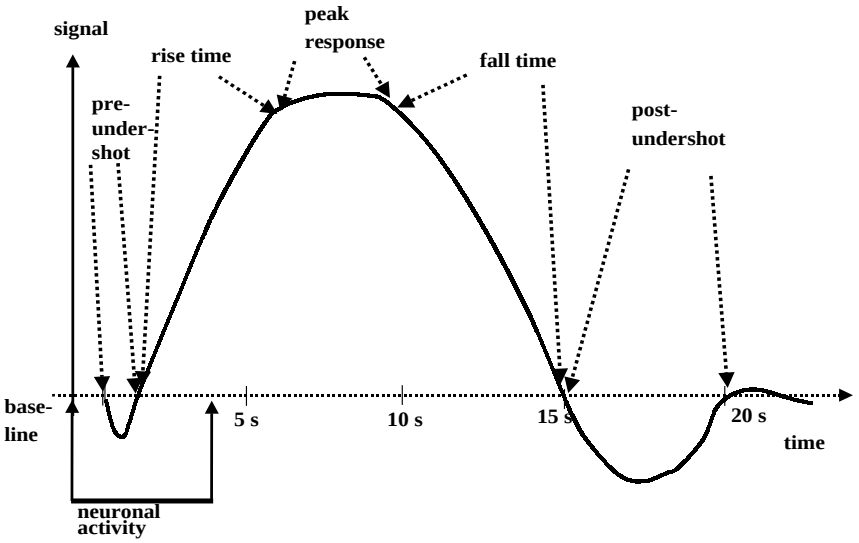

Figure 3.1: Signal time course of the BOLD response. The pre-undershoot is interpreted to arise from an initial increase in the relative amount of deoxyhaemoglobin due to a delayed increase in blood flow. Rise and fall times are the times it takes for a signal to reach its maximum intensity, or in the latter case, return to baseline. Peak response is the time period of maximum signal intensity. Post-undershoot has been interpreted as secondary effects that does not reflect the more basic physiological changes in flow and oxygen metabolism.

be a secondary effect which therefore does not reflect the more basic physiological changes in flow and oxygen metabolism.

The basic shape and timing of the haemodynamic response for similar regions of the cortex is reported to be broadly similar across subjects (see Figure 3.1). The temporal properties of the BOLD response can, however, vary in timing from brain region to brain region, also within the same subject [7].

BOLD responses which arise early following a brief stimuli are most often asymmetric, with a shorter rising than falling edge, while late and wide BOLD responses tend to be more symmetric [28]. The sources of these differences in the haemodynamic response still remain unclear, but may originate from differential sampling of vessels across regions or from delays in the underlying neuronal activity [6]. Physiological factors such as heart rate, blood pressure and perfusion may also influence the shape of the BOLD-response. Respiration and the cardiac cycle causes periodic changes in blood volume. Furthermore, the vasculature differs from voxel to voxel, resulting in different BOLD-responses even if

neuronal activity is the same. These issues must be considered before comparing response magnitude and timing between locations and subjects.

The rate at which the EPI series are sampled is of the order of 100 ms per slice or less whereas the response to a single trial/event evolves over several sampling intervals. Compared to the evoked neuronal activation, the measured BOLD response is thus dispersed and displaced in time. A *haemodynamic response function* (HRF) is a model function that attempts to describe the physiological response to sensory, motor or cognitive stimuli. To measure the correlation between the stimuli and the BOLD response, the stimuli parameter should be subject to the same delay and *dispersion* as that intervening between neuronal activity and the BOLD response. The correlation of interest then, is between the sampled fMRI signal intensity time-series and the input stimulus function convolved with the HRF. Since the mechanism of coupling between neuronal responses and haemodynamics are not well understood, there is currently no exact model of the BOLD response. Several descriptive and/or physiological approaches have nevertheless been proposed for the modeling of the BOLD response. An advantage of using model functions is the possibility to derive physiologically meaningful parameters.

One simple parametric modeling approach is to characterize the HRF by two parameters:

- *lag* - which represents the time delay between neural activations and the maximum haemodynamic response, and
- *dispersion* - which is proportional to the duration of the haemodynamic response.

The HRF can then be approximated by appropriately setting the parameters in the chosen parametric function. The values of the parameters are determined either by

- *simple specification*, i.e to find a distribution that "looks like" the observed BOLD response, or by
- *estimation* from the data

A key question is to what extent the underlying neuronal activation can be inferred from the shape of the BOLD response, e.g. how does a stronger and/or prolonged neuronal activation affect the BOLD response? The experimental conditions clearly influence both onset and duration of the response, and must therefore be considered in the modulation of the response function. Overlapping responses may severely distort the individual responses to temporal adjacent trials, and is therefore a potential challenge in er-fMRI. The obvious solution would be to place trials sufficiently far apart, thereby avoiding the problem but

also decreasing the number of trials per time unit in the particular scanning session. An alternative approach involves methods for resolving overlap between closely spaced trials [7, 14]. In these event-related fMRI experiments trials are presented as close as 2 sec or less apart, and consequently there is no time for baseline return between successive trials. The resulting summation of the haemodynamic responses have been found to be approximately linear [5, 14]. There seems, however, to be a critical stimulation frequency where the measured signal saturate. Whether these nonlinear effects occur on a neuronal level and/or a haemodynamic level is still unclear. Thus, it is not known whether the underlying neuronal activity is itself linearly additive across time and trials. In order to estimate and remove overlap in the BOLD response, a model for how the measured response relates to the response of each individual event is required. Such a model is presented in Section 4.2.

3.2 Simple parameterizations of the BOLD-time course

The measured fMRI signal, y, depends on the type of stimulus, brain site, time in stimulus history (e.g. neural adaptation), individual processing abilities as well as undesirable effects such as body motion, scanner instabilities, physiological and electronic noise, etc. The undesirable effects, which to some extent is reduced during preprocessing of the acquired data, can collectively be modeled as a stochastic part, ϵ. The HRF is a deterministic function, $g(t, \boldsymbol{\theta})$ in which $\boldsymbol{\theta} = (\theta_1, \ldots, \theta_p)$ is a parameters vector of length p. We introduce a matrix $\mathbf{y}$ for a single experimental run consisting of l discrete time samples in a brain region consisting of k voxels:

$$\mathbf{y} = \begin{bmatrix} y_{11} & y_{12} & \cdots & \cdots & y_{1l} \\ y_{21} & y_{22} & \cdots & \cdots & y_{2l} \\ \cdots & \cdots & \cdots & \cdots & \cdots \\ \cdots & \cdots & \cdots & \cdots & \cdots \\ y_{k1} & y_{k2} & \cdots & \cdots & y_{kl} \end{bmatrix}$$

where the columns represent different time samples, and the rows represents the k different voxels sites.
The elements $y_{st} = y(s,t)$ of $\mathbf{y}$ are given by

$$y(s,t) = x(s,t) + \epsilon(s,t) \qquad s = 1, \ldots, k \quad \text{and} \quad t = 1, \ldots, l \tag{3.1}$$

where $x(s,t)$ is the fMRI signal (at site s and time t) in response to the stimulus regime, and $\epsilon(s,t)$ is the part of the observed fMRI response that is attributable to stochastic noise. This noise term is assumed to be independent of the signal, and stationary with respect to time and space. The elements $\epsilon(s,t)$ are assumed to be Gaussian distributed with zero

mean and covariance matrix $\mathbf{V}$. If we consider the observed signal intensities y_{st} as a long vector of length $n = k \cdot l$, then we can write

$$\epsilon \sim N_n(\mathbf{0}, \mathbf{V})$$

If we now consider the fMRI signal $x(s,t)$ to be a convolution between the haemodynamic response function $g(t, \boldsymbol{\theta})$ and the time course of the stimulus $r(t)$, i.e. the stimulus reference vector, we obtain the following relationship (see Figure 3.2)

$$y(s,t) = g(t, \boldsymbol{\theta}) \star r(t) + \epsilon(s,t) \tag{3.2}$$

where (cfr. Appendix A.1)

$$g(t, \boldsymbol{\theta}) \star r(t) = \sum_{k=-\infty}^{\infty} r(t-k) g(t, \boldsymbol{\theta}) \qquad t \in \mathbf{R}$$

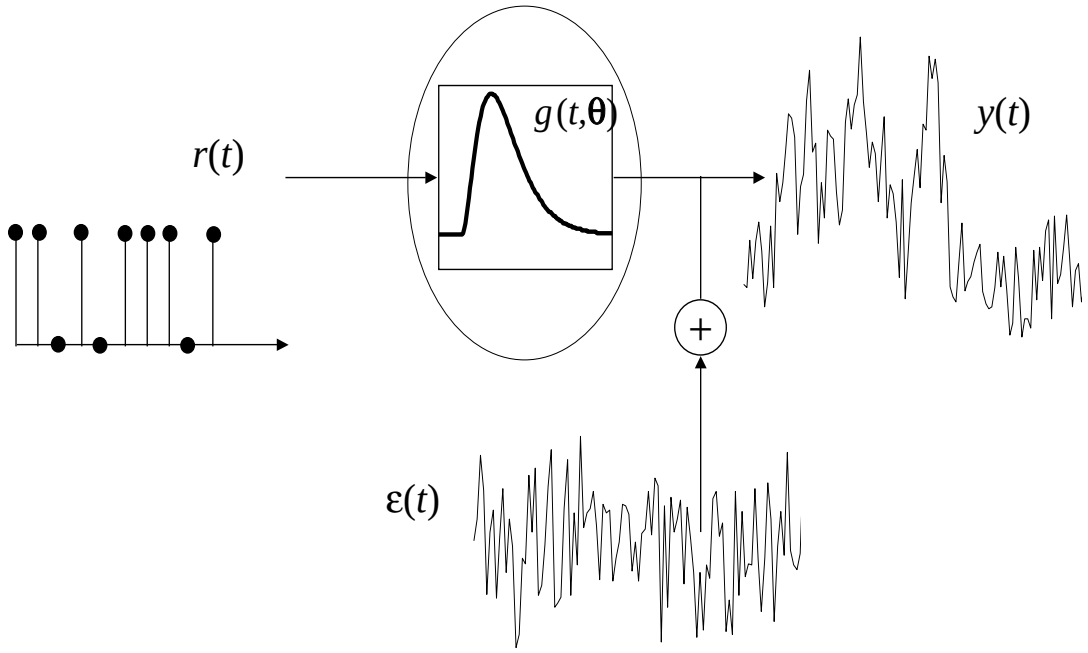

Figure 3.2: The fMRI response $y(t)$ regarded as the convolution between the stimulus regime $r(t)$ and the haemodynamic response function $g(t, \boldsymbol{\theta})$ with additive Gaussian noise, $\epsilon(t)$. The stimulus related response, $x(t) = (g \star r)(t)$ is a sum of shifted and scaled copies of the stimulus reference vector, $r(t)$ shifted to each discrete time step $t - k$ ($k = -\infty, \ldots, -1, 0, 1, \ldots, \infty$) and scaled by the the haemodynamic response function $g(t, \boldsymbol{\theta})$ at that time. (Modified from A. Dale, HBM 2000)

Equation (3.2) is primarily aimed at detecting neuronal activation in response to multiple trials. When describing the characteristics of a single BOLD-response, however, the focus is on separate trials. In such cases the stimulus reference vector consists of only one stimulus and can therefore be omitted. Thus, for the signal *description* problem, Equation (3.2) reduces to

$$y(s,t) = g(t,\boldsymbol{\theta}) + \epsilon(s,t) \tag{3.3}$$

The modeling function, $g(t,\boldsymbol{\theta})$, should be chosen such as to minimize the difference between the observed and the modeled signal. Important aspects to consider regarding the choice of modeling function is not only its ability to fit the actual BOLD-response but the parameters should also highlight important physiological characteristics such as *lag* and *dispersion*.

A number of heuristic functions have been proposed for the HRF, $g(t,\boldsymbol{\theta})$. The aim has primarily been to *detect* functional activation in the presence of high noise levels. Model parameters such as *lag* and *dispersion* may be set as global constants, but recent models have more often determined these parameters separately for each voxel or group of voxels.

One of the first functions to be suggested for the modulation function was the *Poisson* function [18]. The mean and variance of the Poisson function are equal and defined by one parameter, θ. The Poisson function is a discrete distribution which takes on real positive integers and is given by

$$g(t,\theta) = \begin{cases} \frac{\theta^t}{e^\theta\, t!} & t = 0,1,2,3...;\ \theta > 0 \\ 0, & \text{otherwise} \end{cases} \tag{3.4}$$

where t denotes time. Thus, in the modeling of the HRF, θ defines both delay and dispersal, assuming a relationship between these two components. An early block design fMRI experiment (on visual stimulation) estimated θ to a value of 7.69 seconds [18].

Gamma functions have been employed in several studies, e.g. [5, 17, 11, 39], and can in the continuous case be formulated as

$$g(t,\boldsymbol{\theta}) = \frac{\theta_2^{\theta_1}}{\Gamma(\theta_1)}\, t^{\theta_1 - 1}\, e^{-\theta_2 t} \tag{3.5}$$

in which

$$\Gamma(\theta_1) = \int_0^{+\infty} e^{-t} t^{\theta_1 - 1} dt.$$

Lag and *dispersion* for the Gamma function are defined by θ_1/θ_2 and θ_1/θ_2^2 [39], respectively, and consequently, they are not independent. In block design fMRI experiments, the Poisson and Gamma function have been reported to yield similar results [18, 39].

With the Poisson and the Gamma functions it may be hard to model interesting shape characteristics like delay, rise and fall times. These features are easier to model with the Gaussian function which therefore has been favored in a number of studies, e.g. [39, 27, 14]. The Gaussian distribution function can be formulated as

$$g(t, \boldsymbol{\theta}) = \frac{\theta_0}{\theta_1} \exp\left(-\frac{(t-\theta_2)^2}{2\theta_1^2}\right) + \theta_3, \quad where \quad t \in [1, T]. \tag{3.6}$$

The components of $\boldsymbol{\theta}$ can be interpreted as θ_0: the *height* of the BOLD response, θ_1: *dispersion* (proportional to the duration of the BOLD response), θ_2: *lag* and θ_3: *baseline* (see Figure 3.3). An advantage with the Gaussian model is that it accounts separately for the *lag* and *dispersion* of the BOLD response. The Gaussian function are potentially capable of modeling BOLD-responses with shorter rise than fall times. A convolved asymmetric model, involving two Gaussian functions with different rise and fall times, has been suggested for this purpose [28].
A number of other modeling approaches have been considered in various studies (e.g. Fourier series consisting of several temporal basis function [26] and Volterra series [25]).

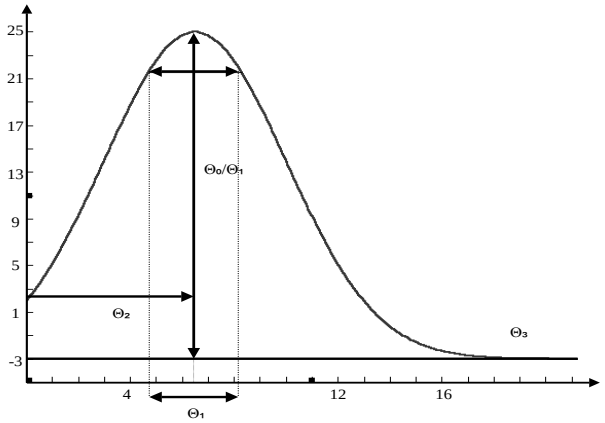

Figure 3.3: Gaussian function with explanatory parameters. The parameters can be interpreted as θ_0: the *height* of the BOLD response, θ_1: *dispersion* (proportional to the duration of the BOLD response), θ_2: *lag* (time to maximum intensity) and θ_3: *baseline*.

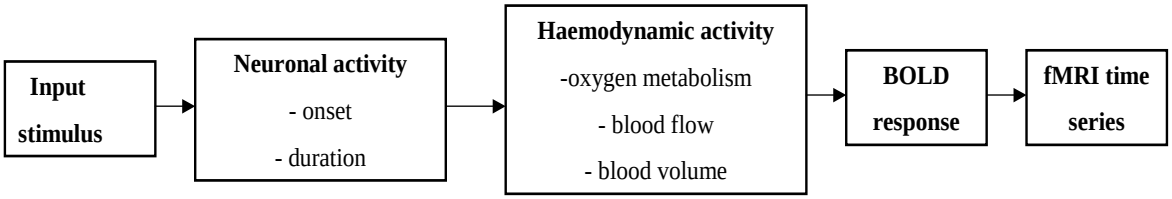

Figure 3.4: Physiological modeling of the BOLD-response in fMRI time series. The emphasis of physiological oriented models lie in the physiological mechanisms which leads to the BOLD-response. The onset and duration of neuronal activity as well as oxygen metabolism, blood flow and blood volume are features that a physiological model must consider.

3.3 Physiological models

When using heuristic modeling functions such as the Gaussian function, we seek to associate the parameters with physiological characteristics (such as *lag* and *dispersion*) related to the BOLD-response. None of these function are, however, based on a comprehensive physiological model. The sequence of events from the onset of neuronal activation to the BOLD-response is complicated and only partly understood. Neuronal activity leads to increased blood flow, which subsequently leads to changes in the magnetic properties of blood. The signal is thus doubly indirect from the physiological factors of interest (i.e. the synaptic activity of neurons). Furthermore, compared to the neuronal activity, the signal is delayed and dispersed in time. Physiologically oriented models emphasizes aspects such as neuronal onset and duration times as well as oxygen delivery, blood volume and dilatation/contraction of blood vessels etc. (see Figure 3.4).

It has been proposed that BOLD-responses are proportional to local average neuronal activity over a short period of time. This should indicate that the relationship between neuronal activity and the BOLD-response is completely characterized by a brief pulse of neuronal activity. If this hypothesis was proven correct it would simplify the analysis and interpretation of fMRI-data. However, experimental approaches testing this presumed linearity of the BOLD-response have found that while it is approximately linear, there are measurable nonlinear effects [14]. Despite this fact, this so called Linear Transform Model is considered a reasonable approximation and several studies rely explicitly on the model for their data analysis [18].

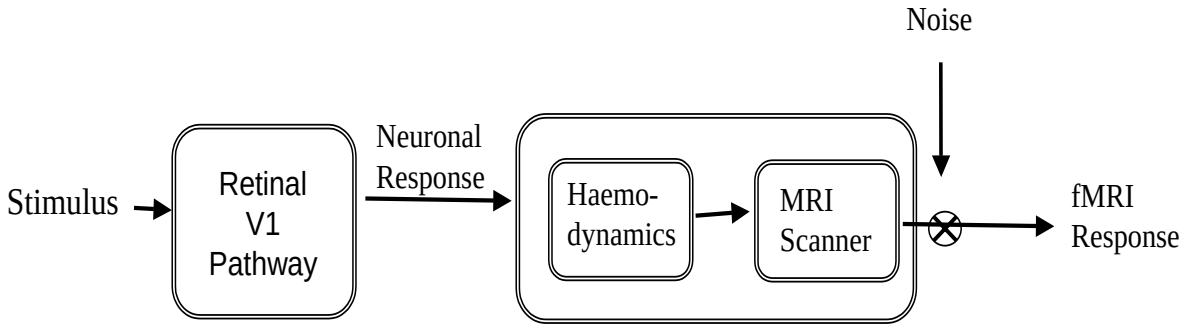

Figure 3.5: fMRI Linear Transform Model (Modified from Boynton et al., 1996). The output of the retinal visual V1 pathway (i.e. neural response) varies non-linearly with visual stimulus contrast. On the other hand, the fMRI signal mediated by the haemodynamics, is regarded to be a linear transformation of neuronal activity such that the fMRI signal is proportional to the neural activity averaged over a small spatial region and over a short period of time. The individual noise processes affecting the fMRI response can be modeled as a single additive noise source.

Within cognitive research it is desirable to separate neuronal and haemodynamic factors, because this could lead to a better understanding of the neuronal mechanisms involved in a cognitive task. The neuronal parameters should modulate characteristics such as neuronal onset and duration, as well as amount of the neuronal activation. A number of approaches can be taken in the modeling of the vascular parameters. However, in constructing a physiological model, the number of parameters must be carefully considered. Since usually just a limited number of time steps are recorded per trial, there is an upper bound for the number of parameters.

The Convolved Compartment Model is based upon flow changes in body subspaces (compartments). The aim is to separate parameters describing the vascular component from parameters describing the neuronal activation. To achieve this distinction the HRF is viewed as a convolution between a neuronal activity function, $n(\cdot)$, and a physiologically based haemodynamic function, $f(\cdot)$. The details of this model will be explored in Section 5.3.

We will now give a brief description of the Balloon Model [9], in which a biomechanical approach is considered. This model especially attempts to model the conflicting effects of the dynamic changes in blood oxygenation and (the relatively larger) blood volume.

At the onset of neuronal activity, both cerebral blood flow and the cerebral metabolic rate

of oxygen ($CMRO_2$) increases. There is, however, a large gap between the cerebral blood flow increase of $30 - 50\%$ and the $CMRO_2$ increase of approximately 5%. The Balloon model is based on the premise that there is a *strong* coupling between blood flow and oxygen metabolism, and that a small increase in $CMRO_2$ must be supported by a large increase in flow due to the biophysics of oxygen extraction. The model assumes that the capillary volume remains fixed, but allows for an expansion in the venous part of the vascular bed, hence the name Balloon model.

There is a close connection between the Balloon model and the *Oxygen Limitation Model*, which assumes that increase in blood flow in the venous compartment is a result of increased flow *velocity* on the capillary side.

An increase in the capillary transit time gives less time for diffusion and therefore a decrease in the amount of oxygen extracted from a particular blood volume. Increased blood flow and thereby also increased blood volume leads, however, to a larger proportion of oxyhaemoglobin on the venous part of the vascular bed and subsequently a stronger signal (see Section 2.4.1). When neuronal activity decreases, the blood flow slows down thereby reducing both venous blood volume and the relative amount of oxygen. This results in a decreasing BOLD-response.

More specifically, for a vascular bed within a small volume of tissue of an expandable compartment, $F_{in}(t)$ denotes the volume flow into the compartment, and $F_{out}(t)$ the volume flow out of the compartment. An increase in $F_{in}(t)$ causes the compartment to expand due to intrinsic pressure in the compartment until a new steady state, where F_{in} equals F_{out} is reached (see Figure 3.6). In reality F_{out} depends on factors such as pressure within the compartment and resistance in the vessels following the compartment. For simplicity, however, the Balloon model assumes that F_{out} merely is a function of the volume in the compartment, $F_{out}(V)$.

The BOLD-response is calculated as a function of the venous blood volume and deoxyhaemoglobin content. A detailed description of the Balloon Model is found in [9, 33].

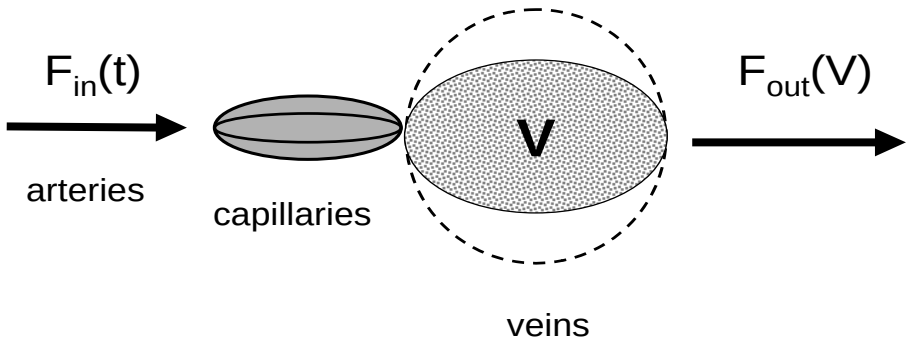

Figure 3.6: Balloon Model. At the onset of neuronal activity, both cerebral blood flow and the cerebral metabolic rate of oxygen ($CMRO_2$) increases. The Balloon model hypotheses that a small increase in $CMRO_2$ must be supported by a large increase in flow and that the capillary volume remains fixed, but allows for an expansion in the venous part of the vascular bed. $F_{in}(t)$ denotes the flow into the compartment, and $F_{out}(t)$ the flow out of the compartment. An increase in $F_{in}(t)$ causes the compartment to expand due to intrinsic pressure in the compartment until a new steady state, where F_{in} equals F_{out} is reached. F_{out} is assumed to be a function of the volume in the compartment, $F_{out}(V)$. Modified from Buxton et. al

Chapter 4

Detection of the BOLD response in fMRI

Measure what is measurable, and make measurable what is not so.

Galileo Galilei, quoted in I Gordon and S Sorkin, The Armchair Science Reader (New York 1959).

Most brain activation images relies on the concept that distinct regions "light up" during particular tasks. These images illustrate the localization and degree of activation. To produce such images, methods for detecting brain activation are required. This chapter describes two signal detection models; ANOVA, which is a pure signal detection method and Selective Averaging which also deals with overlapping BOLD-responses.

4.1 ANOVA [12]

Event-related experiments allows for the signal to be present in a small number of time points, thereby enabling investigation of individual trials. Analysis of variance (ANOVA) relies only on the timing of the start of each trial and thus makes no assumptions about the temporal shape of the activation. This makes it possible to detect many different activation patterns. The main goal is to detect voxels in which the time course shows a repeatable response to a particular type of stimuli. The haemodynamic response consists not only of the genuine response to the stimuli in the activated voxels, but also of random fluctuations due to uncorrelated physiological events and noise in the images. Since noise in fMRI data is assumed to have a normal distribution, averaging across trials reduces the magnitude of the noisy component, but not that of the repeated signal (see Figure 4.1).

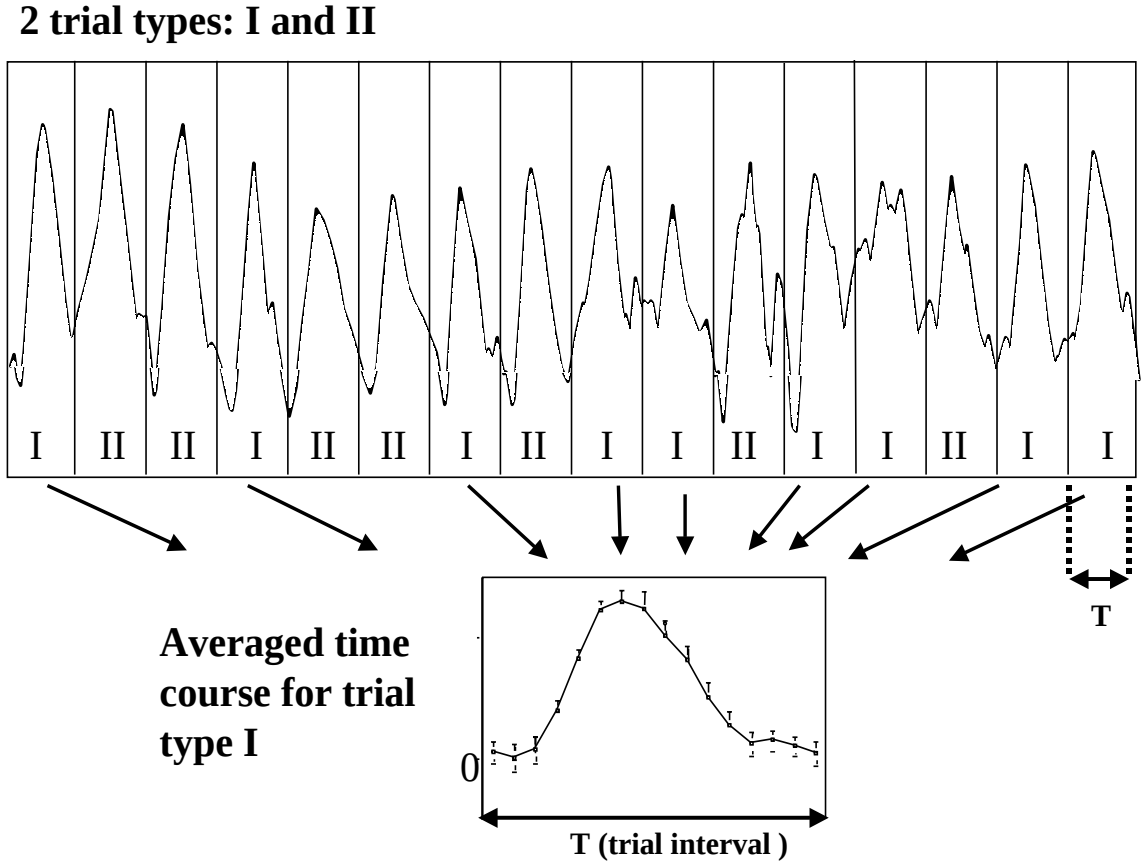

Figure 4.1: Averaged responses in er-fMRI. Trial types I and II. Averaging is performed over all trials of the same type. The magnitude of the noisy component is reduced, but not that of the repeated signal (Modified from R. Buckner, HBM 2000).

Description of method

An experiment may consist of one or several different trial types, randomly intermixed. The design should be such that each trial is presented after a sufficiently long interval to allow the BOLD-response to return to baseline between trials. The data for each trial type are collected and analyzed separately.

Let u_{ij} refer to the pixel intensity at the i-th time point after the stimulus and of the j-th trial of an experiment with n trials and m time points in each single trial:

$$
\begin{array}{cccccccc}
 & & & Trial & & & & \\
 & u_{11} & u_{12} & \ldots & u_{1j} & \ldots & u_{1n} & \overline{u}_1 \\
 & u_{21} & u_{22} & \ldots & u_{2j} & \ldots & u_{2n} & \overline{u}_2 \\
Time & \ldots & \ldots & \ldots & \ldots & \ldots & \ldots & \ldots \\
 & u_{i1} & u_{i2} & \ldots & u_{ij} & \ldots & u_{in} & \overline{u}_i \\
 & \ldots & \ldots & \ldots & \ldots & \ldots & \ldots & \ldots \\
 & u_{m1} & u_{m2} & \ldots & u_{mj} & \ldots & u_{mn} & \overline{u}_m \\
 & & & & & & & \overline{\overline{u}}
\end{array}
$$

The *null hypothesis* states that there are no significant differences in the time point means, $\overline{u}_i$. To test this hypothesis, two estimates of the time point means are compared, the first based on variance *between* time points and the second based on variance *within* the same time point.

Using standard statistical procedures, we begin by calculating the variance within the same time point across all trials of the same type. The mean, $\overline{u}_i$ and mean of means, $\overline{\overline{u}}$, is calculated from

$$\overline{u}_i = \frac{1}{n}\sum_{j=1}^{n} u_{ij}\ , \qquad \overline{\overline{u}} = \frac{1}{m}\sum_{i=1}^{m} \overline{u}_i\ ,$$

and the variance, $s^2_{\overline{u}}$, of time point means is given by

$$s^2_{\overline{u}} = \sum_{i=1}^{m} \frac{(\overline{u}_i - \overline{\overline{u}})^2}{m-1}.$$

Let $\hat{\sigma}^2_B$ denote mean variance *between* time points and $\hat{\sigma}^2_W$ mean variance *within* time points. Assuming

$$\sigma^2_{\overline{u}} = \frac{\sigma^2_B}{n},$$

mean variance *between* time points, $\hat{\sigma}^2_B$, can be approximated by

$$\hat{\sigma}^2_B = n \cdot s^2_{\overline{u}} = n \cdot \sum_{i=1}^{m} \frac{(\overline{u}_i - \overline{\overline{u}})^2}{(m-1)}$$

with $(m-1)$ degrees of freedom.

The variance *within* time points, s^2_i, is calculated from

$$s^2_i = \sum_{j=1}^{n} \frac{(u_{ij} - \overline{u}_i)^2}{n-1}, \quad i = 1, ..., m$$

and mean variance *within* time points is thus given by

$$\hat{\sigma}_W^2 = \sum_{i=1}^{m} \sum_{j=1}^{n} \frac{(u_{ij} - \overline{u}_i)^2}{m(n-1)}$$

with $m(n-1)$ degrees of freedom. $\hat{\sigma}_W^2$ is referred to as variance of the unaveraged data set [13], or unexplained variance [44] because it represents random variations that cannot be systematically explained. Accordingly, $\hat{\sigma}_B^2$ is referred to as variance of the averaged data set or explained variance.

The ratio F, which is the variance of the averaged data set to the variance of the unaveraged data set, is calculated for each voxel in the image. The function

$$F = \frac{\hat{\sigma}_B^2}{\hat{\sigma}_W^2} \tag{4.1}$$

has a Fisher-distribution (see Appendix A.2) with $(m-1)$ and $m(n-1)$ degrees of freedom. Any signal change that is time locked to the stimulus will result in a larger value of $\hat{\sigma}_B^2$ than expected under the null hypothesis. For voxels in regions with only random noise the ratio will be around $1/n$, where n is the number of trials averaged together. Voxels in regions of activation will have a significantly higher ratio due to the stimulus-locked change in the BOLD-response.

P (probability) values are calculated for each voxel yielding a parametric statistical map (SPM) where each voxel in the imaged volume is assigned a value on the likelihood that the null hypothesis is false. By tresholding the SPM and highlighting areas of the brain that can confidently be labeled as active, localization and comparison of brain function can be investigated.

4.2 Selective Averaging [14]

Averaging across trials is used to reduce noise in fMRI images. Dale and Buckner [14] have explored whether averaging techniques similar to those applied in event-related potential (ERP) experiments can be used to demonstrate BOLD responses to rapidly intermixed trials. In these paradigms the trials are closely spaced and the haemodynamic responses to adjacent trials may overlap distorting the averages for the selected trial type (selective averaging). One could choose to present the trials sufficiently apart so that their responses do not overlap. This will, however, reduce the total number of trials and thereby the power of the test. A more attractive solution, illustrated in Figure 4.2, would be to present closely spaced trials, and then apply methods for removing overlap. This requires a model for how the measured haemodynamic response to a sequence of events relates to the response to each individual event.

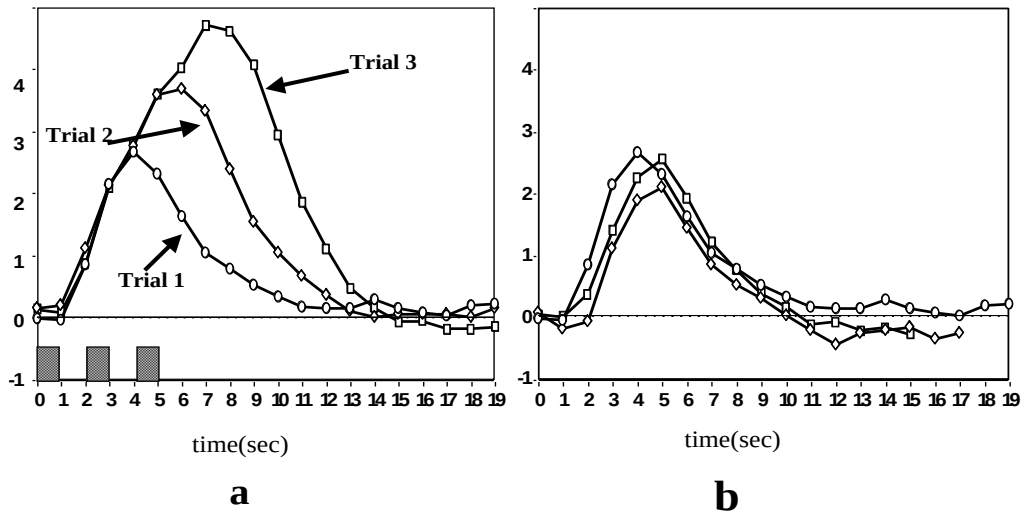

Figure 4.2: Responses to three closely spaced trials. (a) the observed responses and (b) the averaged responses

Description of method

The sampled fMRI time series are sorted by trial type after which the average and variance of the fMRI time courses are estimated for each voxel. Let $t_{i,k}$ denote the start-time of the

k^{th} trial of type i, and $s_{t_{i,k}+j}$ refer to the $(t_{i,k}+j)^{th}$ sample of the signal. We can then arrange the data from the n_i trials of type i as follows :

$$
\begin{array}{cccccccc}
 & & Trials\ of & type\ i & & & & \\
 & s_{t_{i,1}+1} & s_{t_{i,2}+1} & \cdots & s_{t_{i,k}+1} & \cdots & y_{i,1} \\
 & s_{t_{i,1}+2} & s_{t_{i,2}+2} & \cdots & s_{t_{i,k}+2} & \cdots & y_{i,2} \\
Time & \cdots & \cdots & \cdots & \cdots & \cdots & \cdots \\
 & s_{t_{i,1}+j} & s_{t_{i,2}+j} & \cdots & s_{t_{i,k}+j} & \cdots & y_{i,j} \\
 & \cdots & \cdots & \cdots & \cdots & \cdots & \cdots
\end{array}
$$

The average BOLD response, $y_{i,j}$, for trial type i at time j is computed by

$$y_{i,j} = \frac{\sum_k^{n_i} s_{t_{i,k}+j}}{n_i} \tag{4.2}$$

and the associated variance estimate $\sigma_{i,j}^2$ is

$$\sigma_{i,j}^2 = \frac{\sum_k^{n_i} (s_{t_{i,k}+j} - y_{i,j})^2}{n_i - 1} \tag{4.3}$$

where $t_{i,k}$ is the start-time of the k^{th} trial of type i, and $s_{t_{i,k}+j}$ refers to the $(t_{i,k}+j)^{th}$ sample of the signal. The average, $y_{i,j}$, and variance, $\sigma_{i,j}^2$, are weighted by their corresponding number of degrees of freedom (n_i and $(n_i - 1)$, respectively). To arrive at a statistical activation map, calculations of the covariance between the averaged *observed* signal and a normalized *predicted* BOLD-response function is performed.

The predicted BOLD-response function is modeled with a Gaussian function:

$$g(t) = \left(\frac{(t-\delta)}{\tau}\right)^2 e^{\frac{-(t-\delta)}{\tau}} \tag{4.4}$$

where $\delta = 2.5$ seconds and $\tau = 1.25$ seconds [14].

The average of the *predicted* response, $\overline{g}$ is calculated from

$$\overline{g} = \frac{1}{m}\sum_{j=1}^{m} g_j \tag{4.5}$$

where g_j denotes the predicted fMRI response at the $j-th$ time point and m is the number of time points in a single trial.

Similarly, the average of the *observed* signal, $\overline{y}$, for a specific trial type i, is calculated from

$$\overline{y} = \frac{1}{m} \sum_{j=1}^{m} y_j \tag{4.6}$$

where y_j denotes the observed fMRI response at the $j - th$ time point.

To obtain a good measure of how the observed signal relates to the predicted signal, the correlation between them is computed. The correlation, q, given by

$$q = \frac{\sum_j^m (y_j - \overline{y})(h_j - \overline{h})}{\sqrt{\frac{\sum_j^m \sigma_j^2}{m}} \sqrt{\sum_j^m (h_j - \overline{h})^2}}, \tag{4.7}$$

is assumed be Student's t distributed with degrees of freedom equal to the number of degrees of freedom for σ_j^2 [14].

Chapter 5

Description of the BOLD response in fMRI

The models described so far have been aimed primarily at detecting the BOLD response and the amount of this activation. They do not explore the shape properties (time course) of the BOLD responses. Probing the secrets of cerebral activity requires, however, information about both the spatial and the temporal properties of the BOLD response. In the process of extracting the temporal properties of the BOLD-response, the modulation of the HRF must be considered with great care. To avoid warped estimates of the true response, it is desirable that the HRF-models should span the space of all viable responses.

In this chapter the focus will be on the estimation of haemodynamic parameters. For simplicity, the locus of activation is assumed to be known, determined either from using one of the models already described or a suitable software package (e.g. SPM99, see Appendix A.3). The signal *detection* problem is thus separated from the signal *description* problem.

The first two models, the Nonlinear Least Squares Model (Section 5.1) and the Kruggel & Cramon Model (Section 5.2) apply a parametric modeling function for the HRF. They also both obtain estimates on the model parameters in a weighted least squares approach. However, because they differ in the way they deal with noise, and for reasons of clarity they are treated as separate models. Experiments with both these methods have been performed and will be presented in Chapter 7. The last section describes the Convolved Compartment Model in which a physiological modeling function is employed. Experiments with this model is described in Chapter 7.

5.1 Nonlinear Least Squares Model

In this section a straight forward nonlinear regression model of the form

$$x(t) = g(t, \boldsymbol{\theta}) + \epsilon(t), \quad \epsilon \sim N(0, \sigma) \tag{5.1}$$

is explored. Here $x(t)$ is the observed BOLD-response at time t, $g(t, \boldsymbol{\theta})$ is the modeling function with the parameter vector $\boldsymbol{\theta} = (\theta_1, \ldots, \theta_p)$ and $\epsilon(t)$ is the stochastic part (zero mean, Gaussian noise).

Any of the parametric modeling functions described in Section 3.2 can be used as the HRF function, $g(t, \boldsymbol{\theta})$, in Equation (5.1). For the HRF of this model we chose the Gaussian function (Equation (3.6)). This choice is based on the simplicity of the Gaussian and the ability to separately account for characteristics such as *dispersion* and *lag*, which might reflect properties of neuronal activity. Averaging over all trials for each specific trial type is performed for each voxel in a ROI time series. For an observed BOLD-response with m trials and l time steps per trial we introduce the matrix $\mathbf{X}$:

$$\mathbf{X} = \begin{bmatrix} x_{11} & x_{12} & \ldots & \ldots & x_{1l} \\ x_{21} & x_{22} & \ldots & \ldots & x_{2l} \\ \ldots & \ldots & \ldots & \ldots & \ldots \\ \ldots & \ldots & \ldots & \ldots & \ldots \\ x_{m1} & x_{m2} & \ldots & \ldots & x_{ml} \end{bmatrix}$$

Since noise in fMRI time series can, at first approximation, be modeled as additive, independent and identically distributed Gaussian, averaging over multiple trials will potentially increase the Signal to Noise Ratio (SNR, see Section 2.2.8). The averaged BOLD-response per voxel and per trial type, $\overline{\mathbf{x}} = [\overline{x}_1, ..., \overline{x}_l]$, obtained by

$$\overline{x}_j = \frac{1}{m} \sum_{i=1}^{m} x_{ij}, \quad j = 1, .., l \ ,$$

is approximated by determining the parameters in the chosen HRF-model. One set of parameter estimates is obtained for each voxel in all ROI time series and for each trial type. This approach is potentially capable of displaying differences between different activated brain regions and different trial types.

HRF-models where $g(t, \boldsymbol{\theta}$ is nonlinear with respect to the parameters, $\boldsymbol{\theta} = (\theta_1, \ldots, \theta_p)$, require a nonlinear estimation scheme. Using a least squares approach, the problem becomes one of selecting the elements of $\boldsymbol{\theta}$ that minimizes the function

$$D(\boldsymbol{\theta}) = \sum_{t=1}^{l} \left(\frac{x_t - g_t(\boldsymbol{\theta})}{\sigma_t} \right)^2 \tag{5.2}$$

in which σ denotes the variances of the residuals. Since noise is normally and identically distributed, with fixed variance $\sigma_t = \sigma$, the minimization problem in Equation (5.2) reduces to :

$$D(\boldsymbol{\theta}) = \sum_{t=1}^{l} (x_t - g_t(\boldsymbol{\theta}))^2 \tag{5.3}$$

A brief outline of the solution to Equation (5.3) now follows [20]. Expanding $D(\boldsymbol{\theta})$ around the point $\boldsymbol{\theta}_0$ to a second order gives

$$D(\boldsymbol{\theta}) = D(\boldsymbol{\theta}_0) + [\nabla D(\boldsymbol{\theta}_0)]\,(\boldsymbol{\theta} - \boldsymbol{\theta}_0) + \frac{1}{2}(\boldsymbol{\theta} - \boldsymbol{\theta}_0)\,\mathbf{H}\,(\boldsymbol{\theta} - \boldsymbol{\theta}_0), \tag{5.4}$$

where ∇D represents the gradient of the residual and $\mathbf{H}$ its second derivative (the *Hessian*). Setting

$$\frac{\partial D}{\partial \boldsymbol{\theta}} = \frac{\partial D(\boldsymbol{\theta})}{\partial \boldsymbol{\theta}} + H(\boldsymbol{\theta} - \boldsymbol{\theta}_0) = 0 \tag{5.5}$$

gives the following iteration scheme for finding the minimum

$$\boldsymbol{\theta}_{new} = \boldsymbol{\theta}_{old} - \mathbf{H}^{-1}\,\frac{\partial D(\boldsymbol{\theta}_{old})}{\partial \boldsymbol{\theta}} \tag{5.6}$$

To avoid computing second derivatives it is common practice to approximate $\mathbf{H}$ by $\mathbf{J}^T\mathbf{J}$ where $\mathbf{J}$ denotes the Jacobian matrix of partial derivatives. Substitution yields a new formula:

$$\boldsymbol{\theta}_{new} = \boldsymbol{\theta}_{old} - [\mathbf{J}^T\,\mathbf{J}]^{-1}\mathbf{J}^T\,r \tag{5.7}$$

in which r denotes the residuals between the observed signal and the HRF with estimated values for $\boldsymbol{\theta}$. This is the Gauss-Newton method for nonlinear least squares fitting.

5.2 Kruggel & Cramon Model [27]

The signal description problem will now be further investigated in the Kruggel & Cramon Model [27]. This model differs from the Nonlinear Least Squares Model, presented in the previous section, in the way it deals with noise. Rather than attempting to reduce noise, by averaging over multiple trials, the noisy components are collectively modeled in a covariance matrix. The Kruggel & Cramon Model also differs from the Nonlinear Least Squares Model in that it estimates one parameter set for a cluster of voxels and for each separate trial. These clusters are called regions of interest (ROI's) and usually contain 6-9 voxels in a 2-dimensional grid. For a region to qualify as a ROI for the Kruggel & Cramon Model, certain membership criteria must be met. Two voxels are defined as first order neighbours if they share a side. Second order neighbours share a corner. First and second order neighbours are conventionally called *8-connected* (see Figure 5.1).

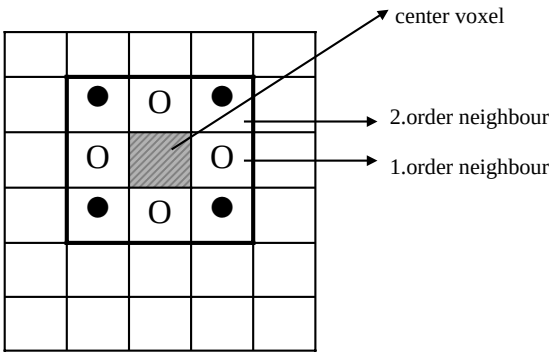

Figure 5.1: Neighbourhoods. First order neighbours share a side and second order neighbours share a corner.

Voxels that are to be defined within a ROI must be 8-connected and, furthermore, before a region is defined as a ROI, similarity measures (usually involving mean signal intensity level) must be investigated. On the basis of these similarity criteria, suitable voxels can be merged into a ROI. In the following a *ROI* denotes a set of voxels within one trial interval and a *ROI time series* refers to a set of voxels over a sequence of trials. A description of the Kruggel & Cramon Model now follows below.

Description of method

Let S be a vector of k 8-connected voxels from a region of interest, and T a vector of l discrete time steps for one specific experimental trial. The observed signal, $y(s,t)$ is collected in a matrix,

$$\mathbf{y} = \begin{bmatrix} y_{11} & y_{12} & \cdots & \cdots & y_{1l} \\ y_{21} & y_{22} & \cdots & \cdots & y_{2l} \\ \cdots & \cdots & \cdots & \cdots & \cdots \\ \cdots & \cdots & \cdots & \cdots & \cdots \\ y_{k1} & y_{k2} & \cdots & \cdots & y_{kl} \end{bmatrix}$$

The general model with $s \in S$ and $t \in T$ is given by

$$y(s,t) = g(t,\boldsymbol{\theta}) + \epsilon(s,t) \tag{5.8}$$

in which $g(t,\boldsymbol{\theta})$ is the modeling function, $\boldsymbol{\theta} = (\theta_1, \ldots, \theta_p)$ is a parameters vector of length p and $\epsilon(s,t)$ is the stochastic part. We define

$$\mathbf{Y} = [y_{11}, ..., y_{1l}, y_{21}, ..., y_{2l}, ..., y_{k1}, ..., y_{kl}]$$

$$\mathbf{g}_i = g(t_1,\boldsymbol{\theta}), ..., g(t_l,\boldsymbol{\theta}) \;\; and \;\; \mathbf{G}(\boldsymbol{\theta}) = [\mathbf{g}_1, ..., \mathbf{g}_k].$$

It has been shown that the stochastic part in preprocessed fMRI data have a normal distribution with zero mean and covariance $\mathbf{V}$ (see [27] and references therein). It is further assumed to be independent of the BOLD-response and stationary with respect to time. It follows that $\mathbf{Y} \sim N_n(\mathbf{G}(\boldsymbol{\theta}), \mathbf{V})$ and the corresponding probability density function of the normal distribution is formulated as

$$N_n(\mathbf{G}(\boldsymbol{\theta}), \mathbf{V}) = \frac{1}{(2\pi)^{1/2}(det\mathbf{V})^{1/2}} \, e^{1/2(\mathbf{Y}-\mathbf{G}(\boldsymbol{\theta}))^T \mathbf{V}^{-1}(\mathbf{Y}-\mathbf{G}(\boldsymbol{\theta}))}. \tag{5.9}$$

In search of the best fit between the model, $g(t,\boldsymbol{\theta})$, and the observed BOLD-response, $y(s,t)$, it suffices to minimize the exponential term of Equation (5.9). The p model parameters are thus obtained by minimizes

$$D(\boldsymbol{\theta}) = (\mathbf{Y} - \mathbf{G}(\boldsymbol{\theta}))^T \mathbf{V}^{-1} (\mathbf{Y} - \mathbf{G}(\boldsymbol{\theta})). \tag{5.10}$$

The number of equations should exceed the number of model parameters, that is $p < n = k \times l$, where k is the number of voxels and l the number of timesteps. The Gaussian function given in Equation (3.6) was chosen for the modulation of the HRF.

Studies of the covariance structure in fMRI data (see [27] and references therein) have found that the BOLD-response, $y(s,t)$, is autoregressive, that is, it depends on the external input stimuli and $y(s,t-1)$. For a weakly stationary process the correlation between residuals $\epsilon(s_0,t_0)$ and $\epsilon(s_1,t_1)$ depend only on the distance between them in time and space. Hence, the correlation matrix $\mathbf{V}$ is defined by the variance of the residuals (γ_2^2) and the $lag-1$ autocorrelation in the x,y and t directions. For the estimation scheme in Equation (5.10) it is required that $\mathbf{V}$ has an inverse, and consequently, $\mathbf{V}$ must be nonsingular. The correlation coefficients are estimated separately in time and space, yielding a spatial correlation matrix, $\mathbf{V}_S$, and a temporal correlation matrix, $\mathbf{V}_T$. $\mathbf{V}^{-1}$ is given by

$$\mathbf{V}^{-1} = \frac{1}{\gamma_2^2}\left(\mathbf{V}_S^{-1} \odot \mathbf{V}_T^{-1}\right) \tag{5.11}$$

in which $\odot$ denotes the Kronecker product[1].

The temporal $lag-1$ autocorrelation coefficient is computed from the formula :

$$\hat{\rho}_T = \frac{\sum_{s\in S}\left(\sum_{t=1}^{l-1}\epsilon(s,t)\;\epsilon(s,t-1)\right)}{\sum_{s\in S}\left(\sum_{t=0}^{l-1}\epsilon(s,t)^2\right)} \tag{5.12}$$

and the temporal correlation matrix is set up

$$\mathbf{V}_T^{-1} = \frac{1}{(1-\rho_T^2)}\begin{pmatrix} 1 & -\rho_T & 0 & \ldots & 0 \\ -\rho_T & 1+\rho_T^2 & -\rho_T & \ldots & 0 \\ 0 & -\rho_T & 1+\rho_T^2 & \ldots & 0 \\ & & & \ldots & \\ 0 & & & \ldots & 1 \end{pmatrix} \tag{5.13}$$

To find the spatial correlation matrix is more involved. Here we closely follow the paper of Kruggel & Cramon with references to [40]. First, the subsets of all pairs of sites located with the same absolute distance are collected, that is :

$$S_{h,v} = \{(s_i,s_j) \mid s_i, s_j \in S\}$$

where $h = H(s_i,s_j), v = V(s_i,s_j)$ returns the absolute distance in the x and y directions. The correlation coefficients for all possible combinations of h and v are then computed:

$$\hat{\rho}_{h,v} = \frac{\sum_{t\in T}\left(\sum_{s_i,s_j\in S_{h,v}}\epsilon(s_i,t)\;\epsilon(s_j,t-1)\right)}{\sum_{t\in T}\left(\sum_{s_i,s_j\in S_{h,v}}\epsilon(s_i,t)^2\right)} \tag{5.14}$$

[1]The Kronecker product of the two matrices $\mathbf{S}$ and $\mathbf{T}$ is the $k^2\times l^2$ matrix $\mathbf{V}$ obtained by replacing the entry s_{ij} of S with the matrix $s_{ij}\mathbf{T}$

The correlation coefficients, ρ_X and ρ_Y, are found by minimizing

$$\sum_{h,v}(\hat{\rho}_{h,v} - \rho_X^h \, \rho_Y^v)^2, \tag{5.15}$$

after which the spatial correlation matrix is set up as

$$\mathbf{V}_S = \begin{pmatrix} 1 & \rho_S(s_0, s_1) & \rho_S(s_0, s_2) & ... & \rho_S(s_0, s_{k-1}) \\ \rho_S(s_0, s_1) & 1 & \rho_S(s_1, s_2) & ... & \rho_S(s_1, s_{k-1}) \\ \rho_S(s_0, s_2) & \rho_S(s_1, s_2) & 1 & ... & \rho_S(s_2, s_{k-1}) \\ ... & ... & ... & ... & ... \\ \rho_S(s_0, s_{k-1}) & ... & ... & ... & 1 \end{pmatrix} \tag{5.16}$$

in which

$$\rho_S(s_i, s_j) = \rho_X^h \, \rho_Y^v.$$

Optimization

When the covariance matrix has been set up, the next step is to minimize $D(\boldsymbol{\theta})$ in Equation (5.10). Optimization is the process in which the "best" parameters for the function $D : R^n \rightarrow R$ are chosen. These parameters are often found where D takes on a minimum or a maximum, commonly referred to as an extreme point. An extreme point may be either global or local. Ideally, the optimization method should converge to the optimal solution, and not get caught in a local minima or maxima. Optimization methods can be divided into two main categories; *gradient methods*, in which an approximation of the function's derivative is required, and *direct search methods* where no derivatives are necessary.

Kruggel & Cramon suggests the Nelder & Mead downhill simplex method for the optimization of the present model [27]. Nelder& Mead downhill simplex method is a direct search method. A simplex is a geometrical figure that has one more vertex that dimension; a triangle in 2D, a tetrahedron in 3D, and so on. An initial simplex is formed by picking a random location and taking unit vectors for the edges. The function being minimized is then evaluated at the D+1 vertices of the simplex. An iterative procedure will at each step attempt to improve the position of the "worst" vertex. During this process the worst vertex is moved to a new location via a series of update moves (reflection, reflection and expansion, contraction, multiple contraction, see Figure 5.2). If the move results in a better position, the vertex position is updated. The procedure continues until a stopping criteria is reached. A detailed description of the method can be found in [20]. Direct search methods are usually preferable if derivatives cannot be accurately computed and

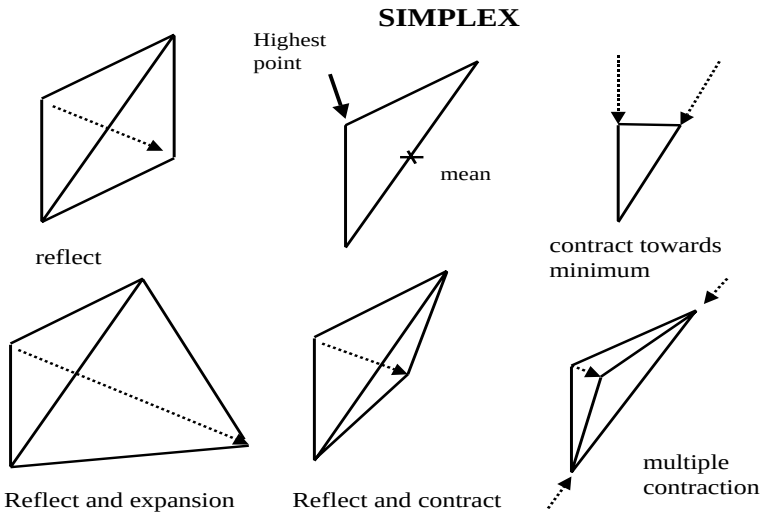

Figure 5.2: Downhill simplex update moves

numerical approximations of derivatives are expensive and the values of D are noisy, which is the case for fMRI-data. The Gaussian function (Equation 3.6) has only four parameters and numerical approximation of the derivatives are readily computed. Furthermore, the Kruggel & Cramon Model presents a way of dealing with noise. It is therefore relevant to explore whether gradient based methods may be employed for the parameter estimation of this model. The Levenberg-Marquardt method, as implemented in the Matlab function `lsqnonlin` (see Appendix A.4), was chosen for this purpose.

The Gauss-Newton method (described in Section 5.1) converges quickly close to a minimum, it is, however, extremely unreliable far from a minimum. The Levenberg-Marquardt (LM) algorithm solves this problem by switching between gradient descent, which takes a step in the direction in which the error is decreasing most rapidly far away, and Gauss-Newton near a minimum. LM modification adds $\mu\,\mathbf{I}$ to $\mathbf{J}^T\,\mathbf{J}$ in Equation (5.7), adjusting the parameter μ continuously :

$$\boldsymbol{\theta}_{new} = \boldsymbol{\theta}_{old} - [\mathbf{J}^T\,\mathbf{J} + \mu\,\mathbf{I}]^{-1}\mathbf{J}^T\,r. \tag{5.17}$$

For $\mu = 0$ the algorithm is pure Gauss-Newton, but as $\mu \to \infty$ the algorithm descends by use of the gradient and thus becomes the method of gradient descent. If a step reduces the error then μ is decreased because Gauss-Newton is best close to a minimum. If, on the other hand, a step increases the error then μ is increased since gradient descent is

better. However, special attention regarding starting conditions are necessary. Whereas the function to minimize may possess many minima, the Levenberg-Marquardt method will only find the local minima closest to the starting conditions. The Levenberg-Marquardt method therefore requires a starting value near the desired minimum, as well as a relative smooth function.

5.3 Convolved Compartment Model [28]

The BOLD-response is interpreted as a convolution between neuronal activation and haemodynamics, and a major problem with fMRI data is that they reflect changes in the Blood Oxygenation Level, and not the desired neuronal activation. The question arises as to what extent it is possible to distinguish the "neuronal" from the "vascular" component. A deconvolution of the BOLD-response could prove useful in the search for the characteristics of neuronal activation. A method which attempt to model this convolution process will now be presented.

Description of method

To accommodate the convolution between neuronal activity and haemodynamics, Equation (3.3) is reformulated as

$$y(s,t) = f(t) \star n(t) + b + \epsilon(s,t) \tag{5.18}$$

where $y(s,t)$ is the observed signal intensity at site s and time t, $n(t)$ denotes a *neuronal stimulation* function, $f(t)$ the haemodynamic modulation function, b is a baseline term and $\star$ is the convolution operator (cfr. Appendix A.1). If we include the parameter vector $\boldsymbol{\theta} = [a, t_0, t_1, b, \gamma_0, \gamma_1, \gamma_2, \gamma_3]$, Equation (5.18) can be written

$$y(s,t;a,t_0,t_1,b,\gamma_0,\gamma_1,\gamma_2,\gamma_3) = f(t;\gamma_0,\gamma_1,\gamma_2,\gamma_3) \star n(t;a,t_0,t_1) + b + \epsilon(s,t). \tag{5.19}$$

The neuronal stimulation function is modeled as a simple box-wave function:

$$n(t) = \begin{cases} a & if\ t_0 \leq t < t_0 + t_1 \\ 0 & \text{otherwise} \end{cases} \tag{5.20}$$

This gives three neuronal parameters, a: gain of neuronal response, t_0: time of onset and t_1: duration of neuronal response. In search of the vascular parameters, the BOLD response is thought of as an endogenous contrast. Exogenous contrast such as radioactive markers or pharmaceuticals have been modeled by compartment models since 1920 (see [28] and references therein). Compartments refer to body subspaces such as tissue or vasculature. Taking advantage of this modeling approach, and assuming that the measured BOLD-response is proportional to the oxyhaemoglobin concentration, a compartment model should reflect the temporal oxygen flow pattern. Increasing the proportion of oxyhaemoglobin leads to decreased spin-spin dephasing and thereby a stronger signal (see Section 2.4.1). Thus, if the concentration of oxyhaemoglobin in a compartment increases, so will also the signal contribution from the particular compartment.

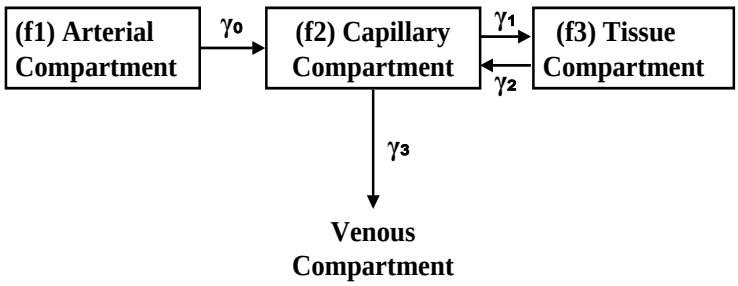

Figure 5.3: Movement of oxygen in vascular and tissue compartments. γ_0 denotes the rate at which oxyhaemoglobin enters the capillary compartment. Rates γ_1 and γ_2 reflect the oxyhaemoglobin exchange between capillaries and tissue, and γ_3 is the rate at which oxyhaemoglobin flows into the venous system. Modified from Kruggel & Cramon[1999]

The Convolved Compartment Model consists of two vascular and one tissue compartment. The signal contribution from the venous side of the vascular bed is ignored. An illustration of the model is given in Figure 5.3. Oxyhaemoglobin is transported from the arterial compartment into the capillary compartment at rate γ_0. Rates γ_1 and γ_2 reflect the oxyhaemoglobin exchange between capillaries and tissue, and γ_3 is the rate at which oxyhaemoglobin flows into the venous system.

The model is described by the following linear system of differential equations[2]:

$$\frac{df_1}{dt} = -\gamma_0 f_1, \quad f_1(0) = 1$$

$$\frac{df_2}{dt} = \gamma_0 f_1 + \gamma_2 f_3 - (\gamma_1 + \gamma 3) f_2, \quad f_2(0) = 0$$

$$\frac{df_3}{dt} = \gamma_1 f_2 - \gamma_2 f_3, \quad f_3(0) = 0$$

The solution to this system can be written as a sum of exponentials for the $i-th$ compartment:

$$f_i = k_{i1} e^{-\gamma_0 t} + k_{i2} e^{\lambda_0 t} + k_{i3} e^{\lambda_1 t}, \tag{5.21}$$

[2]A misprint in the last equation of this system, reading $\dot{f}_3 = \gamma_0 f_2 - \gamma_2 f_3$, was found in the paper [28].

in which the eigenvalues λ_0 and λ_1 are given by:

$$\lambda_0 = -0.5(\gamma_1 + \gamma_2 + \gamma_3 + \sqrt{(\gamma_1 + \gamma_2 + \gamma_3)^2 - 4\gamma_2\gamma_3}),$$

$$\lambda_1 = -0.5(\gamma_1 + \gamma_2 + \gamma_3 - \sqrt{(\gamma_1 + \gamma_2 + \gamma_3)^2 - 4\gamma_2\gamma_3})$$

and the $k_{i,j}$'s are[3]:

$$k_{1,j} = [1, 0, 0],$$

$$k_{2,j} = \left[\frac{\gamma_0(\gamma_2 - \gamma_0)}{(\gamma_0 + \lambda_0)(\gamma_0 + \lambda_1)}, \frac{\gamma_0(\gamma_2 + \lambda_0)}{(\gamma_0 + \lambda_0)(\lambda_0 - \lambda_1)}, \frac{\gamma_0(\gamma_2 + \lambda_1)}{(\gamma_0 + \lambda_1)(\lambda_1 - \lambda_0)}\right]$$

$$k_{3,j} = \left[\frac{\gamma_0\gamma_1}{(\gamma_0 + \lambda_0)(\gamma_0 + \lambda_1)}, \frac{\gamma_0\gamma_1}{(\gamma_0 + \lambda_0)(\lambda_0 - \lambda_1)}, \frac{\gamma_0\gamma_1}{(\gamma_0 + \lambda_1)(\lambda_1 - \lambda_0)}\right]$$

The parameter vector, $\boldsymbol{\theta}$, now consist of eight parameters: $[a, t_0, t_1, b, \gamma_0, \gamma_1, \gamma_2, \gamma_3]$, in which a, t_0 and t_1 are neuronal parameters, $\gamma_1 - \gamma_4$ are vascular transfer rates and b is the baseline. The convolution between the neuronal and vascular components $g(t, \boldsymbol{\theta}) = f(t) \star n(t)$, is defined as the definite integral:

$$g(T) = \int_0^T f(t)n(T - t)dt, \quad f, n, t \in [0, \mathcal{T}] \mapsto \mathcal{R} \tag{5.22}$$

in which the integral $[0, \mathcal{T}]$ corresponds to the time interval of one single trial. Based on Equation (5.20) and (5.22), $g(T)$ has the following properties:

$$g(T) = \begin{cases} 0 & 0 \leq T < t_0 \\ a \int_0^{T-t_0} f(t)dt & t_0 \leq T < t_0 + t_1 \\ a \int_{T-t_0-t_1}^{T-t_0} f(t)dt & T \geq t_0 + t_1 \end{cases} \tag{5.23}$$

where $f(t) = f_1(t) + f_2(t) + f_3(t)$. Integrating Equation (5.23) with regard to t yields :

$$\int_0^{T-t_0} f(t)dt = -\frac{\sum k_{i,1}}{\gamma_0}\left[e^{-\gamma_0(T-t_0)} - 1\right] + \frac{\sum k_{i,2}}{\lambda_0}\left[e^{\lambda_0(T-t_0)} - 1\right] + \frac{\sum k_{i,3}}{\lambda_1}\left[e^{\lambda_1(T-t_0)} - 1\right]$$

and

[3]In the paper [28] the denominator for the $k_{3,j}$ are $\gamma_0\gamma_1(\gamma_2 - \gamma_0)$, $\gamma_0\gamma_1(\gamma_2 + \lambda_0)$ and $\gamma_0\gamma_1(\gamma_2 + \lambda_1)$, respectively. We assume that this is a misprint.

$$\int_{T-t_0-t_1}^{T-t_0} f(t)dt = -\frac{\sum k_{i,1}}{\gamma_0}\left[e^{-\gamma_0(T-t_0)} - e^{-\gamma_0(T-t0-t1)}\right] + \frac{\sum k_{i,2}}{\lambda_0}\left[e^{\lambda_0(T-t_0)} - e^{\lambda_0(T-t0-t1)}\right]$$

$$+\frac{\sum k_{i,3}}{\lambda_1}\left[e^{\lambda_1(T-t_0)} - e^{\lambda_1(T-t0-t1)}\right]$$

We now need to estimate the eight parameters of the modeling function. Two different ways of dealing with noise have already been described:

- Averaging over multiple trials was described in Section 5.1. With the Convolved Compartment Model one could chose to perform both spatial and possibly temporal averaging over multiple trials in a ROI time series. Spatial averaging per trial in a ROI time series would give one parameter estimate per trial. If both spatial and temporal averaging are performed, one parameter estimate is obtained for each ROI time series. However, the number of observations per averaged trial (ROI) must exceed the number of model parameters. Since the number of observations per trial in er-fMRI experiments usually are between 4-12, the rather large number of eight parameters represents a limitation for this approach.

- Noise collectively modeled in a covariance matrix (Section 5.2). Kruggel & Cramon [28] suggests this approach for the present model. The function to minimize is given by

  $$D(\boldsymbol{\theta}) = (\mathbf{Y} - \mathbf{G}(\boldsymbol{\theta}))^T \mathbf{V}^{-1} (\mathbf{Y} - \mathbf{G}(\boldsymbol{\theta})), \tag{5.24}$$

  This estimation scheme gives one set of parameters for each separate trial in a ROI time series.

Part III

Experiments

Chapter 6

Applied Methods and Implementations

This chapter focuses on the specific implementation of methods described in Chapter 4 and 5. The models selected for experimental purposes of this work are as follows:

- Signal *detection* : ANOVA (Section 4.1)
- Signal *description*
  - Nonlinear Least Squares Model (Section 5.1)
  - Kruggel & Cramon Model (Section 5.2)
  - Convolved Compartment Model (Section 5.3)

All programs are implemented in Matlab (www.mathworks.com). Matlab, which is available on a number of platforms including Windows 95/98/2000, Macintosh, several Unix platforms and Linux, is especially suitable for matrix handling. Several toolboxes are available, including toolboxes for signal and image processing and statistical analysis. A number of Matlab functions have been included in the implementation of the models and will be referred to in the appropriate sections.

All data sets employed in this thesis have been preprocessed with the SPM99 software package (see Appendix A.3). Before proceeding with a detailed description of the selected models, a brief description of the SPM preprocessing procedure will therefore be given.

6.1 Preprocessing with SPM99

SPM99 is a software environment for the analysis of PET (Positron Emission computed Tomography) and fMRI neuro-imaging data. The software package contains functionalities

such as image display, image registration, image realignment and co-registration, nonlinear spatial normalization and statistical analysis.

The first step in the preprocessing procedure for an event-related fMRI experiment is to correct for differences in slice timing (*slice timing*). This problem arises because slices in a volume is acquired at slightly different times relative to the induced stimuli, yet model the same. SPM solves the slice timing issue by temporal interpolation. The second step is motion correction (*realignment*). Subject movement during the MR session is a major source of artifact in fMRI. Changes in signal intensity at the boarders of the brain, even upon very small movement, can be far greater than the BOLD response. Furthermore, the sensitivity of the analysis is determined by the amount of residual noise in the image series, and movement that is unrelated to the stimuli will add to the noise and reduce sensibility. The steps in motion correction are:

- Registration : determine the 6 parameters (translations and rotations in x,y and z directions) that describe the rigid body transformation which minimizes the sum of squared differences between each image and a reference image.

  These operations are represented as affine transformation matrices. *Translations* about all 3 axes are thus given by:

$$\begin{pmatrix} 1 & 0 & 0 & x_{transX} \\ 0 & 1 & 0 & y_{transY} \\ 0 & 0 & 1 & z_{transZ} \\ 0 & 0 & 0 & 1 \end{pmatrix}$$

  and the *rotations* about the x-axis(pitch), y-axis(roll) and the z-axis(yaw), are:

$$\underbrace{\begin{pmatrix} 1 & 0 & 0 & 0 \\ 0 & cos(\Phi) & sin(\Phi) & 0 \\ 0 & -sin(\Phi) & cos(\Phi) & 0 \\ 0 & 0 & 0 & 1 \end{pmatrix}}_{\text{Pitch}} \times \underbrace{\begin{pmatrix} cos(\Phi) & 0 & sin(\Phi) & 0 \\ 0 & 1 & 0 & 0 \\ -sin(\Phi) & 0 & cos(\Phi) & 0 \\ 0 & 0 & 0 & 1 \end{pmatrix}}_{\text{Roll}} \times \underbrace{\begin{pmatrix} cos(\Phi) & sin(\Phi) & 0 & 0 \\ -sin(\Phi) & cos(\Phi) & 0 & 0 \\ 0 & 0 & 1 & 0 \\ 0 & 0 & 0 & 1 \end{pmatrix}}_{\text{Yaw}}$$

- Transformation (*co-registration*): resampling of all the volumes according to the determined transformation parameters.

Normalization is an optional process in which images from different subjects are registered into roughly the same coordinate system. Since the data-sets in this thesis were to be analyzed individually (not compared to other subjects), there was no need to map the

images to a standard template. The normalization step was therefore omitted. Finally, the images are smoothed. *Smoothing*, which in SPM is a convolution between the sampled image and a Gaussian kernel, is performed to increase the Signal to Noise Ratio (SNR, see Section 2.2.8).

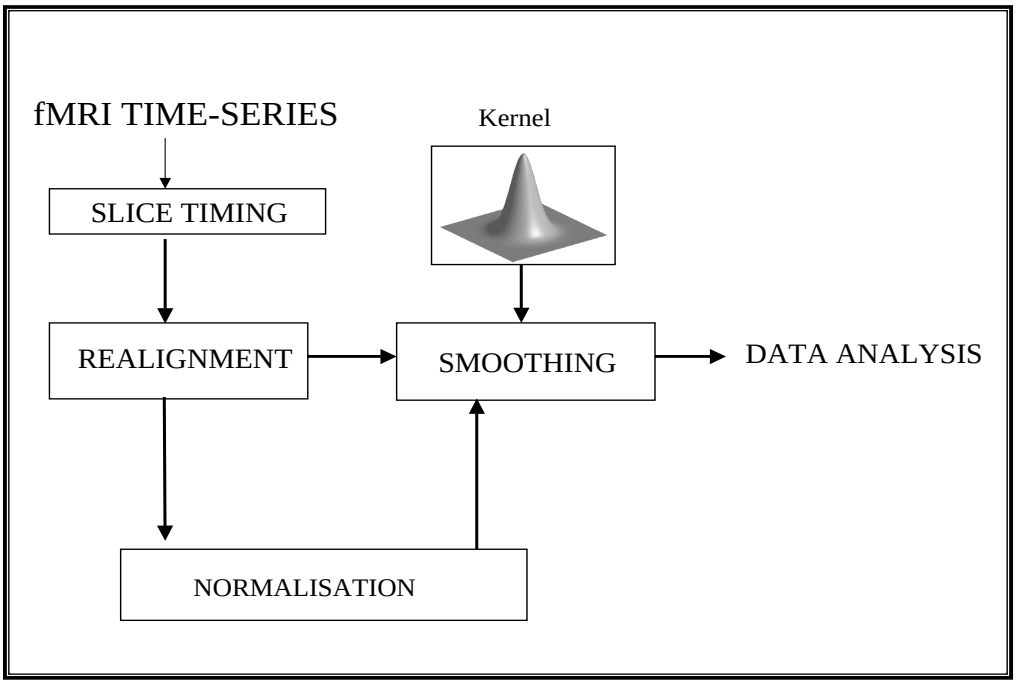

Figure 6.1: SPM preprocessing process. The fMRI time series is first subject to *slice-timing* in which data are corrected for the difference in the image acquisition times between slices. *Realignment* seeks to reduce noise (i.e. misregistration) related to movement. All volumes of the fMRI time series are aligned according to the first volume. This involves a spatial transformation to minimize the difference between two volumes. *Normalization* is the process of registering images from different subjects into roughly the same coordinate system. *Smoothing*, a low pass filtering in which the images are convolved with a kernel shaped according to the applied filter, is performed to to increase the SNR (see Section 2.2.8)

As an example of SPM analysis in terms of detection of activated voxels, a recent experimental study on dichotic listening (see below) was selected. We used a gradiant echo, EPI protocol, echo time TE = 60 msec, TR = 0.6 msec and flip angle = 90° (FOV = 220×220 mm), and a total of 472 echo planar images (EPI, see Section 2.2.7) were acquired. Each volume consisted of 9 slices of 64 ×64 voxel resolution and spatial resolution 3.44×3.44×5

mm, no gap between consecutive slices. A corresponding anatomical image (3D FLASH, see Section 2.2.7) was acquired in the same session.

While in the scanner, the subject was presented with dichotic listening tasks in which similar sounds (e.g ba, pa) is presented to both ears simultaneously. These sounds were also presented to the subject on a visual display. The subject was asked to determine which of the sounds he had heard. Presentation rate was a fixed interval of 21 seconds. The data set was preprocessed and analyzed with the SPM software package. Expected areas of activation include primary and secondary auditory cortex (see Figure 6.2). The activation map constructed with SPM is shown in Figure 6.3.

A general problem with auditory stimulus in fMRI experiments is that the level of background noise in the scanner is extremely high. This presumably leads to a constant activation in the auditory cortex. Over time, however, there will be a certain adaptation to the scanner noise which also has specific frequency characteristics. It should therefore in theory be possible to detect the activation that arises from the very brief auditory stimulus applied in this experiment.

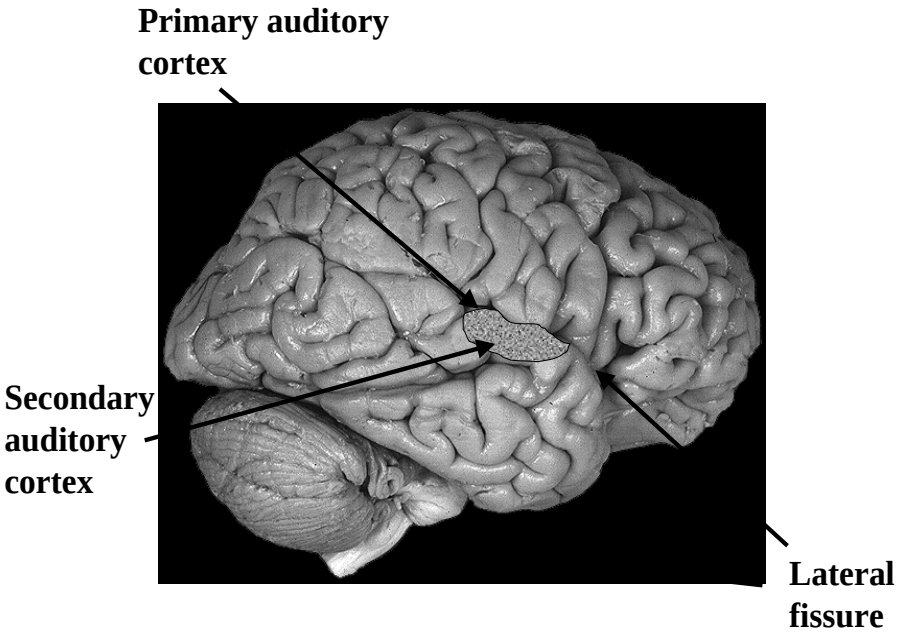

Figure 6.2: Auditory cortex

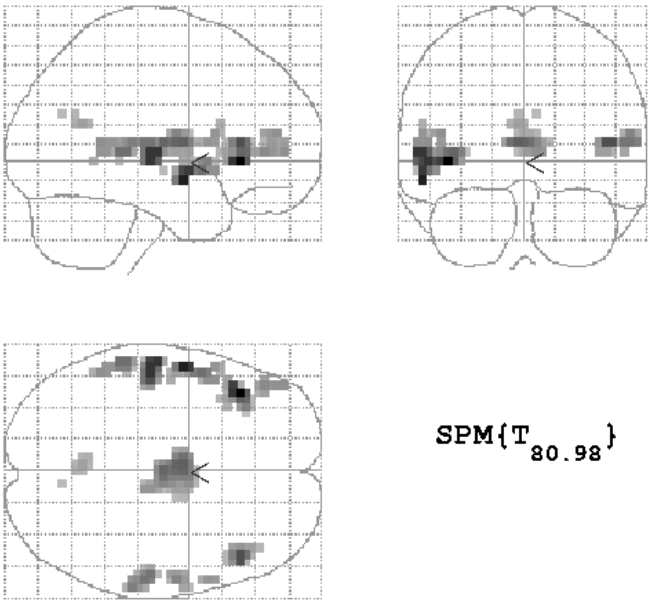

Figure 6.3: SPM activation map. SPM analysis in terms of detecting activated voxels in a dichotic listening study.

6.2 ANOVA

The ANOVA procedure is based on simple averaging theory (see [13] and references therein) and implementation is straightforward. A formal description of the method is given in Chapter 4.1. The ANOVA approach assumes that each time point is independent and the experimental design must therefore allow for the response to return to baseline between successive trials. If the duration of the BOLD-response is longer than the trial sampling period, the time points no longer can be considered independent. However, if the data have a high level of temporal connectivity, it has been suggested that a method of randomization be applied [13]. In short this means that the order of the time series for each separate trial is randomized prior to the processing and statistical analysis.

The F-ratio, given in Equation (4.1), differs with varying degrees of freedom in numerator and denominator (see Appendix A.2). For the current problem, the degree of freedom for the numerator is the number of time points minus one. For the denominator, the degrees of freedom is given by the total number of observations (number of trials $\times$ number of time points) minus the number of time points per trial [44].

To assess the validity of ANOVA with fMRI noise levels, the procedure was tested on real data. The data set, consisting of 45 volumes, each of $64 \times 64 \times 40$ matrix size, was analyzed with the SPM software package after which regions with activated voxels were excluded from further tests. All remaining voxel time series were submitted to the ANOVA procedure after which the resultant F-values were investigated. All test showed a good fit to the F-distribution, confirming the validity of the technique on fMRI data. An illustration is given in Figure 6.4.

The data should be organized such that all time points and all trials for each trial type are collected in a separate matrix. This $m \times n$ matrix, in which m is the number of time points in each trial and n is the number of trials, is taken as input to the Matlab m-file, `ihk_ANOVA`. Pseudo code for the algorithm follows below.

Pseudo code `ihk_ANOVA` :

INPUT:

- data ($[m \times n]$ data matrix where m is the number of time points in each trial and n is the number of trials)

OUTPUT:

- F (F-ratio)

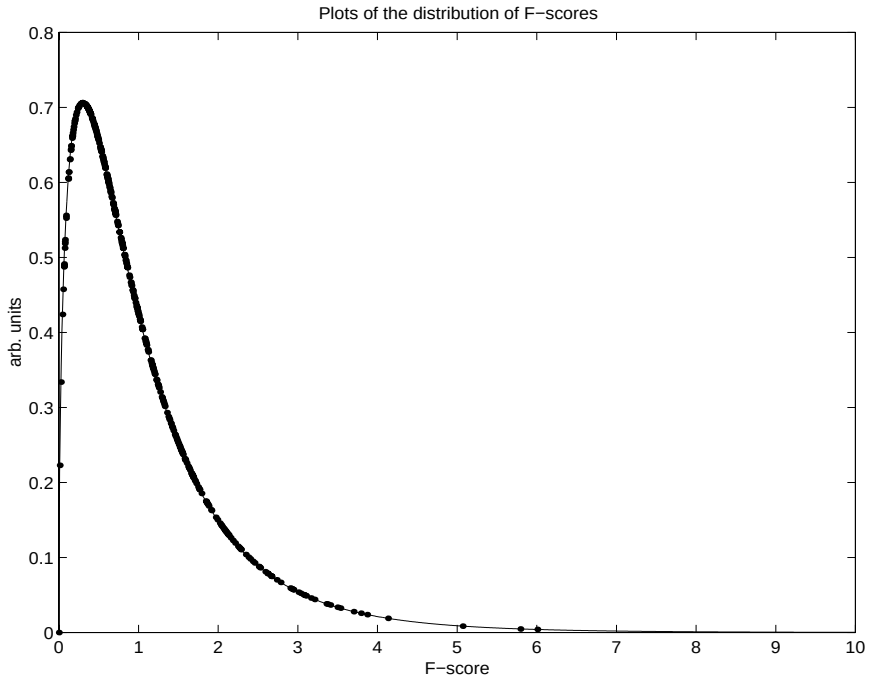

Figure 6.4: Plot of distribution of F-scores in fMRI noise. Validity of ANOVA tested with noise levels in real fMRI data. Non-activated voxel time series were submitted to the ANOVA procedure after which the resulting F-scores were plotted. F distribution with corresponding degrees of freedom is shown as a solid line.

compute time point means: TPM = mean(transpose(data))

compute mean of means: MOM = mean(TPM)

compute mean variance between time points MVB :

for all rows

    MVB = MVB + (TPM(row) - MOM)^2

end for

MVB = (MVB×n)/(m-1)

compute mean variance within time points MVW :

for all rows

    for all columns

        MVW = MVW + (data(row,column) - TPM(row))^2

    end for

end for

MVW = MVW/(m(n-1))

return F = MVB/MVW

6.3 Nonlinear Least Squares Model

The Nonlinear Least Squares approach is the least complex of the signal *description* models presented in this work. A general overview of this method is found in Chapter 5.1. In this section a more detailed description is presented. The Nonlinear Least Squares Model ignores all spatial and/or temporal correlations present in the noise. Therefore, it is important that the noisy component is reduced. This is achieved by performing an averaging over all trials of the same type (Single Trial Averaging) for each voxel. In order to reduce the noise to an acceptable level, a large number of trials are required for all trial types. In Single Trial Averaging the mean over all trials is computed for every voxel yielding one parameter (vector) estimate for each specific trial type. Given m trials per trial type and l time steps per trial, the averaged BOLD-response, $\overline{\mathbf{x}} = [\overline{x}_1, ..., \overline{x}_l]$, per voxel is given by

$$\overline{x}_j = \frac{1}{m} \sum_{i=1}^{m} x_{ij}, \quad j = 1, .., l \ ,$$

This approach is valid only under the assumption that identical trial types generate the same response in a specific voxel. To avoid adaptation to the imposed external stimulus it is required that the experiment is event-related with randomly intermixed trial types.

A Gaussian form was selected for the parametric modeling function. The Gaussian modeling function

$$g(t, \boldsymbol{\theta}) = \frac{\theta_0}{\theta_1} \ \exp\left(-\frac{(t-\theta_2)^2}{2\theta_1^2}\right) + \theta_3, \quad where \ \ t \in T, \tag{6.1}$$

has been preferred in many studies because of its ease of application and its ability to independently represent *lag* and *dispersion* [39]. In a physiological interpretation of the parameters *lag* (θ_2) can be understood as the time to maximum of the BOLD-response, whilst *dispersion* (θ_1) reflects the duration of the response. *Gain* (θ_0) has been proposed to reflect the energy consumption of an activated area and (θ_3) the baseline [39].

For the minimization of $D(\boldsymbol{\theta})$ in Equation (5.3), the Gauss-Newton method for nonlinear least squares fitting was employed. This procedure is implemented in `nlinfit` (see Appendix A.4). To test the validity of `nlinfit` with the Gaussian function (Equation (6.1)), various signals with known true parameters were constructed. Given these signals, `nlinfit` should be able to reproduce the true parameters. A slight modification of `nlinfit`, changing the convergence criteria from 10^{-4} to 10^{-12}, ensured an acceptable fit. The modified version, `ihk_nlinfit` yields parameter estimates that are identical with the true parameters with at least 14 decimals. The Matlab function `nlparci` (see Appendix A.4) was

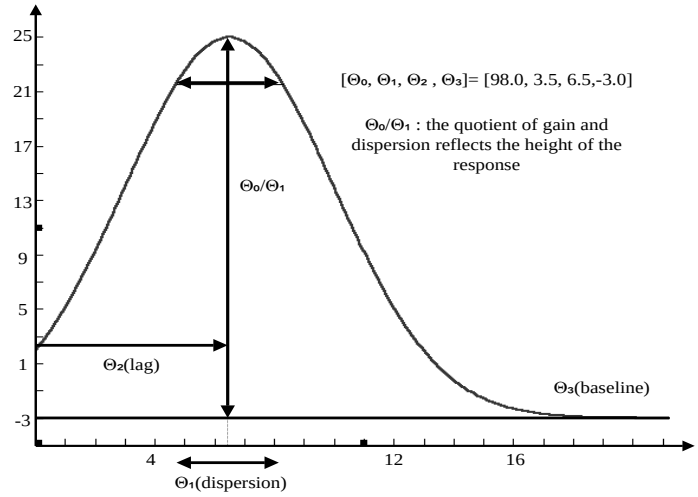

Figure 6.5: Gaussian function with physiological interpretations of the parameters:(θ_0) is assumed to reflect the energy consumption of an activated area, (θ_1) the duration of the response, (θ_2) the time to maximum of the BOLD-response and (θ_3) is the baseline.

employed for the computation of 95% confidence intervals on the p model parameters, $\boldsymbol{\theta} = (\theta_1, \ldots, \theta_p)$. Normality in the residuals for all ROI's were tested according to the Lilliefors and the Bera-Jarque tests implemented in the Matlab functions `lillietest` and `jbtest`, respectively (see Appendix A.4).

A brief outline of the MATLAB code follows below:

Matlab function `ihk_lsq` :

INPUT:

- ROI (matrix of data points in which rows represents voxels and columns represents time points. There are l time points in each trial. Consecutive trials must be such that the last time point in one trial is directly followed by the first time point in the next trial)
- t (vector with time interval for one trial, if e.g. $t = [0 : 2 : 22]$ then there are 12 time points and 2 seconds between each time point)
- start (starting values for the parameter vector)

OUTPUT:

- theta_est (vector with estimated parameters)
- conf_int (95% confidence interval for the parameter vector, theta_est)
- h_tab (table of results from Lilliefors and Bera-Jarque tests for normality in the residuals)

```
theta_est = [ ]; % matrix for estimated parameters
h_tab = [ ];
l=length(t)
[k, n] = size(ROI); % k voxels and n time points, n =l× number of trials

%Single Trial Averaging: compute mean over all trials
mean_ROI = [ ];
for voxel = 1:k
    ROI_voxel = [ ];
    for trial = 1:l:n
        if trial + (l-1) ≤ n
            ROI_voxel = [ROI_voxel; ROI(voxel,trial:(trial+(l-1)))];
        end if
    end for
    %compute the average over all timepoints
    mean_ROI(voxel,:) = mean(ROI_voxel);
end for

% nonlinear least-squares data fitting by the Gauss-Newton method
model = 'gaussmodelHR'; % Subroutine for use with ihk_nlinfit
res_after_est = [ ]; % matrix for residuals after estimation
conf_upper = [ ]; conf_lower = [ ];
for voxel = 1 : k
    [thetahat, resid, J] = ihk_nlinfit(t,mean_ROI(voxel,:), model, start);
    betaci = nlparci(thetahat, resid, J);
    conf_lower = [conf_lower; transpose(betaci(:,1))];
    conf_upper = [conf_upper; transpose(betaci(:,2))];
    theta_est(voxel,:) = transpose(thetahat);
    res_after_est(voxel,:) = transpose(resid);
end for

conf_int= (conf_upper-conf_lower)/2;

% Test for normality in the residuals
for voxel = 1:k
    % Lilliefors test for goodness of fit to a normal distribution
    H = lillietest(res_after_est(voxel,:), 0.01);
    h_tab(voxel,1) = H;
    % Bera-Jarque test for normality in the residuals
    H = jbtest(res_after_est(voxel,:), 0.01);
    h_tab(voxel,2) = H;
end for
return;
```

6.4 Kruggel & Cramon Model

This section considers the details of implementation for the Kruggel & Cramon Model. The general model description is found in Section 5.2. This model differs from the previous model in the way it deals with noise. Temporal and/or spatial correlations in the residuals are applied as weights in a weighted least squares approach. One set of parameters is then estimated for each separate trial in a ROI time series.

The estimation procedure, in which one set of parameters is estimated for each trial (ROI), was implemented in a matlab m-file, `ihk_kruggel`. This function calls several other m-files for the calculation of the covariance structure and parametric modeling function. The parametric modeling function is the Gaussian function as described by Equation (6.1) and illustrated in Figure 6.5. Two approaches were investigated for the minimization of

$$D(\boldsymbol{\theta}) = (\mathbf{Y} - \mathbf{G}(\boldsymbol{\theta}))^T \mathbf{V}^{-1} (\mathbf{Y} - \mathbf{G}(\boldsymbol{\theta})) \tag{6.2}$$

1. Levenberg-Marquardt method, as implemented in the Matlab function `lsqnonlin` (see Appendix A.4), and

2. multi-dimensional unconstrained nonlinear minimization by Nelder-Mead Downhill Simplex Method as implemented in the Matlab function `fminsearch` (see Appendix A.4).

`lsqnonlin` does not take the covariance matrix, $\mathbf{V}^{-1}$, as input argument. An adjustment of the object function (Equation (6.2)) is therefore necessary. $\mathbf{V}^{-1}$ is both symmetric and positive definit[1]. Choleskys factorization can therefore be applied, producing an upper triangular matrix, $\mathbf{L}$, such that $\mathbf{V}^{-1} = \mathbf{L}^T\mathbf{L}$. Substitution yields

$$D(\boldsymbol{\theta}) = (\mathbf{L}(\mathbf{Y} - \mathbf{G}(\boldsymbol{\theta})))^T (\mathbf{L}(\mathbf{Y} - \mathbf{G}(\boldsymbol{\theta}))),$$

which is valid input for `lsqnonlin`.

Before employing the estimation methods, however, tests concerning their ability to reproduce the true parameters were performed. For this purpose, signals with known true parameters were constructed from the Gaussian modeling function. Both `lsqnonlin` and `fminsearch` achieve a good fit when starting values are relatively near the true parameters. By appropriately setting the tolerance, `lsqnonlin` succeeded in finding the true parameters even with extremely bad parameter starting values. `fminsearch` fails, however, to arrive at the true values if the initial parameter values are far from the true values. Fortunately,

[1]Positive definit: An n $n \times n$ matrix, M, is positive definit if for every n component vector, $x^T M x \geq 0$, furthermore $x^T M x = 0$ only if x is the zero vector. Equivalent definition: M has all positive eigenvalues.

the intervals for realistic starting values are not too difficult to find (e.g. the parameter *lag* should be given a starting value according to the expected time to maximum of the BOLD-response, usually between 2 and 6 seconds), and `fminsearch` performs acceptably within these limits. The use of `fminsearch` is therefore justified.

The procedure was implemented in Matlab and the core functions follow below. For simplicity, the code is shown only with `lsqnonlin` for the optimization of $D(\boldsymbol{\theta})$ in Equation (6.2). ROI's consisting of k voxels in l 2-dimensional grids are reorganized into matrices ROI(s,t) such that $s = 1, .., k$, and $t = 1, .., l$. In this work all ROI's are 3×3 voxel grids (i.e $k = 9$). The function `ihk_Kruggel` accepts a $k \times l$ matrix (ROI) as input. Choleskys factorization and calculation of the Kronecker product is performed by the Matlab routines `chol` and `kron`. The Matlab function `nlparci` is employed for the computation of 95% confidence intervals on the model parameters, $\boldsymbol{\theta}$, and normality in the residuals is explored using the Matlab functions `lillietest` and `jbtest`. For a brief outline of the employed Matlab functions see Appendix A.4. Code for the subroutines `ihk_argmin`, `ihk_gaussmodelHR` and `ihk_find_rhoxy` are not shown. `ihk_argmin` is used with `lsqnonlin` and returns a scalar value, res=$\mathbf{L} \times (\mathbf{Y} - \mathbf{G})$, `ihk_gaussmodelHR` returns a vector $\mathbf{g} = g_1, ..., g_l$ representing the Gaussian modeling function and `ihk_find_rhoxy` is used with `ihk_nlinfit` and returns a vector, result = $\rho_X^h \; \rho_Y^v$ for all combinations of h and v.

Matlab function `ihk_kruggel` :

INPUT :

- ROI (matrix with k rows (voxels) and l columns (time points in a single trial))
- t (vector with time points, if $t = [0 : 2 : 22]$ then the trial has 12 time points with 2 second interval between each time point)
- start (starting values for the model parameter vector (theta))
- N (number of desired iterations to compute the spatiotemporal correlation matrix (and optimize $D(\boldsymbol{\theta})$ in Equation (6.2)))
- tolx (termination tolerance on model parameter vector (theta))
- tolfun (termination tolerance on the function value)

OUTPUT:

- est_theta (vector of estimated model parameters)
- betaci (95% confidence interval for the model parameter vector, theta_est)
- h_tab (table of results from Lilliefors and Bera-Jarque tests for normality in the residuals)

$[k, l]$ = size(ROI); *% k voxels and l time points*

x = [1,1]; *% starting values for* ρ_X *and* ρ_Y
model = ihk_argmin; *% subroutine for use with lsqnonlin*
Y = reshape(transpose(ROI), 1, *k*l*);
theta = start;

for rep = 1 : N
% compute the gaussian modeling function with current values of theta
g = ink_gaussmodelHR(theta,t) ;

% find the residuals
for i = 1: *k*
residual(i,:) = ROI(i,:) - g ;
end for

% compute V_inv from the residuals
gamma2 = var(var(transpose(residual)));
rhoT = ihk_compute_rhoT(residual);
V_inv_time = ihk_setup_V_inv_time(rhoT,*l*);
V_inv = ihk_inverseV(residual, gamma2, V_inv_time, x);

L = chol(V_inv); *% Cholesky factorization V_inv = transpose(L)*L*
opt = optimset('LargeScale','off','MaxFunEvals', 1000,'TolX',tolx,'TolFun',tolfun);

```
    % model = ihk_argmin : subroutine for lsqnonlin, returns L*(Y - G)
   [theta, resnorm, res, exitflag, OUTPUT, lambda, jacobian] = ...
                    lsqnonlin(model, theta, [ ], [ ], opt, transpose(Y), L, t);
    if exitflag ~= 1
       print ERROR message
    end if
end for

betaci = nlparci(theta, res,jacobian) ;

% Test for normality in the residuals
for voxel = 1:k
    % Lilliefors test for goodness of fit to a normal distribution
    H = lillietest(residual(voxel,:), 0.01);
    h_tab(voxel,1) = H;
    % Bera-Jarque test for normality in the residuals
    H = jbtest(residual(voxel,:), 0.01);
    h_tab(voxel,2) = H;
end for
return;
```

Matlab function `ihk_compute_rhoT`: Computes the temporal autocorrelation coefficient.

INPUT :

- residual (residual difference between the true and modeled data points)

OUTPUT:

- rhoT (temporal autocorrelation coefficient)

```
[k, l] = size(residual);
numerator = 0 ;
denominator = 0;
for s = 1 : k
   for t = 1 : l
       numerator = numerator + residual(s, t)*residual(s, t − 1);
       denominator = denominator + residual(s, t)^2;
    end for
end for
rhoT = numerator/denominator;
return
```

Matlab function `ihk_setup_V_inv_time`: Sets up the inverse temporal correlation matrix.

INPUT:

- rhoT (temporal autocorrelation coefficient)
- timesteps (number of timesteps in a single trial)

OUTPUT:

- V_inv_time (the inverse temporal correlation matrix)

```
rhoT_squared = rhoT^2;
D(1) = 1;
D(timesteps) = 1;
D(2:timesteps-1) = 1 + rhoT_squared;
rho_neg = ones(timesteps - 1 ,1)*(-rhoT);
V_inv_t = diag(D) + diag(rho_neg,-1)+ diag(rho_neg,1);
const = ( 1 ./( 1- ( rhoT_squared)));
V_inv_time = const .* V_inv_t;
return
```

Matlab function `ihk_inverseV` : Sets up the inverse spatiotemporal correlation matrix.

INPUT :

- residual (residual difference between the true and modeled data points)
- gamma (variance of residual)
- V_inv_time (inverse of the temporal correlation matrix)
- x (starting parameter vector for rhoX and rhoY)

OUTPUT:

- V_inv (the inverse spatiotemporal correlation matrix)

```
[k, l]=(residual)
[rhohat,h,v] = ihk_rhohat_hv(residual);
q = length(rhohat);
hv = [transpose(h), transpose(v)];
model = 'ihk_find_rhoxy'; % subroutine for use with ihk_nlinfit
[X, resid, J] = ihk_nlinfit(hv, rhohat, model, x);

V_inv = [ ];
rhoX = X(1); rhoY = X(2);
Vs = zeros(k);
roi_rows = 3;
r = 0;
h_new = h ; v_new = v;
% set up the spatial correlation matrix V
for i = 1:q
    for j = (i+1):k
        Vs(i,j) = (rhoX.^(h_new(j-1))) * (rhoY.^(v_new(j-1))) ;
    end for
    if r < roi_rows-1
        r = r+1; v_new = abs(v-r);
    else
        r = 0;
        v_new = v; h_new = abs(h_new-1);
    end if
end for

Vs = Vs+transpose(Vs);
for h = 1:k
    Vs(h, h) = 1;
end for
V_inv_space = inv(Vs);

% Set up the inverse spatiotemporal covariance matrix
V_inv = (1 /(gamma2.^ 2)).* kron(V_inv_space,V_inv_time);
return
```

Matlab function `ihk_ rhohat_hv` : Collect subsets of all pairs of sites located with the same absolute distance and compute the spatial correlation coefficient rhohat for each subset.

INPUT :

- residual (residual difference between the true and modeled data points)

OUTPUT:

- rh (vector containing the rhohat estimates)
- h (horizontal distance between two voxels)
- v (vertical distance between two voxels)

```
numerator = 0 ; denominator = 0;
numRows = 3; numCols = 3;
rh = [ ]; h = [ ]; v = [ ];
for hor = 0:numCols-1
    for ver = 0:numRows-1
      if hor + ver > 0 % (0,0) is not a valid combination
          h = [h,hor]; v = [v,ver];
          rhohat = 0; numerator = 0; denominator = 0; % initializing
          for r1 = 1 : numRows
             for c1 = 1 : numCols
                % find the corresponding index in residual
                s1 = r1 + (c1-1) * numRows
                for r2 = 1 : numRows
                   for c2 = 1 : numCols
                      if abs(r1-r2) == ver & abs(c1-c2) == hor
                         s2 = r2 + (c2-1)*numRows
                         for t=1:l
                            numerator = numerator + residual(s1,t)* residual(s2,t);
                            denominator = denominator + residual(s1,t)^2;
                         end for
                      end if
                   end for
                end for
             end for
          end for
          rhohat = numerator/denominator;
          rh = [rh, rhohat];
      end if
   end for
end for
return
```

6.5 Convolved Compartment Model

The Convolved Compartment Model presented in this work is constructed on the basis of two articles [28, 27], in which an outline of the procedure is given. A detailed description of the model is found in Section 5.3. There is a radical difference between the modeling function, $g(t, \boldsymbol{\theta})$, in this method and the Gaussian modeling function employed in the signal description methods in Sections 5.1 and 5.2. The modeling function for the present method is constructed from a more involved physiological point of view and attempts to modulate transient neuronal and vascular events associated with the haemodynamic BOLD-response. A square-wave function for the neuronal stimulation is combined (i.e. convolved) with a vascular compartment model. An example signal with the corresponding eight parameters is shown in Figure 6.6. Only the parameters t_0 (interpreted as onset of neuronal activation) and t_1 (interpreted as duration of neuronal activation) can easily be confirmed by visual inspection.

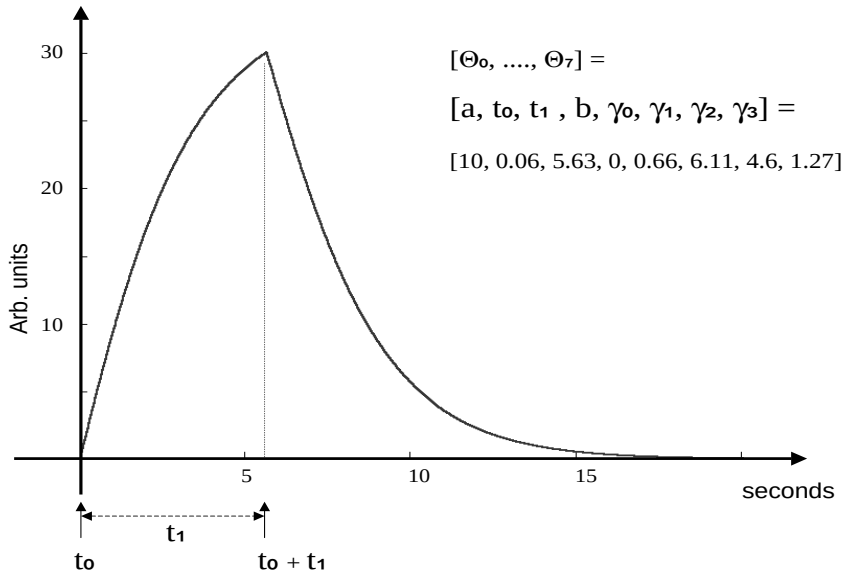

Figure 6.6: Modeling function, $g(t, \boldsymbol{\theta}) = f(t; \gamma_0, \gamma_1, \gamma_2, \gamma_3) \star n(t; a, t_0, t_1) + b$, for the Convolved Compartment Model. Note that $g(t, \boldsymbol{\theta}) = 0$ in the interval $0 \leq t < t_0$

For validation, the model was tested with various sets of known parameter vectors. The following steps were taken:

- Implementation of the physiological modeling function $g(t, \boldsymbol{\theta})$
- Signal construction based on the modeling function, the parameter vector used for this construction is denoted $\boldsymbol{\theta}_{true}$ and $\mathbf{g}_{true} = g(t, \boldsymbol{\theta}_{true})$
- Selection of 8 starting parameters, $\boldsymbol{\theta} = (\theta_0, \ldots, \theta_7)$
- Parameter estimation using the Levenberg-Marquardt procedure as implemented in Matlab's `lsqnonlin`. Estimated parameter vector is denoted $\boldsymbol{\theta}_{est}$ and $\mathbf{g}_{est} = g(t, \boldsymbol{\theta}_{est})$
- Comparison of results. Differences in $\mathbf{g}_{est}$ and $\mathbf{g}_{true}$ were found from:

$$\delta = \max_{t \in [a,b]} \{ |g_{true}(t) - g_{est}(t)| \} \tag{6.3}$$

  in which $[a, b]$ is the trial interval.

We define

$$\mathbf{g}_{true} \equiv \mathbf{g}_{est} \quad if \quad \delta \leq 10^{-3}.$$

With this definition, a high temporal resolution (e.g $t = 0 : 0.001 : 20$) and by appropriately setting the tolerance, $\mathbf{g}_{est}$ were found to be equal to $\mathbf{g}_{true}$. However, while differences between $\mathbf{g}_{est}$ and $\mathbf{g}_{true}$ were in the range of 10^{-3} or less, the corresponding parameter sets were found to differ in the order of for example 0.3-0.7 for γ_0 and 6.1-7.1 for γ_1. Hence, two signal that are equal according to our definition can be constructed from a number of relatively different parameter sets. It is, however, only in the vascular parameters, $(\gamma_0, .., \gamma_3)$, that the variabilities occur, the true neuronal parameters (a, t_0, t_1) are readily reproduced. Our tests suggest that the landscape of the multivariate function to minimize (Equation (5.24)) is rather shallow for the vascular parameters. This may lead to similar sub-optimal solutions (many local minima) in a relatively wide parameter range. Moreover, Kruggel & Cramon [28] "had to resort to a costly optimization method (the genetic algorithm)" in their optimisation step. An example of four signal shapes which are equal according to our definition, with corresponding vascular parameter sets, is illustrated in Figure 6.7.

Seeking the reasons for this behaviour in the vascular parameters, we explored the underlying physiological mechanisms of the vascular component (see Figure 6.8). Vascular geometry and distribution of oxyhaemoglobin/deoxyhaemoglobin is not easily modeled. An essential problem is that many image voxels contain very heterogeneous distributions

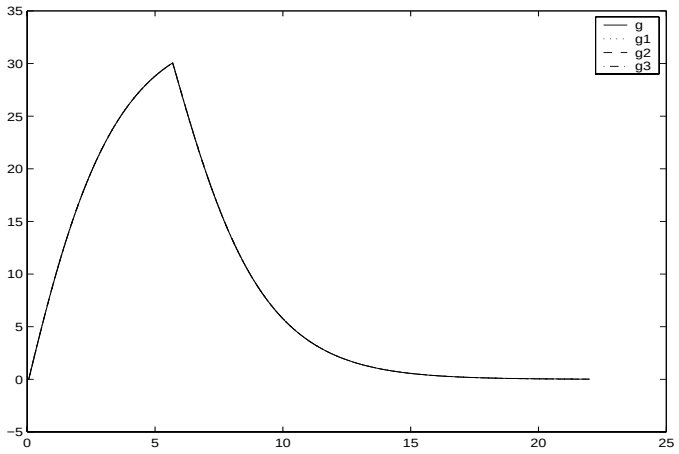

	0	1	2	3
γ_0	0.66	0.5059	0.5041	0.6998
γ_1	6.11	4.0276	3.6432	8.0046
γ_2	4.6	4.8139	4.8741	7.7228
γ_3	1.27	1.3231	1.2617	1.0434

Figure 6.7: Four modeling functions for the Convolved Compartment Model. Vascular parameter vectors for the four signal shapes, g,g_1,g_2 and g_4 are given in column 0,1,2 and 3, respectively.

of vessels [24]. A typical fMRI voxel is in the order of $3mm \times 3mm \times 4mm$, and such a voxel may contain blood vessels ranging from capillaries and venules up to larger draining veins. The contribution to the BOLD-response is not limited only to intravascular signals. The magnetic field gradient surrounding deoxyhaemoglobin extend into surrounding tissue, thereby affecting a larger proportion of water protons. The arterial side of the vasculature is essentially fully oxygenated, and hence, there are no contributions to the BOLD-response on this side. The BOLD response primarily arises from the capillary beds, venules and draining veins, which are only 60-70% saturated with oxygen at rest, and thus have the capacity of increasing the fraction of oxygen. Since the contribution from the arterial compartment in reality is either very small or nonexistent, the question arises whether signals from this compartment should be excluded from the model. Another important issue is the absence of signal contribution from a venous compartment.

The Convolved Compartment Model assumes the amount of oxyhaemoglobin (see Section 2.4.1) to be proportional to the response amplitude, with increasing amounts of oxyhaemoglobin leading to a stronger signal. The vascular transfer rates are a measure of the oxygen exchange between the different compartments. Increase in the oxyhaemoglobin concentration in a compartment should result in an increased signal contribution from that particular compartment. If the total amount of oxyhaemoglobin in the three compartments is reduced, the overall signal decreases. This is achieved by increasing the transfer rate, γ_3, at which oxyhaemoglobin leaves the capillary compartment. If γ_3 is given a fixed value, our tests show that the changes in the remaining transfer rates to some degree is capable of

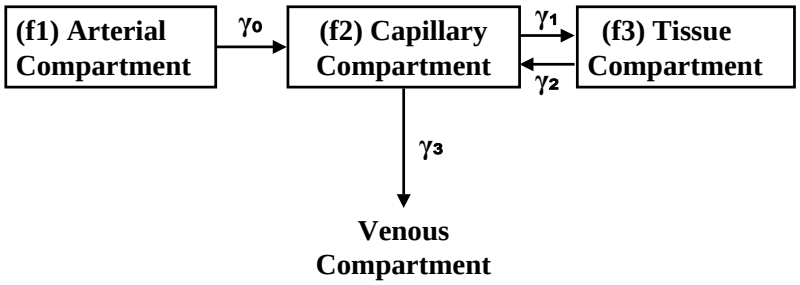

Figure 6.8: Movement of oxygen in vascular and tissue compartments. Modified from Kruggel & Cramon[1999]

cancelling out one another. More specifically, an increase in γ_0 and γ_2 leads to a higher concentration of oxyhaemoglobin in the capillary compartment (see Figure 6.8). These effects may, however, be counteracted by an increase in γ_1. Only two transfer rates, γ_1 and γ_2, directly affects the oxyhaemoglobin concentration of the tissue compartment. Decreasing γ_1 reduces the signal, but this effect may conveniently be cancelled out by a simultaneous decrease in γ_2. From a physiological point of view it is therefore reasonable that several combinations of the vascular parameters may lead to similar signal amplitudes. Another important issue regarding present fMRI techniques is the limited number of time steps that can be measured per trial. This puts restrictions on the maximum number of model parameters that can be reasonably estimated for any model function.

Tests were also performed separately on the vascular model, thereby eliminating possible influence by the neuronal parameters. The vascular component of the Convolved Compartment Model, $f = f_1 + f_2 + f_3$, is given by Equation (5.21) (illustrated in Figure 6.8). Estimation results from these tests did not contribute any significant improvement.

Signal contribution from the different compartments of the Convolved Compartment Model can also be regarded separately. Since the BOLD-response primarily arises from capillary, tissue and venules, the focus should be on the capillary compartment alone or on the capillary *and* the tissue compartments. This modeling context still suffer from the absence of venous contributions. To explore this approach, the convolution in Equation (5.18) was modified to only consider the capillary signal contribution, that is

$$y(s,t) = f_2(t) \star n(t) + b + \epsilon(s,t).$$

An example signal with the corresponding parameters is shown in Figure 6.9. Validation was performed as previously described. By appropriately setting the tolerance, and

applying a high temporal resolution, we found

$$\mathbf{g}_{est} \equiv \mathbf{g}_{true} \quad and \quad \boldsymbol{\theta}_{true} \equiv \boldsymbol{\theta}_{est}$$

However, the number of observations per trial in fMRI data is low compared to the temporal resolution employed for the present evaluations. Reducing the number of time points to 12-22 observations per trial lead to relatively large departures from the true (vascular) parameter values.

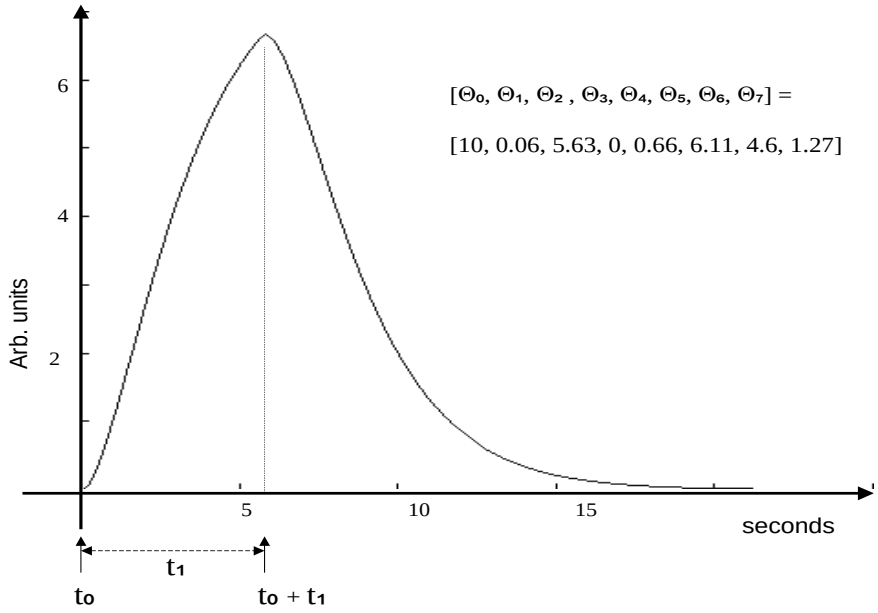

Figure 6.9: Modeling function for the capillary compartment of the Convolved Compartment Model

In the modeling of the BOLD-response it is important that the selected modeling functions span the space of potential responses. The shape of this modeling function differs from the shape of the Gaussian function, and may therefore be more suitable for modeling some types of BOLD-responses. The question arises, however, as to what extent conclusions regarding physiological characteristics, especially the vascular components, can be drawn.

Temporal and spatial correlations in the noise are estimated in the same way as for the Kruggel & Cramon Model. The noise correlation matrix, $\mathbf{V}^{-1}$, is then subject to a Choleskys factorization as described in the previous section. One parameter set is obtained for each trial in each ROI time series. Expensive estimation algorithms, such as genetic algorithms and simulated annealing, has been suggested for the minimization problem [28].

In this work a less costly optimization algorithm, the Levenberg-Marquardt method as implemented in the Matlab function `lsqnonlin` (see Appendix A.4), is used. The Convolved Compartment Model deals with noise in the same way as the Kruggel & Cramon Model(Sections 5.2 and 6.4). The implementation of the latter model could therefore be modified to accommodate the Convolved Compartment Model. The code for this procedure will not be repeated here. The difference between the two models lies in the choice of modeling function,$g(t, \boldsymbol{\theta})$. The physiologically based modeling function of the Convolved Compartment Model is computed from the following steps:

$$\lambda_0 = -0.5(\gamma_1 + \gamma_2 + \gamma_3 + \sqrt{(\gamma_1 + \gamma_2 + \gamma_3)^2 - 4\gamma_2\gamma_3})$$
$$\lambda_1 = -0.5(\gamma_1 + \gamma_2 + \gamma_3 - \sqrt{(\gamma_1 + \gamma_2 + \gamma_3)^2 - 4\gamma_2\gamma_3})$$

$$k_{1,1} = 1;\ k_{1,2} = 0;\ k_{1,3} = 0;$$
$$k_{2,1} = \frac{\gamma_0(\gamma_2-\gamma_0)}{(\gamma_0+\lambda_0)(\gamma_0+\lambda_1)},\ k_{2,2} = \frac{\gamma_0(\gamma_2+\lambda_0)}{(\gamma_0+\lambda_0)(\lambda_0-\lambda_1)},\ k_{2,3} = \frac{\gamma_0(\gamma_2+\lambda_1)}{(\gamma_0+\lambda_1)(\lambda_1-\lambda_0)}$$
$$k_{3,1} = \frac{\gamma_0\gamma_1}{(\gamma_0+\lambda_0)(\gamma_0+\lambda_1)},\ k_{3,2} = \frac{\gamma_0\gamma_1}{(\gamma_0+\lambda_0)(\lambda_0-\lambda_1)},\ k_{3,3} = \frac{\gamma_0\gamma_1}{(\gamma_0+\lambda_1)(\lambda_1-\lambda_0)}$$

$$kg1 = (k_{1,1} + k_{2,1} + k_{3,1})/\gamma_0$$
$$kg2 = (k_{1,2} + k_{2,2} + k_{3,2})/\lambda_0$$
$$kg3 = (k_{1,3} + k_{2,3} + k_{3,3})/\lambda_1$$

$$0 \le T < t_0$$
$$g_1 = 0,\ g_2 = 0,\ g_3 = 0$$

$$t_0 \le T < t_0 + t_1$$
$$g_1 = [g_1,\ kg1\ \left(e^{-\gamma_0(T-t_0)} - 1\right)]$$
$$g_2 = [g_2,\ kg2\ \left(e^{\lambda_0(T-t_0)} - 1\right)]$$
$$g_3 = [g_3,\ kg3\ \left(e^{\lambda_1(T-t_0)} - 1\right)]$$

$$T \ge t_0 + t_1$$
$$g_1 = [g1,\ kg1\ \left(e^{-\gamma_0(T-t_0)} - e^{(-\gamma_0(T-t0-t1)}\right)]$$
$$g_2 = [g2,\ kg2\ \left[e^{\lambda_0(T-t_0)} - e^{(\lambda_0(T-t0-t1)}\right)]$$
$$g_3 = [g3,\ kg3\ \left[e^{\lambda_1(T-t_0)} - e^{(\lambda_1(T-t0-t1)}\right]$$

$$g = -g_1 + g_2 + g_3$$
$$g = g \times a + b$$

Chapter 7

Experimental Results

This chapter reports of experiments on synthetic as well as real data. The *signal detection* problem is assessed by ANOVA (Section 4.1) on a real er-fMRI data set. The main part of this chapter is, however, dedicated to the *signal description* problem which can for example be formulated in terms of introduction and estimation of physiologically interpretable parameters like *lag* (time to maximum response intensity), *dispersion* (duration of response) and *gain* response intensity/strength) or vascular transfer rates between different physiological tissue compartments. The methods selected for this purpose are the Nonlinear Least Squares Model (Section 5.1), the Kruggel & Cramon Model (Section 5.2) and the Convolved Compartment Model (Section 5.3). The ability to model the BOLD-response in er-fMRI data, with increasing noise levels, have been explored. Another issue of interest is whether the parameters are capable of reflecting physiological characteristics of the BOLD-response itself and/or the underlying neuronal activity.

Section 7.1 deals with experiments on synthetic data. These experiments are concerned exclusively with the signal *description* problem. In Section 7.2 real data experiments dealing with both the signal *detection* problem and the signal *description* problem will be presented. Experiments on real data with the Convolved Compartment Model have not carried out.

7.1 Synthetic Data

7.1.1 Construction of Synthetic Data

Simulated event-related data-sets have been used for the evaluation of the signal *description* models in this thesis. A dataset from a recent single trial er-fMRI experiment on language processing was selected for this purpose. This dataset was acquired on a Siemens Vision

Plus 1.5 Tesla Scanner at Haukeland University Hospital. We used gradient echo, with an echo time TE = 60 msec, TR = 0.6 sec and flip angle = 90° (FOV = 200mm), and a total of 501 echo planar images (EPI see Section 2.2.7) were acquired. Each image consisted of 20 slices of 64 ×64 voxel resolution and spatial resolution 3.13×3.13×4 mm, no gap between consecutive slices. A corresponding anatomical image was acquired in the same session.

The data set was preprocessed and analyzed with SPM99 (see Appendix A.3) after which 25 non-activated brain patches were located. Synthetic ROI time series were constructed by modulating various prototypical BOLD-responses with known properties (spatial distribution, temporal shape; Figures 7.4 and 7.5) onto these patches. Five different prototypical BOLD-responses with sampling frequency of 12 time points per single trial and 2 seconds between each time point, were explored. With this trial period of 12 time points, a total of 40 prototypical BOLD-responses were modulated onto each voxel time series.

In real fMRI data sets, the BOLD-response have been reported to be in the order of about 1-10% relative to mean signal intensity level. Boynton et al. [5] found that activation modulates 5-10% above and below baseline whereas Parrish et al. [36] estimates brain activations to be 1-5% relative to mean signal intensity level (at 1.5 Tesla). The synthetic data should be tested with similar Signal to Noise Ratio (SNR, see Section 2.2.8).

We found a high spatial correlation in the fMRI voxel time courses used for the synthetic data set. For the spatial pattern illustrated in Figure 7.4, correlation coefficients in the x and y-directions (see Section 5.2) were calculated to be in the range 0.95-1.0 for preprocessed and smoothed data, and 0.6-1.0 prior to preprocessing. Since Kruggel & Cramon [27] reported of spatial correlation coefficients in the range of 0.4-0.6 for smoothed data, and 0.1-0.3 for non-filtered data, two additional data sets from two different experiments, acquired at Haukeland University Hospital, were also investigated. Correlation coefficients for both data sets confirmed a high spatial correlation. Figures 7.1, 7.2 and 7.3 illustrates the spatial correlations in the three data sets.
The noisy component of fMRI data is assumed to have a normal distribution (see Section 3.2). Normality tests according to Lilliefors and Bera-Jarque confirmed this assumption for all three data sets.

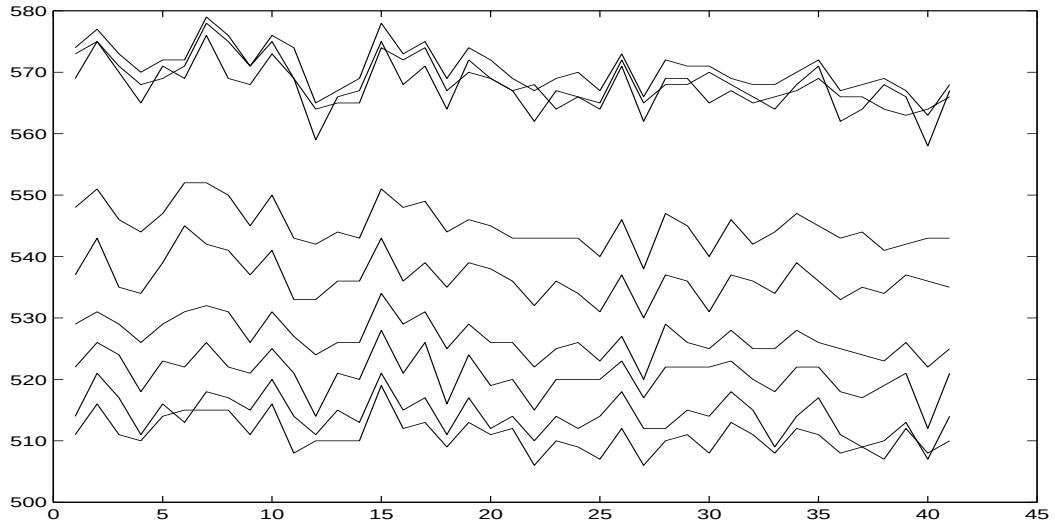

Figure 7.1: Signal intensity versus time (i.e voxel time courses) in smoothed fMRI data for 9 neighbouring voxels in a *word* recognition single trial er-fMRI experiment. x-axis represents time (seconds) and y-axis the signal intensity (arbitrary units). Note the spatial correlation of the time series.

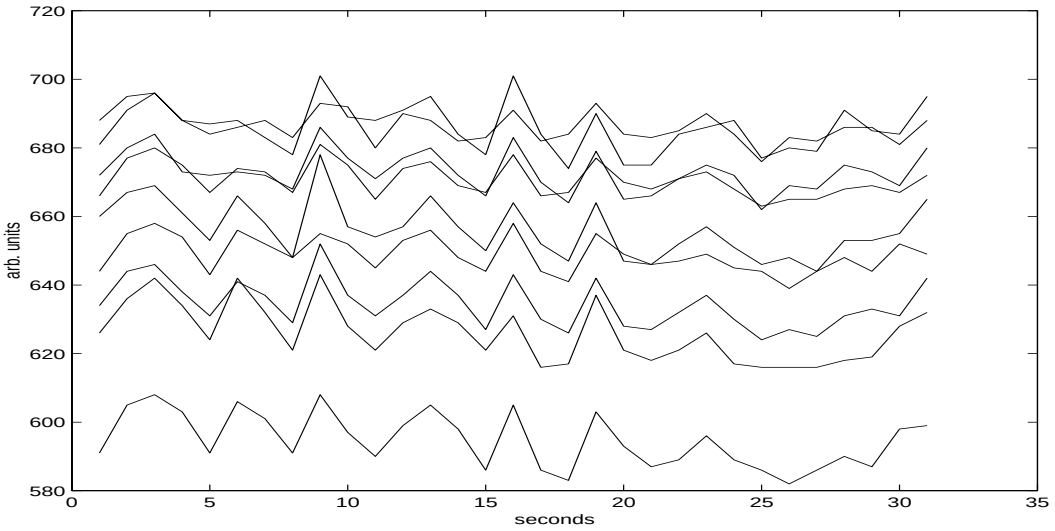

Figure 7.2: Signal intensity versus time (i.e voxel time courses) in smoothed fMRI data for 9 neighbouring voxels in a finger tapping er-fMRI experiment. x-axis represents time (seconds) and y-axis the signal intensity (arbitrary units). Note the spatial correlation of the time series.

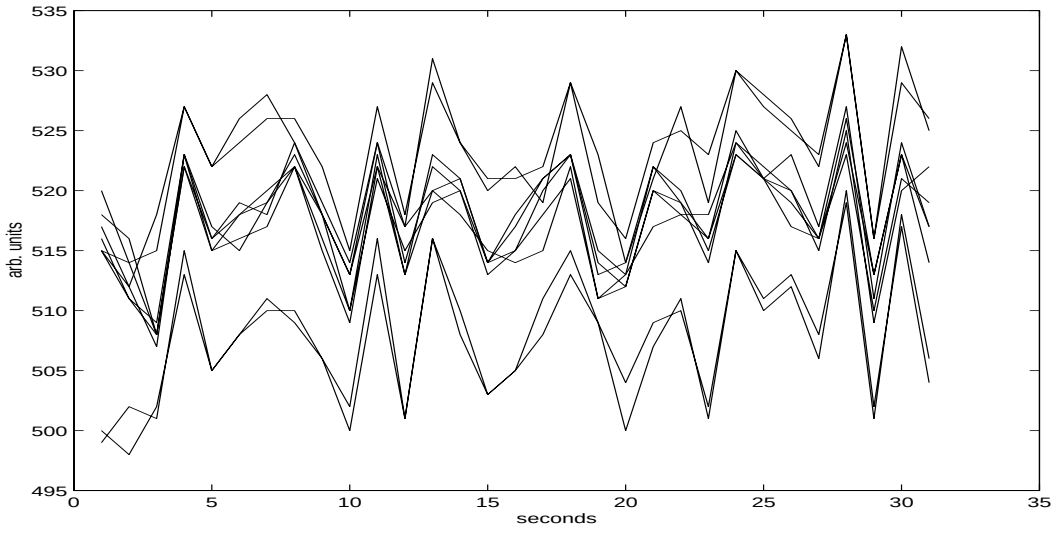

Figure 7.3: Signal intensity versus time (i.e voxel time courses) in smoothed fMRI data for 9 neighbouring voxels in a dichotic listening, er-fMRI experiment. x-axis represents time (seconds) and y-axis the signal intensity (arbitrary units). Note the spatial correlation of the time series.

7.1.2 Experimental Design

The BOLD-response is reported to vary in duration, time to maximum as well as rise and fall times. For the experiments in this thesis five different prototypical BOLD-responses, with varying spatial and temporal characteristics, were constructed. Figure 7.4 depict three of these shapes and their spatial pattern. These three shapes were constructed from the Gaussian function (see Equation (3.6)), and were employed in the experiments involving the Nonlinear Least Squares Model in Section 7.1.3 and the Kruggel & Cramon Model in Section 7.1.4. True parameters for *dispersion* and *lag* are given in Table 7.1.2. Baseline correction influence the values of *gain* and *baseline*. True values for these parameters must therefore be established separately for each voxel time course. The three different Gaussian shapes were modulated onto each of the 25 non-activated brain patches yielding a total of 75 ROI time series.

For the experiments in Section 7.1.5 with the Convolved Compartment Model, two different prototypical BOLD-responses (see Figure 7.5) were constructed from Equation (5.18) with spatial pattern as illustrated in Figure 7.4a. From these two shapes a total of 50 synthetic ROI time series were constructed.

The prototypical BOLD-responses were modulated onto the 25 brain patches with signal

amplitudes ranging from 2-6% relative to mean signal intensity level. Each prototypical BOLD-response was represented with a discrete equidistant sampling of 12 time points per single trial. This temporal resolution is a compromise between the advantage of performing estimation on as many data points as possible per time unit and the temporal resolution of the available fMRI-technique (multi-slice gradient echo EPI).

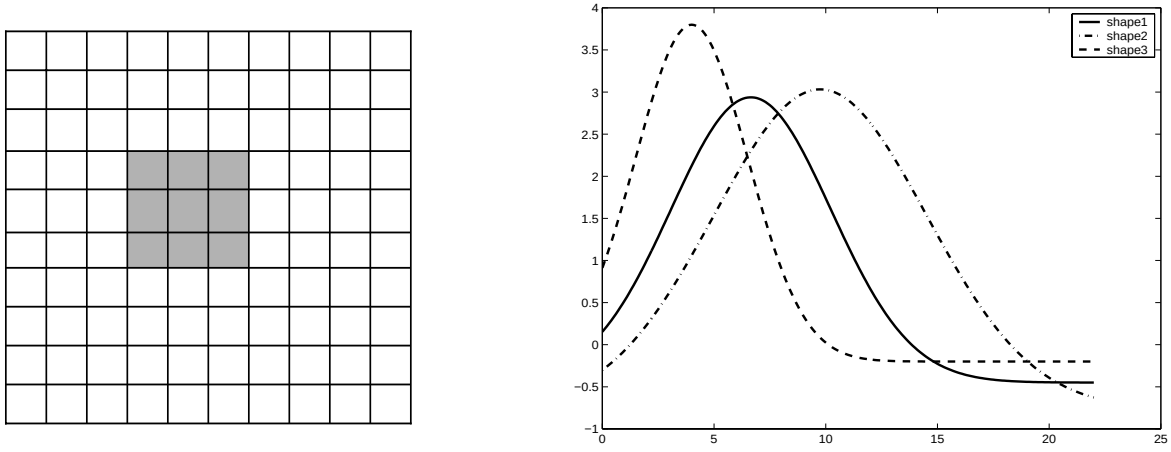

a b

Figure 7.4: (**a**) Spatial pattern of the BOLD-response used in the simulated data. (**b**) Three different shapes for the prototypical BOLD-response, constructed from the Gaussian function.

	Dispersion (θ_1)	Lag (θ_2)
Shape 1	3.5798	6.6502
Shape 2	4.7553	9.7541
Shape 3	2.5	4.0

Table 7.1: True values for the parameters *dispersion* and *lag* for the three prototypical BOLD-responses in Figure 7.4.

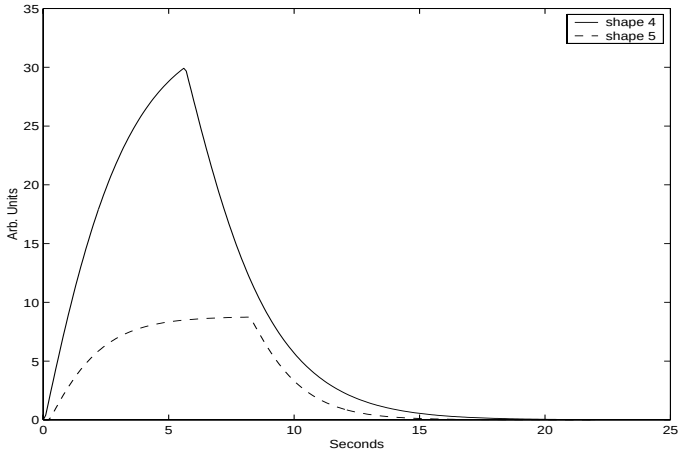

	4	5
θ_0	7	4
θ_1	0.05	0.25
θ_2	4.6	8
θ_3	0	0
θ_4	0.4	0.7
θ_5	8.51	6.11
θ_6	8.6	6.6
θ_7	3.17	2.5

Figure 7.5: Two different synthetic BOLD-responses constructed from the modeling function in the Convolved Compartment Model. True values for the parameter vector, $\boldsymbol{\theta}$, are given in 4 and 5.

The prototypical BOLD-responses were adjusted to both signal amplitude and mean signal intensity level. Matlab code for this procedure is shown below (`ihk_synt_data`). A subroutine (`ihk_update_y`) takes care of the estimation of the true parameters after the prototypical BOLD-response has been adjusted to mean signal intensity level and desired signal amplitude. Estimation procedure for finding the true parameters depends on whether the prototypical BOLD-response was constructed from the Gaussian function or from the modeling function of the Convolved Compartment Model. The subroutine takes as input the estimation procedure and the prototypical BOLD-response, and returns a new prototypical BOLD-response which can be modulated onto the non-activated brain patch. Figure 7.6 shows a synthesized signal collected from 4 neighboring voxels.

Matlab function `ihk_synt_data` :

INPUT:

- y (vector with prototypical BOLD-response)
- ROI (non-activated brain patch, 3×3 voxel grid)
- signampl (desired signal amplitude)
- est_model (optimization method for finding the true parameters. Options are "gauss" or "convcomp")

OUTPUT:

- ROI_new (the new ROI with synthetic activation/BOLD-response)
- theta_true (true parameters for the prototypical BOLD-response)

$[k, N]$ = size(ROI); *% k voxels and N time points*
l = length(y); *% l time points per trial*
residual = ROI;

% find mean_voxel_value as the mean over all time steps for each voxel in a ROI
mean_voxel_value = mean(transpose(ROI));

% compute scaling factor for the prototypical BOLD-response relative to mean signal intensity level
rise_voxels = mean_voxel_value.* signampl;
scale_voxels = rise_voxels ./ max(y);

% adjust y
scale_average = mean(scale_voxels);
y_new = scale_average .* y;

% update y_new and find true parameters
t=[0 : 2 : l]; *% 2 seconds between each time point*
[theta_true, y_update] = ihk_update_y(y_new,' est_model',t);

% modulate the signal on top of the noise
for voxel = 1 : k
  for trial = 1 : l : N
    if (trial+(l − 1)) ≤ N
      ROI(voxel,trial:(trial+(l−1))) = (ROI(voxel,trial:(trial+(l−1)))+ transpose(y_update));
    end if
  end for
end for

% correct for baseline
meanresidual = mean(transpose(residual));
for i = 1:k
  ROI(i,:) = (ROI(i,:) - meanresidual(i));
end for
return;

Matlab function `ihk_update_y` :

INPUT:

- y (vector with prototypical BOLD-response)
- est_model (optimization method)

- t (vector of time points)

OUTPUT:

- theta_true (true parameters for y)
- y_update (updated y constructed from theta_true)

opt = optimset('TolX',1e-5,'TolFun',1e-8);
if 'est_model' == gauss
    model = 'ihk_argmin'; *% Subroutine for use with lsqnonlin*
    start = [1, 1, 1, 1];
   [theta_true, resnorm, res, ef] = lsqnonlin(model,start,[],[],opt,y_new,t);
    if ef ~= 1
        print ERROR message
    end if
    y_update = ihk_gaussmodelHR(theta_true,t); *% Subroutine for computing the Gaussian function*
else if 'est_model' == convcomp
    model = 'ihk_argmin_cc; *% Subroutine for use with lsqnonlin*
    start = [5, 0.06, 6, 0.1, 1, 7, 7, 2];
    [theta_true, resnorm, res, ef] = lsqnonlin(model,start,[],[],opt,y_new,t);
    if ef ~= 1
        print ERROR message
    end if
    % `ihk_cc_g`*: Subroutine for computing the modeling function for the Convolved Compartment Model*
    y_update = ihk_cc_g(theta_true,t);
else print ERROR message
end if
return;

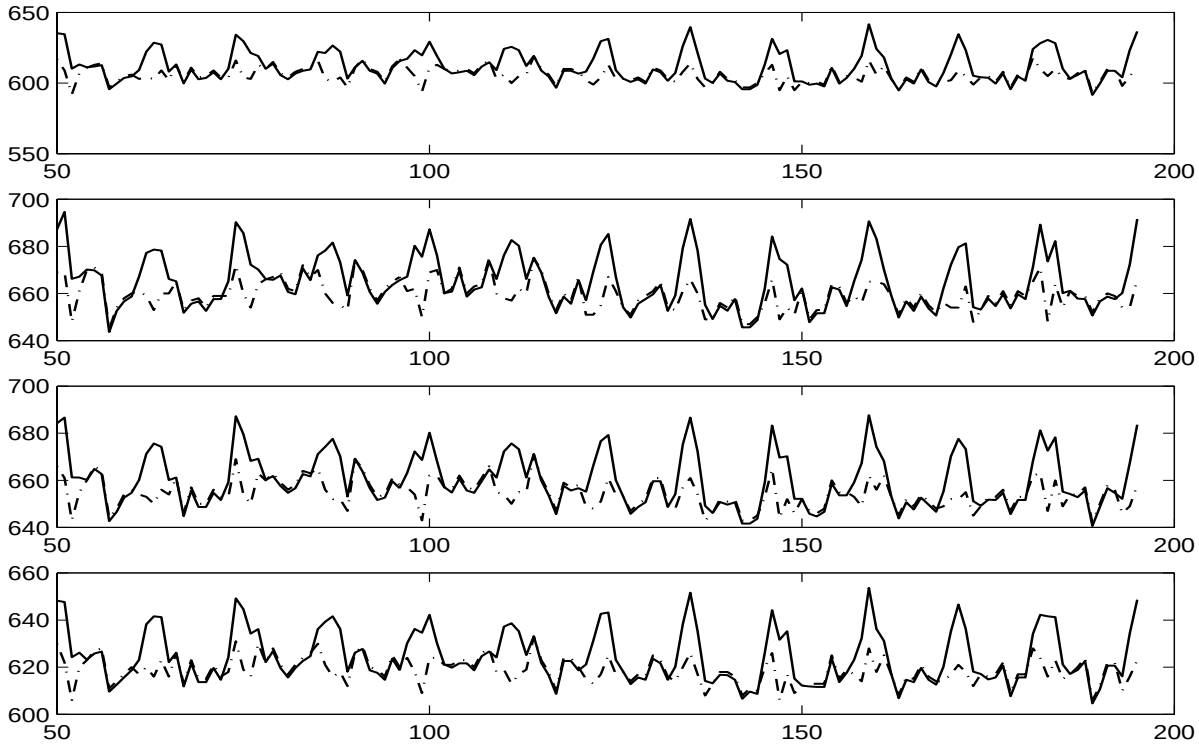

Figure 7.6: Plot of synthesized signal (solid line) superimposed on background noise (dashed line) from four neighbouring voxels. x-axis denotes the scan number and the y-axis is the signal intensity (arbitrary units). Signal amplitude is 4%.

A major advantage with synthetic data is knowledge of the true parameters - and ideally the modeling function should span the space of all possible BOLD-responses. Such a modeling function is, however, not presently available, and we must therefore resort to modeling functions that approximate the observed fMRI signal. None of the five prototypes have the pre- or postundershoot features described in Section 3.1 (and illustrated in Figure 3.1). Neither the Gaussian modeling function (Equation (3.6)) nor the modeling function for the Convolved Compartment Model (Equation (5.18)) are able to modulate these characteristics. Thus, if the prototypes were to have these features, true parameters could not have been established. However, the so called initial dip and post-undershoot is not regularly observed at magnetic field strength of 1.5 Tesla.

The estimation of the parameters can be simplified by assuming that identical trials lead to similar responses in a specific region of interest. In the case of synthesized data this assumption is already present in the data because only one response type is modulated onto the background noise in each voxel time-series. Averaging over all trials in a voxel

will reduce the noise and approximate the true signal (See Section 4.1). The Nonlinear Least Squares Model in experiment I explores these issues. Experiment II and III covers the Kruggel & Cramon Model and the Convolved Compartment Model, respectively.

7.1.3 Experiment I: Nonlinear Least Squares Model

In the Nonlinear Least Squares Model noise is reduced by averaging over multiple trials (see Figure 7.7). Given the 75 synthetic ROI's (25 ROI time series for each of the three prototypical BOLD-responses (see Section 7.1.2)), time-locked to stimulus averaging over all 40 trials in each voxel in all ROI time series was performed. Parameter estimates were obtained using the Gauss-Newton Method as implemented in `nlinfit`. Signal amplitudes ranged from 2-6% relative to mean signal intensity level. For all voxel time series a set of parameter estimates, accompanied by 95% confidence intervals (according to the method in Matlab's `nlparci`) was obtained for each of the five amplitude settings. Visual inspection of synthesized and modeled signals were carried out for all shapes in all voxels and for all signal amplitudes. A good fit was generally found for signal amplitudes ranging from 4-5%. For signal amplitudes of 2-3% the synthesized signal was in some voxels distorted by noise, and thereby not easily modeled with the Gaussian modeling function. All the true parameter values, $(\theta_0, \theta_1, \theta_2, \theta_3)$, were, however, found to be within the 95% confidence intervals of the estimated values (cfr Table 7.1.3). Figures 7.8, 7.9, 7.10 and 7.11 illustrates the averaged prototypical BOLD-responses together with the modeled signal for a representative ROI time series. Signal amplitudes were 4% for the first three examples and 2% for the last example. Summary of results for prototypical BOLD-response, shape 3 in six representative ROI's are presented in Table 7.1.3. The table shows the average (parameter vector and 95% confidence intervals) over the nine estimates obtained for each ROI time series.

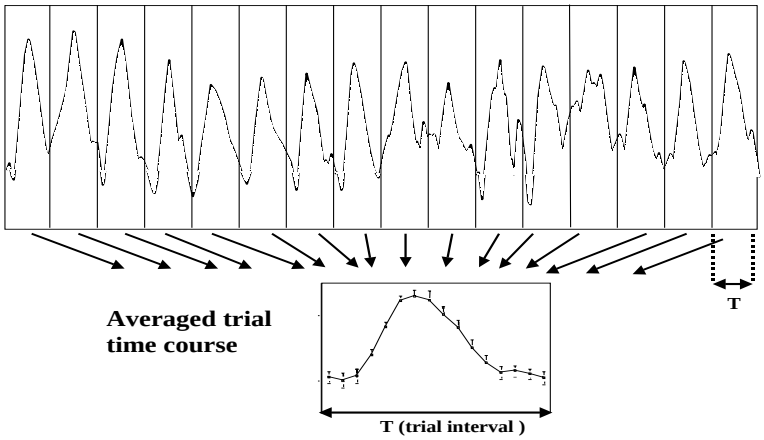

Figure 7.7: Averaged responses in er-fMRI. Averaging is performed over all trials of the same type. The magnitude of the noisy component is reduced, but not that of the repeated signal (Modified from R. Buckner, HBM 2000).

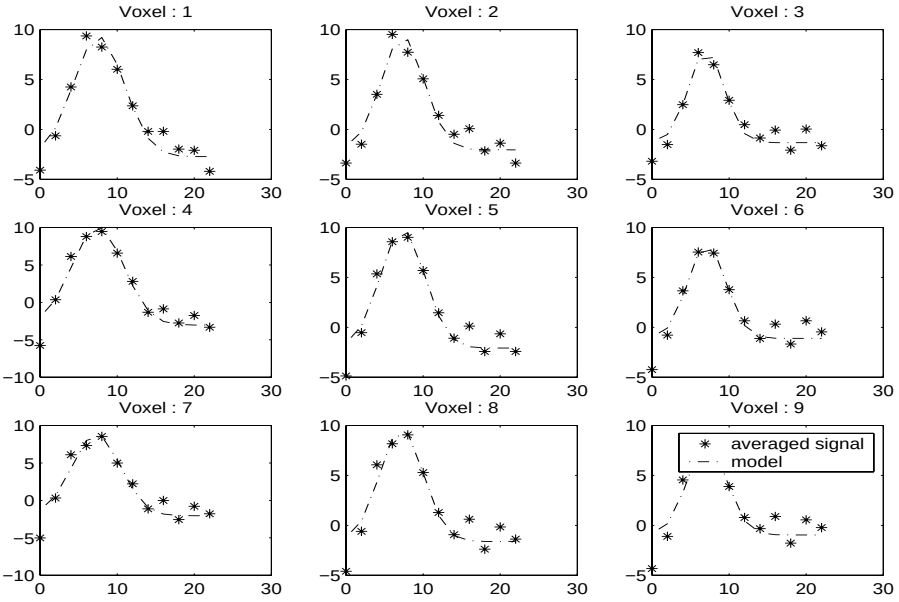

Figure 7.8: Synthetic data, Experiment I, results from estimation of parameters for the synthetic shape 1 (cfr. Figure 7.4). Time-locked to stimulus averaging of synthetic time course over all trials is denoted by star dots. The estimated model signal time course is denoted by solid line. Signal amplitude is 4%.

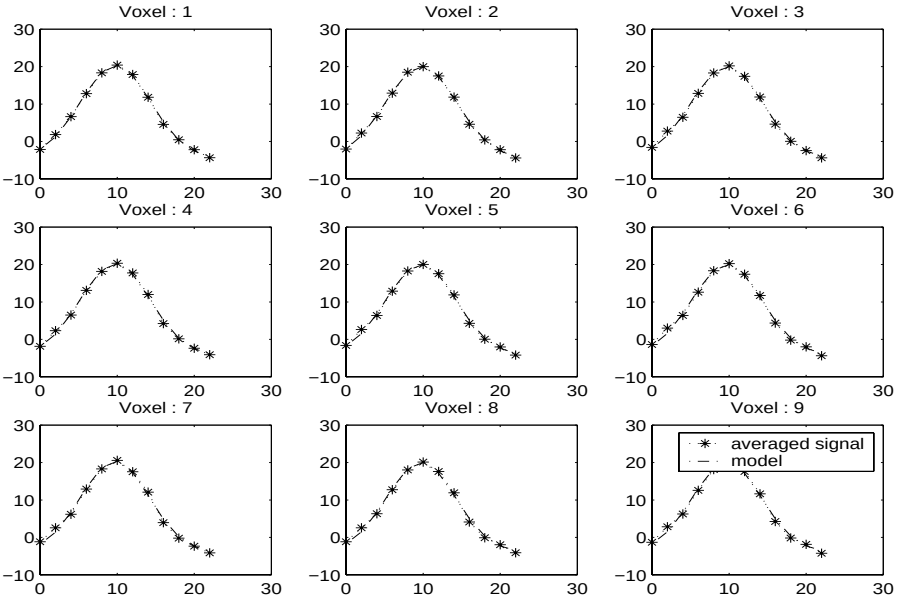

Figure 7.9: Synthetic data, Experiment I, results from estimation of parameters for the prototypical BOLD-response, shape 2 (cfr. Figure 7.4). Time-locked to stimulus averaging of synthetic time course over all trials is denoted by star dots. The estimated model signal time course is denoted by solid line. Signal amplitude is 4%.

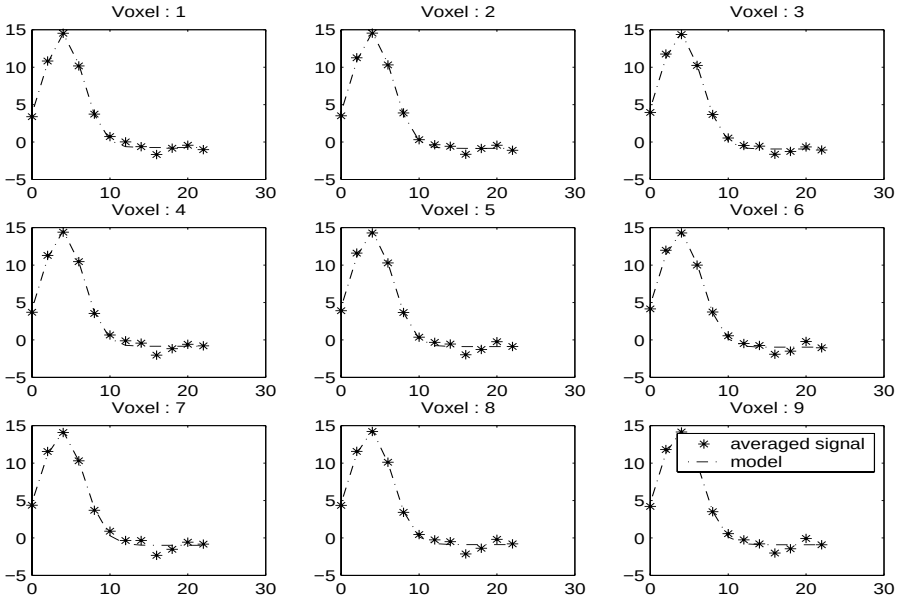

Figure 7.10: Synthetic data, Experiment I, results from estimation of parameters for the prototypical BOLD-response, shape 3 (cfr. Figure 7.4). Time-locked to stimulus averaging of synthetic time course over all trials is denoted by star dots. The estimated model signal time course is denoted by solid line. Signal amplitude is 4%.

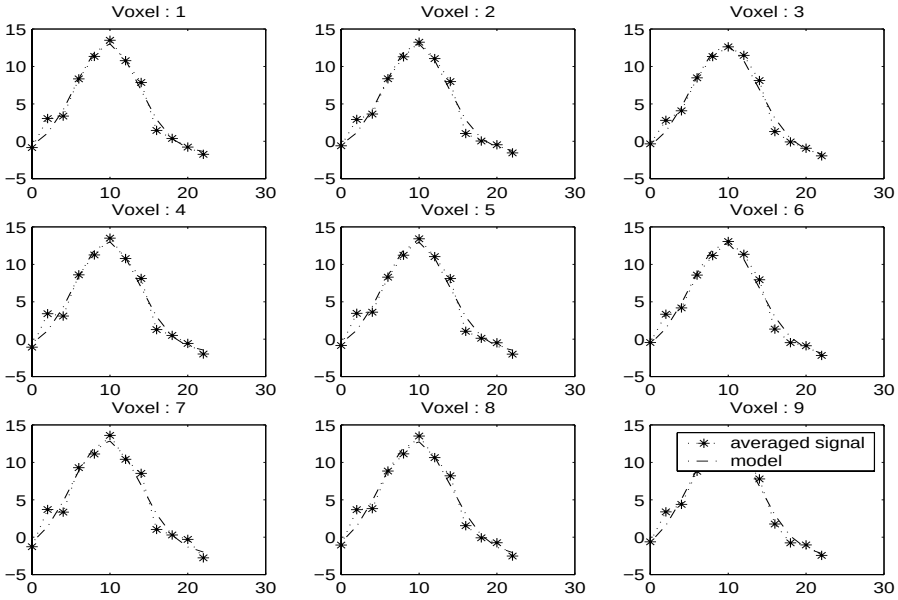

Figure 7.11: Synthetic data, Experiment I, results from estimation of parameters for the prototypical BOLD-response, shape 2 (cfr. Figure 7.4). Time-locked to stimulus averaging of synthetic time course over all trials is denoted by star dots. The estimated model signal time course is denoted by solid line. Signal amplitude is 2%.

Location		θ_0 (gain)	θ_1 (dispersion)	θ_2 (lag)	θ_3 (baseline)
ROI 1	True	56.4506	2.5000	4.0000	-1.1290
	Estimated	59.4764 ∓5.46551	2.5911 ∓ 0.2279	3.8428 ∓ 0.1956	-1.3617 ∓ 0.7320
ROI 2	True	53.7129	2.5000	4.0000	-1.0743
	Estimated	56.2737 ∓4.7608	2.5643 ∓0.2077	3.8630 ∓ 0.1790	-1.2725 ∓ 0.64350
ROI 3	True	58.9247	2.5000	4.0000	-1.1785
	Estimated	61.3766 ∓5.5697	2.5914 ∓0.2249	3.8909 ∓ 0.1934	-1.3221 ∓ 0.7488
ROI 4	True	70.2582	2.5000	4.0000	-1.4052
	Estimated	74.0736 ∓ 9.2802	2.6510 ∓0.3144	4.0306 ∓ 0.2693	-1.6675 ∓ 1.2337
ROI 5	True	59.4794	2.5000	4.0000	-1.1896
	Estimated	63.2248 ∓5.7620	2.5828 ∓ 0.2237	3.9949 ∓ 0.1928	-1.4817 ∓ 0.7781
ROI 6	True	62.6489	2.5000	4.0000	-1.2530
	Estimated	66.9899 ∓ 6.5016	2.6661 ∓ 0.2432	3.9187 ∓ 0.2082	-1.2530 ∓ 0.8639

Table 7.2: Synthetic data, Experiment I, averaged parameter estimates for the synthesized signal(prototypical BOLD-response, shape 3) in selected regions. Parameters and 95% confidence intervals averaged over each ROI.

Gain was found to increase linearly with signal amplitude. There was a tendency towards overestimated *gain* values for prototypical BOLD-response, shapes 1 and 3, whereas *gain* for shape 2 generally was estimated to be below the true value. *Dispersion* values were overestimated for shape 1 and 3, while a slight underestimation was seen for shape 2 (see Figure 7.12 a,b and c). These asymmetries increased for cases of low signal to noise ratio (SNR, see Section 2.2.8). *Lag* was slightly underestimated for all three shapes (see Figure 7.12 d,e and f).

The parameter estimates were plotted with signal amplitudes ranging from 2% to 5% relative to mean signal intensity level. For increasing SNR, the estimated parameters converge toward the true value. Figure 7.13 shows the resulting *dispersion* and *lag* values for a representative ROI time series.
Based on the test results the estimation procedure is assumed to be stable against noise levels typically found in er-fMRI data.

Normality (tested according to Lilliefors and Bera-Jarque (see Appendix A.4)) in the residual distributions after estimation were fulfilled for all regions. Q-Q plots also revealed a high conformance with a normal distribution.

Regarding physiological interpretations of the estimated parameters *gain*, *dispersion* and *lag* (which might express neuronal processing strength, processing duration or asynchrony and processing delay, respectively) we plotted the three parameter estimates in a 3D feature plot. This plot will thus indicate if the joint distribution of these parameters are sufficiently separated to discriminate between different types of BOLD-responses which might give information about underlying neuronal processing mechanisms. Feature plots were generated for all ROI time series and all signal amplitudes. Even for small signal amplitudes, the three different shapes explored in this experiment can easily be distinguished and if desired mapped to the corresponding anatomical images. Example feature plots for the three different shapes are given in Figures 7.14 and 7.15. Signal amplitudes are 2 and 5%. In both examples the three prototypical BOLD-responses are easily distinguished.

The performed experiments demonstrates that the averaging approach for the present model leads to robust parameter estimates for the three prototypical BOLD-responses. The model is stable against noise levels commonly found in fMRI data. Furthermore, the procedure is easy to implement and computation cost is low.

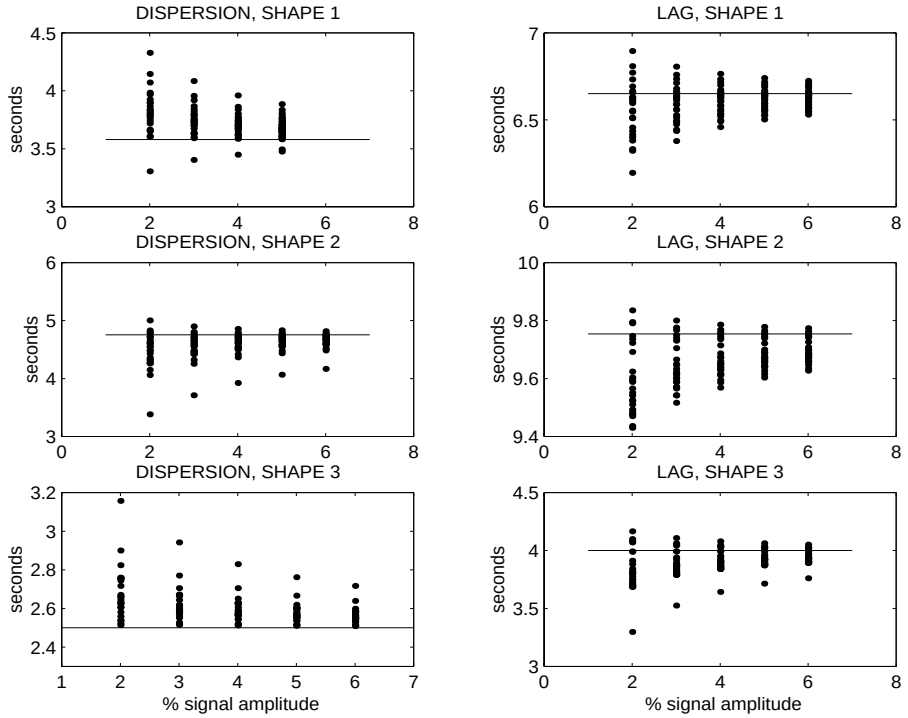

Figure 7.12: Synthetic data, Experiment I, Dependency of the parameters on the signal amplitude, here represented by *dispersion* (a,b,c) and *lag* (d,e,f) values. Signal amplitudes ranges from 2 to 6% relative to the mean intensity level.

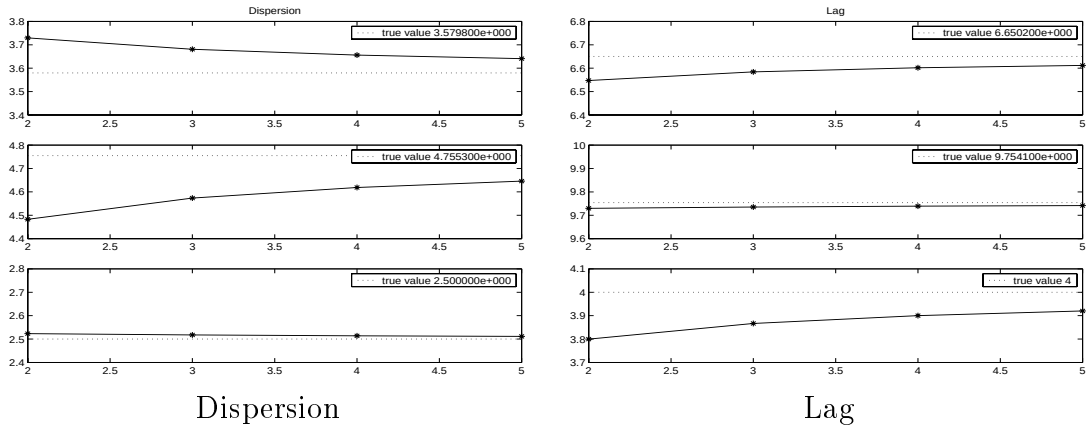

Figure 7.13: Synthetic data, Experiment I, robustness to noise in the parameters *dispersion* and *lag*. Signal amplitudes ranging from 2% to 5% relative to mean signal intensity.

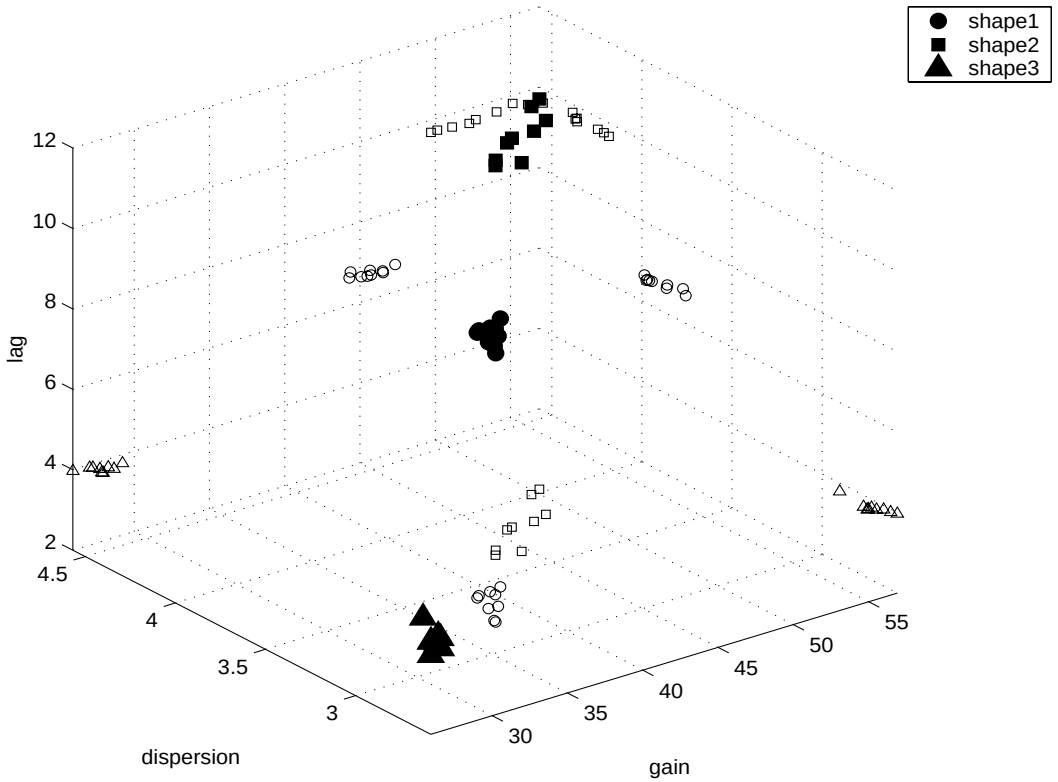

Figure 7.14: Synthetic data, Experiment I, example feature plot. Each prototypical BOLD-response is mapped in 3D feature space with a filled symbol. "Empty" symbols shows the projections from 3D feature space to each of the three planes. Signal amplitude is only 2%

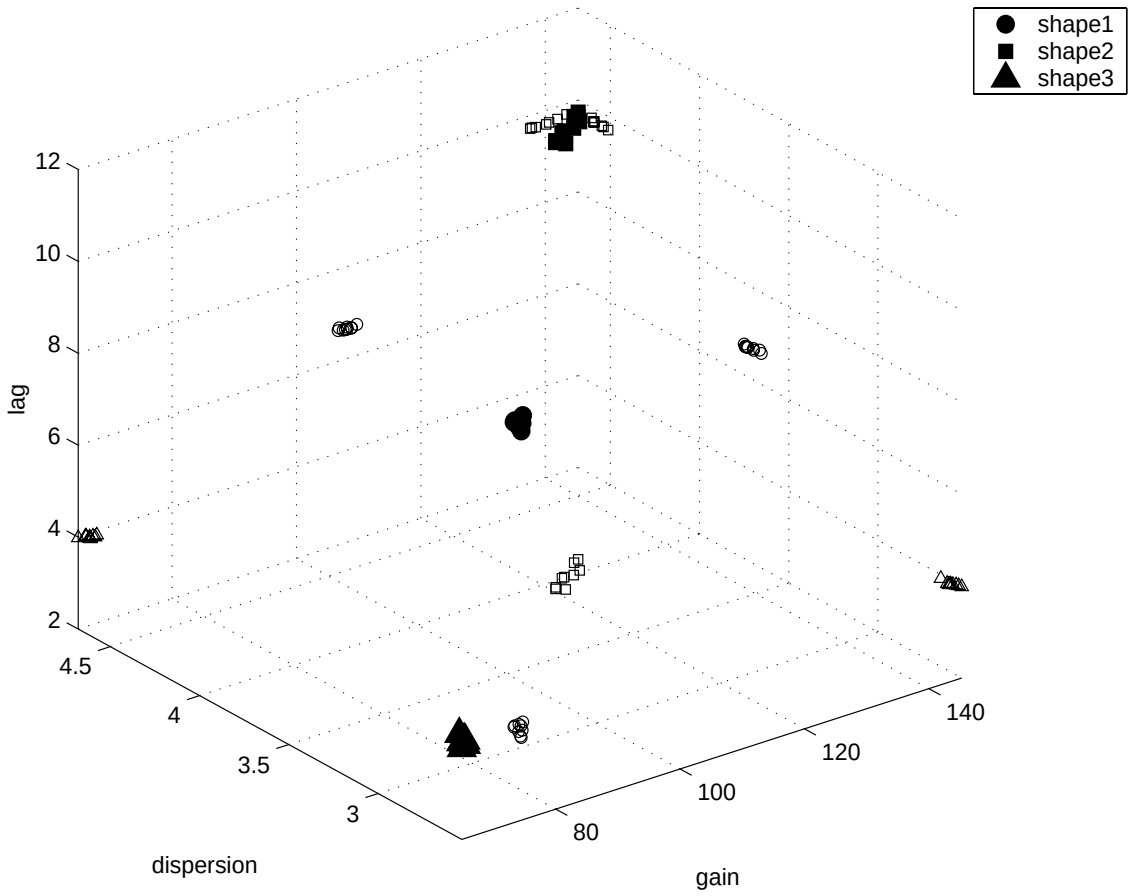

Figure 7.15: Synthetic data, Experiment I, example feature plot. Each prototypical BOLD-response is mapped in 3D feature space with a filled symbol. "Empty" symbols shows the projections from 3D feature space to each of the three planes. Signal amplitude is 5%

7.1.4 Experiment II: Kruggel & Cramon Model

This section reports on several experiments performed with the Kruggel & Cramon Model. From the synthetic dataset described in Section 7.1, a total of 20 ROI time series, each modulated with three different prototypical shapes (see Section 7.1.2), were selected. From each ROI time series 20 trials were extracted, each of which was sampled with 12 time points. Thus, a total of 1200 parameter estimates were obtained for each of the 5 signal amplitudes.

Kruggel & Cramon [27] suggests the Nelder & Mead Downhill simplex method for the parameter estimation. For the experiments in this section, this method together with the Levenberg-Marquardt method, was considered. Figure 7.16 shows the results from the estimation of eight consecutive trials. This signal is constructed from the prototypical BOLD-response, shape 1, and signal amplitude is 4%.

Tests of normality in the residuals were fulfilled for the majority of trials. These findings agreed with visual inspection of QQ-plots. Deviations were mainly present in trials with a low Signal to Noise Ratio and. In Table 7.3 summary statistics for prototypical BOLD-response, shape 3, in six sample ROI time series is given. The table displays parameter sets averaged over 20 ROI's in each of the six ROI time series. The estimation algorithm for this example is the Levenberg-Marquardt method and the signal amplitude is 4%. Each parameter estimate is presented with a 95% confidence interval (Matlab's `nlparci` was used for this purpose). The ROI time series listed in this table are identical with the ROI time series in Table 7.1.3.

To assess the robustness of the signal to increasing noise levels, all ROI's were evaluated for signal amplitudes ranging from 2-6% relative to the mean signal intensity level. An averaged parameter estimate was computed for each ROI time series resulting in 60 parameter sets for each signal amplitude. Results from estimation with the Levenberg-Marquardt method are shown in Figure 7.17. Figure 7.18 shows the results from estimation with Nelder & Mead Downhill simplex method. The largest departures from the true parameter values were found with the Nelder & Mead Downhill simplex method. This procedure also produced poor parameter estimates more frequently than the Levenberg-Marquardt method. This is especially noticeable for *dispersion* values of the prototypical BOLD-response, shape 2, and *lag* values of shape 3. Moreover, computation times per parameter estimate for the Levenberg-Marquardt method are approximately twice as fast compared to the Nelder & Mead Downhill simplex method. Based on these results we favor the Levenberg-Marquardt method for the parameter estimation of the present model.

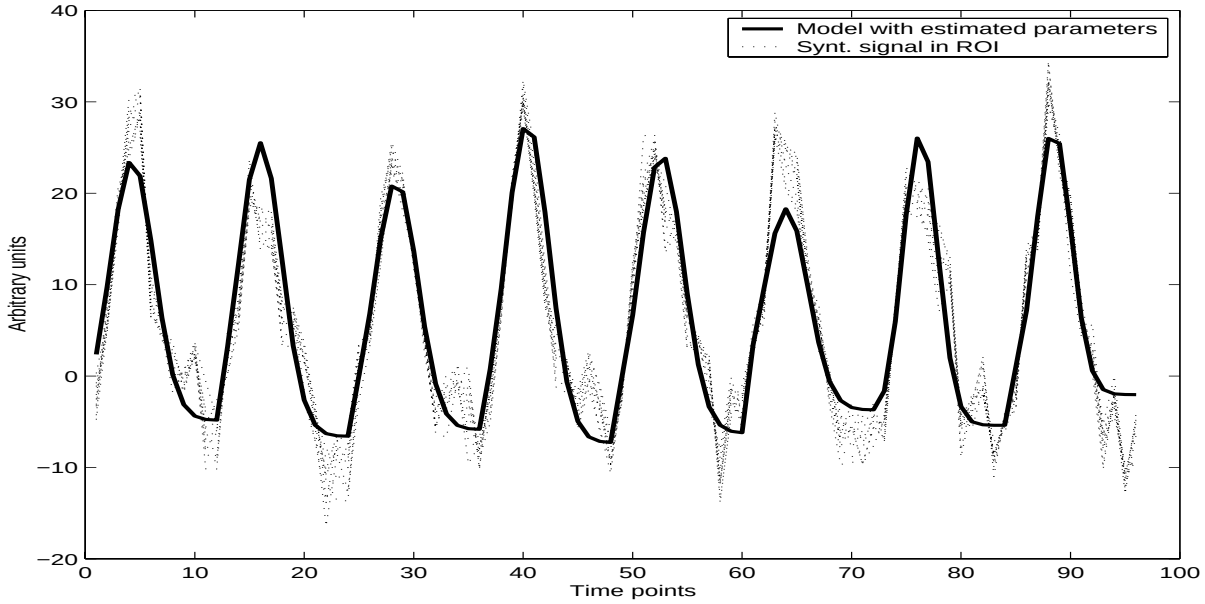

Figure 7.16: Synthetic data, Experiment II, prototypical BOLD-response, shape 1, eight consecutive trials with 12 time points each. Signal amplitude in this example is 4%

Location		θ_0 (gain)	θ_1 (dispersion)	θ_2 (lag)	θ_3 (baseline)
ROI 1	True	56.4506	2.5000	4.0000	-1.1290
	Estimated	65.0547 ∓24.7370	2.6981 ∓ 0.9803	3.9296 ∓ 0.8185	-1.326 ∓3.1653
ROI 2	True	53.7129	2.5000	4.0000	-1.0743
	Estimated	60.6850 ∓ 23.3116	2.5060 ∓ 0.9965	3.9230 ∓ 0.8223	-1.3395 ∓ 3.0044
ROI 3	True	58.9247	2.5000	4.0000	-1.1785
	Estimated	60.1267 ∓15.7736	2.5063 ∓ 0.5937	3.9961 ∓ 0.5214	-0.4993 ∓ 2.3512
ROI 4	True	70.2582	2.5000	4.0000	-1.4052
	Estimated	74.6687 ∓ 32.6574	2.6125 ∓ 1.1589	4.1944 ∓ 0.9362	-0.7206 ∓ 4.1922
ROI 5	True	59.4794	2.5000	4.0000	-1.1896
	Estimated	60.2500 ∓ 21.3372	2.3279 ∓ 0.9090	4.2150 ∓ 0.7358	-1.1556 ∓ 2.9579
ROI 6	True	62.6489	2.5000	4.0000	-1.2530
	Estimated	69.4466 ∓ 17.2870	2.7227 ∓ 0.7142	4.0630 ∓ 0.5755	-1.7150 ∓ 2.1327

Table 7.3: Synthetic data, Experiment II, parameter estimates for the prototypical BOLD-response, shape 3, in selected regions. Parameters and confidence intervals (95%) averaged over 20 ROI's in each ROI time series.

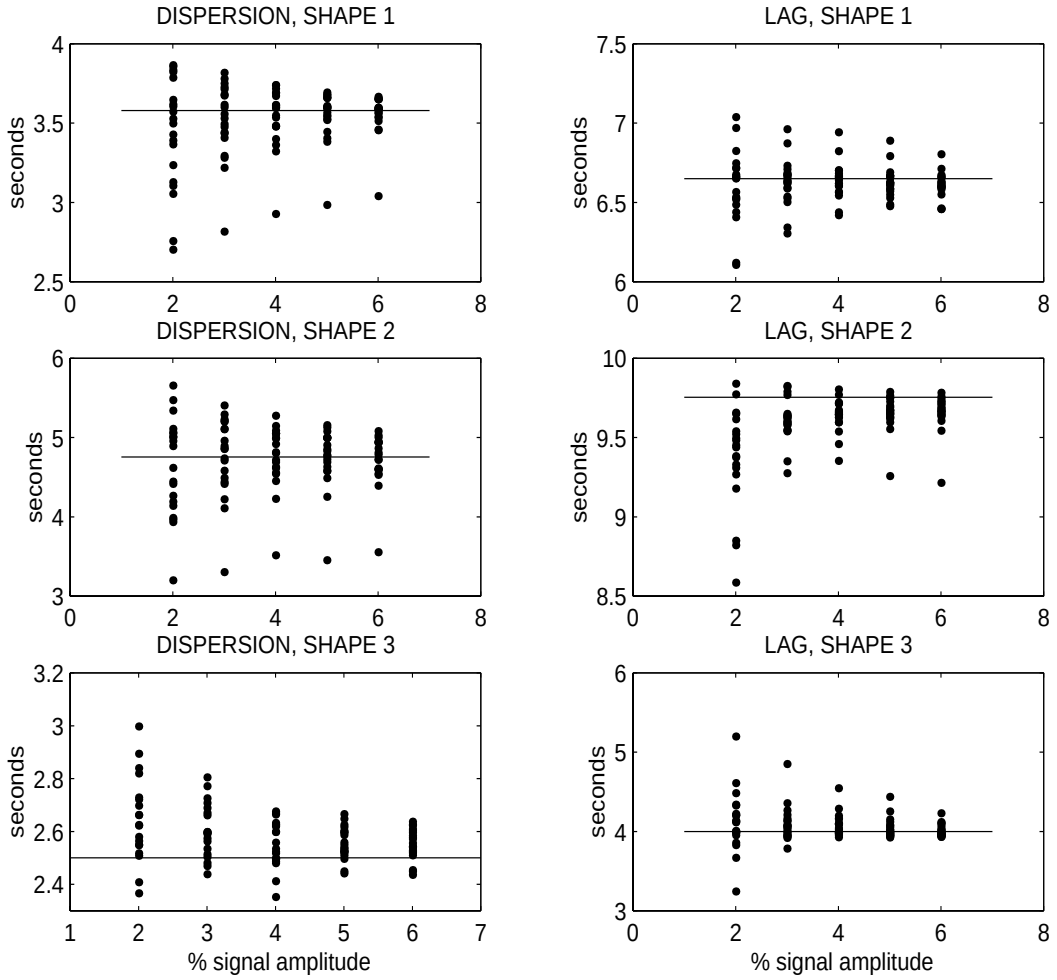

Figure 7.17: Synthetic data, Experiment II, dependency of the parameters, represented by *dispersion* and *lag*, on the signal amplitude. Signal amplitudes are 2-6% relative to mean signal intensity level. Estimation procedure : Nonlinear Least Squares by the Levenberg-Marquardt method

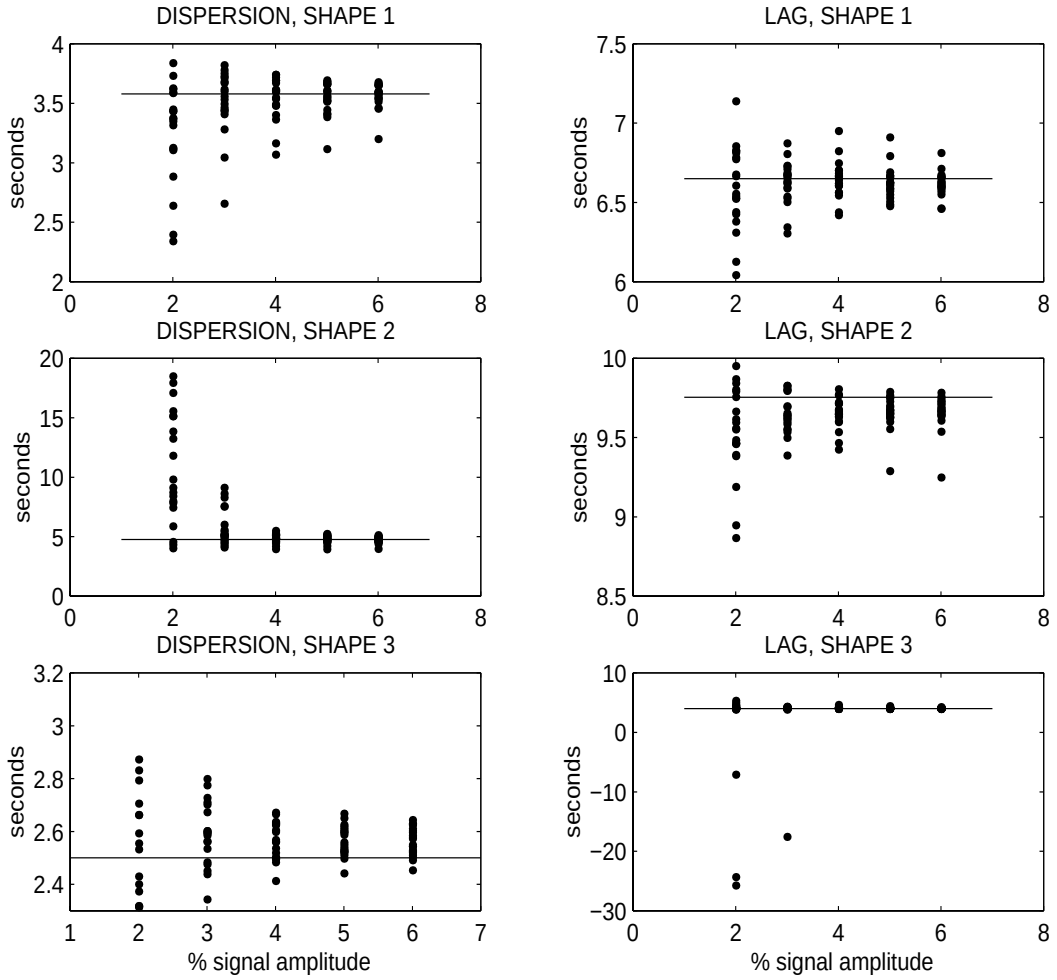

Figure 7.18: Synthetic data, Experiment II, dependency of the parameters, represented by *dispersion* and *lag*, on the signal amplitude. Signal amplitudes are 2-6% relative to mean signal intensity level. Estimation procedure: Nelder & Mead Downhill simplex method

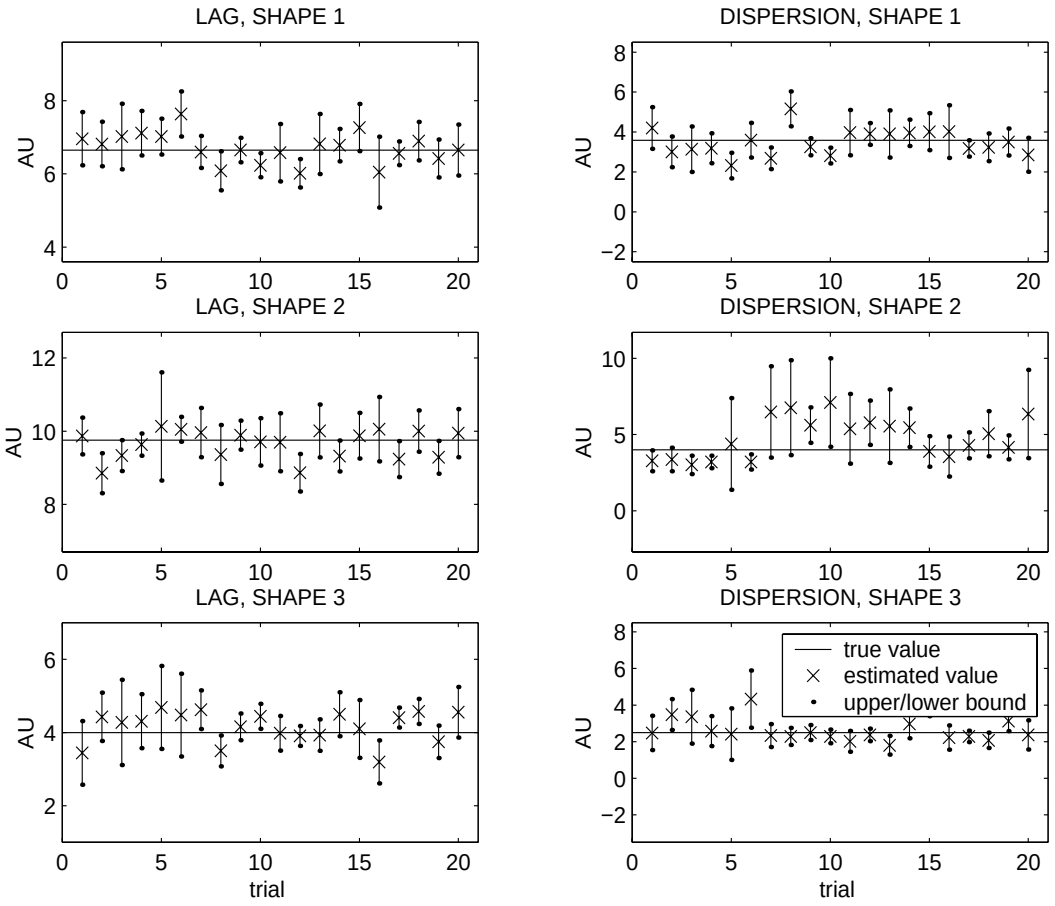

Figure 7.19: Synthetic data, Experiment II, estimated parameters with 95% confidence intervals for single trials. Estimation procedure: Nonlinear Least Squares by the Levenberg-Marquardt method. True parameter values for prototypical BOLD-responses, shape 1: $dispersion = 3.5798$ and $lag = 6.6502$, shape 2: $dispersion = 4.7553$ and $lag = 9.7541$, shape 3: $dispersion = 2.5$ and $lag = 4.0$. Signal amplitude is 4%.

To assess the deviation within single trials for a fixed ROI time series using the Levenberg-Marquardt method, 95% confidence intervals were derived for all parameter estimates. These results were then inspected to establish whether the true value could be found within the confidence interval or not. Signal amplitude used in these tests were 4%. Figure 7.19 illustrates these features. Each estimated parameter is plotted together with its 95% confidence interval. In most ROI time series 5-15% of the true parameters were located outside the confidence interval indicating that the synthetic BOLD-response was distorted by noise and not well fitted with our model.

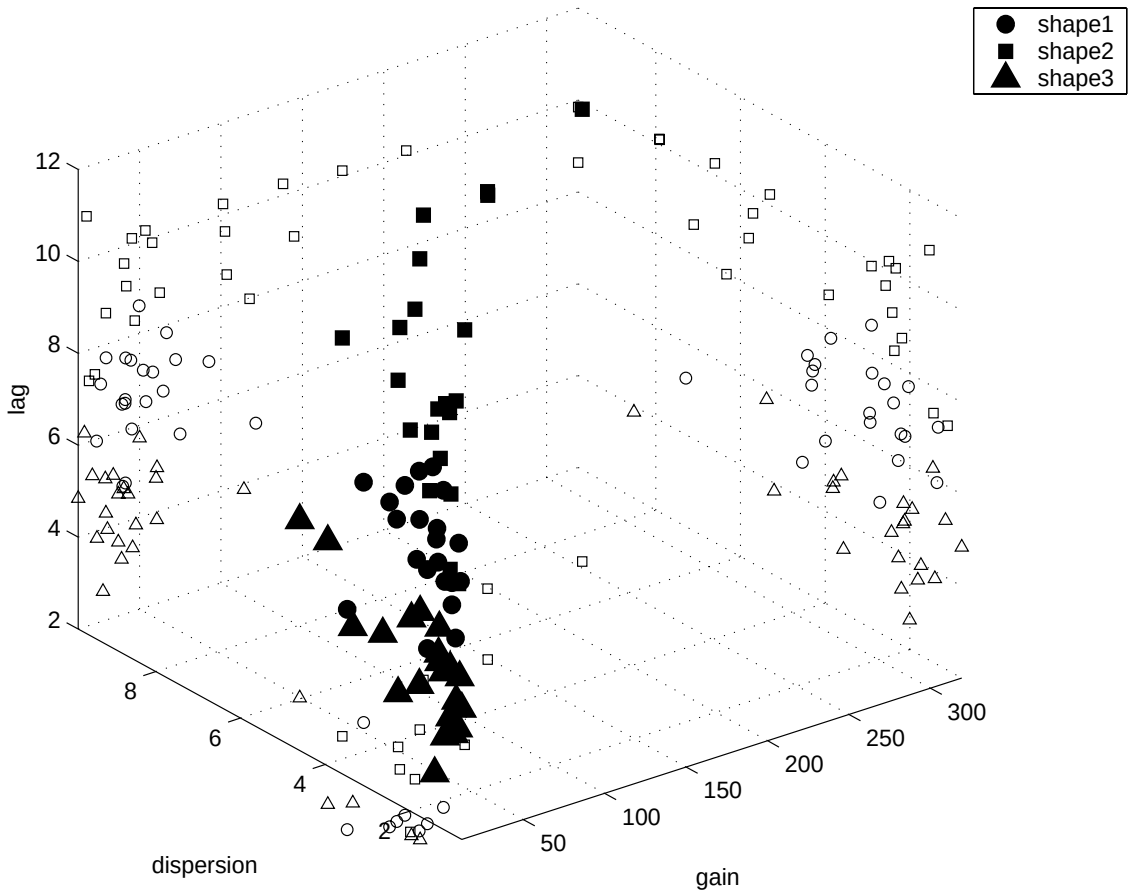

Figure 7.20: Synthetic data, Experiment II, feature plot. Each prototypical BOLD-response is mapped in 3D feature space with a filled symbol. "Empty" symbols shows the projections from 3D feature space to each of the three planes. Signal amplitude is only 2%. Estimation procedure : Nonlinear Least Squares by the Levenberg-Marquardt method

Feature plots (feature vector:[*gain*, *dispersion*, *lag*]) were generated to explore how well the different prototypical shapes could be distinguished from one another with increasing noise levels. Figures 7.20 and 7.21 demonstrates this idea. In Figure 7.20 the signal amplitude is only 2% and the prototypical shapes are partly overlapping. In this case it is difficult to differentiate between the three prototypical BOLD-responses. With a signal amplitude of 5% as illustrated in Figure 7.21 the three prototypical BOLD-responses are more easily distinguished. Compared to the feature plots in Experiment I (see Figure 7.15), however, the feature vectors within a given shape type are more scattered thereby complicating the discrimination of the response types.

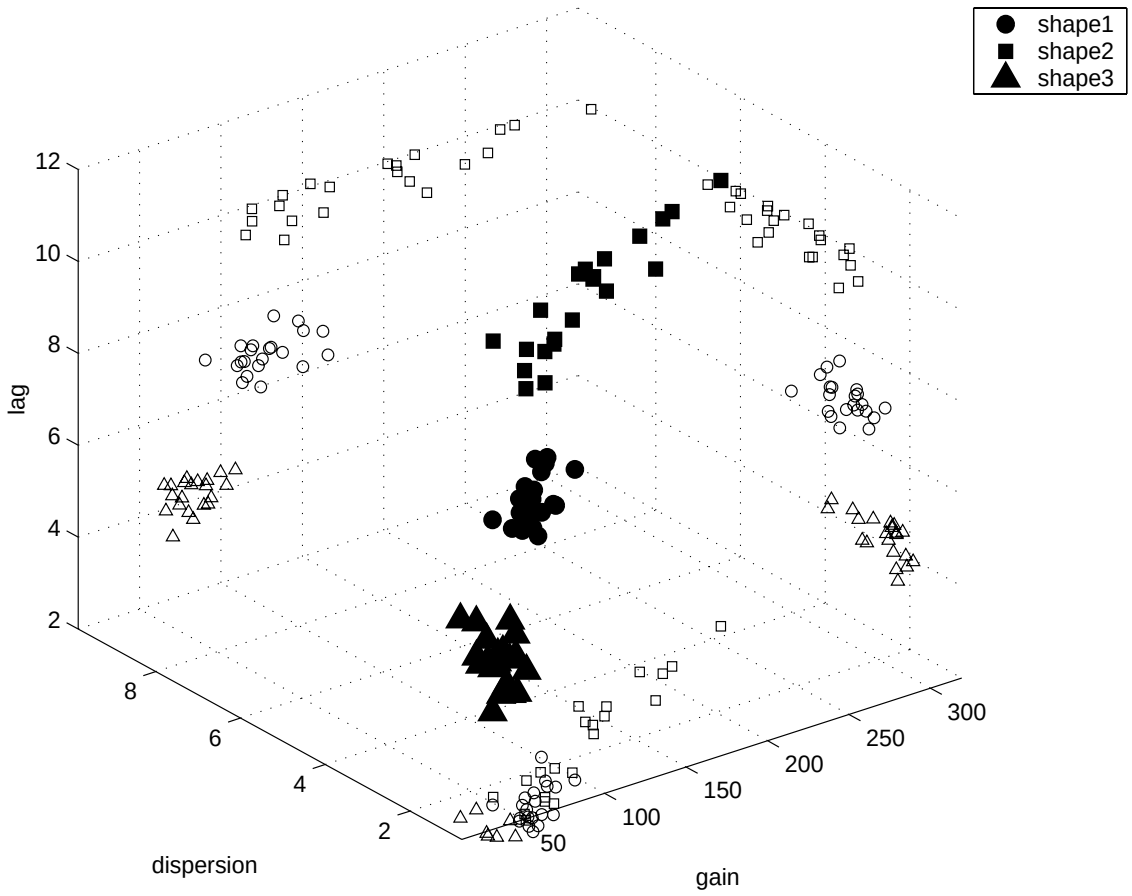

Figure 7.21: Synthetic data, Experiment II, feature plot. Each prototypical BOLD-response is mapped in 3D feature space with a filled symbol. "Empty" symbols shows the projections from 3D feature space to each of the three planes. Signal amplitude is 5%. Estimation procedure : Nonlinear Least Squares by the Levenberg-Marquardt method

Since the Kruggel & Cramon Model incorporates spatial information as well as temporal information, the high spatial correlation present in our synthetic data may explain the large distortions of the prototypical BOLD-responses. The Nonlinear Least Squares Model (Section 5.1) performs averaging over multiple trials, and ignores any spatial correlation between voxels. For the present model, however, the effects of spatial correlation seemed to yield poorer parameter estimates compared to the Nonlinear Least Squares Model.

7.1.5 Experiment: III Convolved Compartment Model

Experiments with the Convolved Compartment Model were performed on the same ROI time series as those used for the experiments with the Kruggel & Cramon Model. All ROI time series, each of which held 20 trials with 12 time points each, were modulated with two different prototypical BOLD-responses (shape 4 and 5, cfr. Section 7.1.2). Parameter estimates were obtained separately for all trials in each of the 40 ROI time series. The main intention for these experiments were

- to explore how well the model could approximate the prototypical BOLD-response, and furthermore
- to obtain estimates of the neuronal parameters (*gain*, *onset* of neuronal response (t_0) and *duration* of neuronal response (t_1)).

Due to the previously discussed difficulties with regard to the vascular parameters of the Convolved Compartment Model (see Section 6.5), we shall not attempt to interpret these parameters.

Parameter estimation procedures included both the Nelder & Mead Downhill Simplex Method and the Levenberg-Marquardt method. Preliminary experiments conveyed, however, that the better results were achieved using the Levenberg-Marquardt method. The parameter estimates found with the Nelder & Mead Downhill Simplex Method were generally further from the true parameter values than the corresponding parameter estimates found by the Levenberg-Marquardt method. Large departures from the true values also occurred much more frequently with the Nelder & Mead Downhill Simplex Method. Furthermore, there is a marked difference in computation times for the two algorithms, with the Levenberg-Marquardt method being the fastest of the two. The main body of experiments with the Convolved Compartment Model was therefore conducted using the Levenberg-Marquardt method for parameter estimation. All results presented below have been obtained with this method.

An example of a typical estimation result for the three neuronal parameters, *gain*, *onset* and *duration* of neuronal activity (see Section 5.3), and for both prototypical BOLD-responses is given in Table 7.4. Signal amplitude for this example is 4%. Neuronal *onset* times (t_0) were generally found to be below one second for prototypical BOLD-response, shape 4, and below two seconds for shape 5 and neuronal *duration* times (t_1) were in the range 2-6 seconds for shape 4 and in the range 6-10 seconds for shape 5. *Gain* was found between 5-13 AU (Arbitrary units) for shape 4 and 3-8 AU for shape 5.

Normality tests according to Lilliefors and Bera-Jarque (see Appendix A.4) in the residual distributions after estimation were fulfilled for the majority of the regions.

Figure 7.22 shows the synthetic and modeled signals in eight consecutive trials for a typical ROI time series. Signal amplitude is 4%. As the figure illustrates, an acceptable fit could not be achieved for all trials.

	Shape 4			Shape 5		
	gain	t_0	t_1	gain	t_0	t_1
True	7.0000	0.0500	4.6000	4.0000	0.2500	8.0000
Estimated	8.7906	0.0758	4.4340	4.9816	0.3178	8.6862
"	8.6837	0.0665	4.1884	4.5545	0.0147	6.0147
"	6.9935	0.5322	5.4678	3.7049	1.3022	4.6978
"	7.8754	0.2912	5.8232	4.0973	0.0000	8.8289

Table 7.4: Synthetic data, Experiment III: Neuronal parameters (*gain*, *onset* (t_0) and *duration* (t_1)). Results from 4 representative ROI's, prototypical BOLD-responses, shape 4 and 5, signal amplitude is 4%. Nonlinear Least Squares by the Levenberg-Marquardt method.

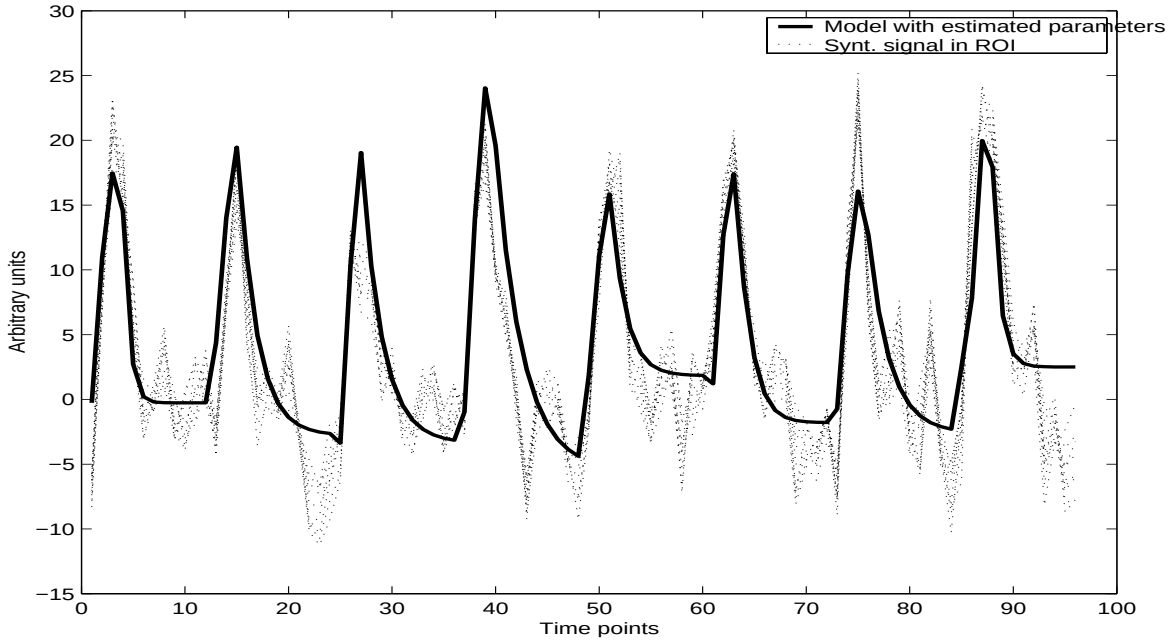

Figure 7.22: Synthetic data, Experiment III: Plot of synthesized (prototypical BOLD-response, shape 5) and modeled signal in eight consecutive trials. Signal amplitude is 4%.

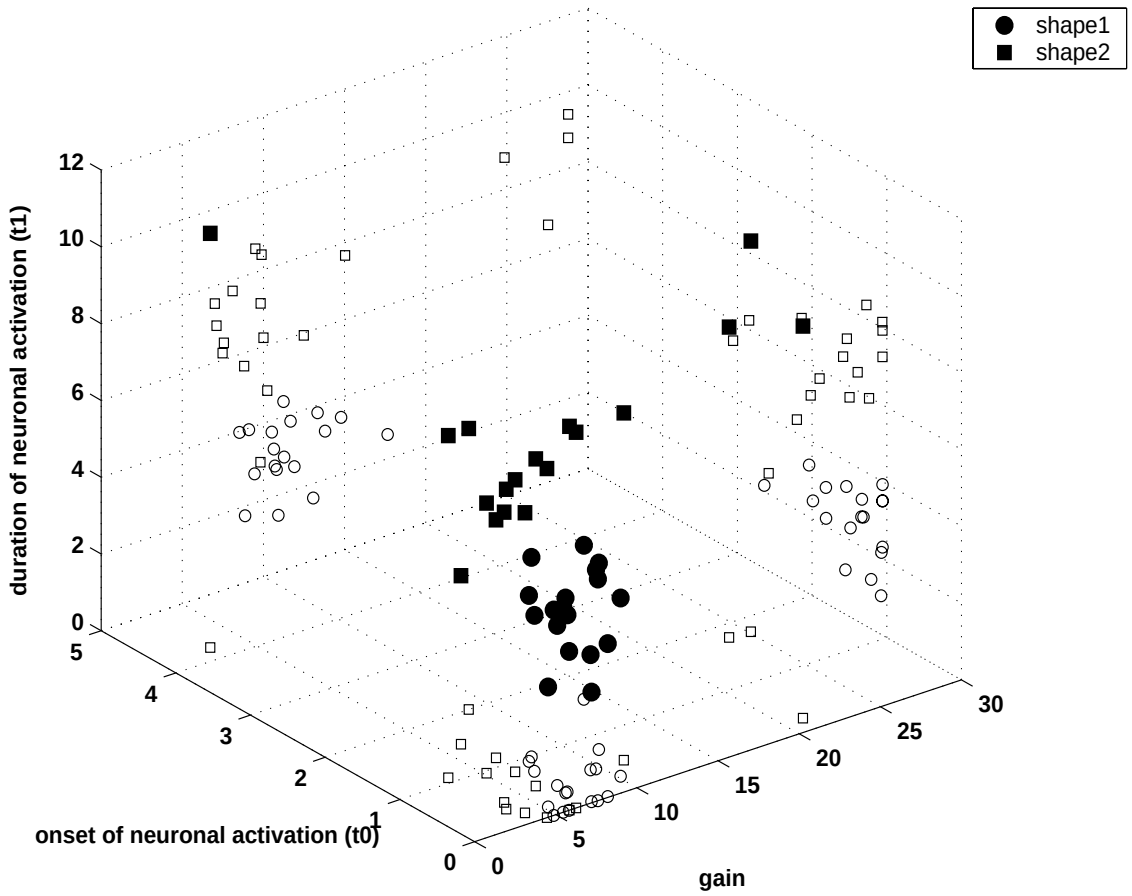

Figure 7.23: Synthetic data, Experiment III, feature plot. Each prototypical BOLD-response is mapped in 3D feature space with a filled symbol. "Empty" symbols shows the projections from 3D feature space to each of the three planes. Signal amplitude is 4%. Estimation procedure: Nonlinear Least Squares by the Levenberg-Marquardt method

Feature plots were generated based on the three neuronal parameters (*gain*, *onset* (t_0) and *duration* (t_1)). An example plot is shown in Figure 7.23. The two prototypical BOLD-responses can relatively easily be distinguished from one another. However, most BOLD-responses would be expected to appear with values somewhere in between the two neuronal parameter sets used for the prototypical BOLD-responses of this experiment (see Section 7.1.2). Especially the *onset* of neuronal activation cannot be expected to vary much for different BOLD-responses. These effects may reduce the power of the feature plots in deriving the characteristics of the neuronal parameters of the Convolved Compartment Model.

Our test results show that the Convolved Compartment Model is capable of approximating the two prototypical BOLD-responses used in our synthetic data. The Levenberg-Marquardt method was found to yield better estimates (with less computation time) than the Nelder & Mead Downhill Simplex Method. Neuronal parameters can be approximated and was mapped in 3D feature space.

7.2 Real Data

7.2.1 Experiment: IV : Signal Detection

ANOVAs ability to detect activation was tested on a data set from an event-related experiment performed at Haukeland University Hospital. The experiment was performed on a Siemens Vision Plus 1.5 Tesla scanner equipped with 25mT/m gradients. 50 BOLD sensitive Echo Planar Images (EPI, see Section 2.2.7) were acquired. Each measurement of 4 seconds consisted of 40 axial slices. Interscan interval was 6 seconds. With this temporal resolution only 4 scans were recorded per trial. The time between successive trials was 24 seconds.

At each trial the subject was instructed to *finger-tap* either with his *right* or *left* hand. Images were preprocessed and analyzed using the SPM software package (see Appendix A.3). Figures 7.24 and 7.25 shows the corresponding activation plots. As could be expected, *left* hand finger tapping leads to activation in the motor cortex of the right hemisphere, and visa versa for *right* hand finger tapping.

The collected signals for each voxel time series were organized in two $l \times o$ matrices, in which l is the number of time points per trial and o is the number of trials for each of the two trial types. In this experiment there were 4 time points per trial and 5 trials per trial type. Each voxel time series is organized such that there is one matrix for trial condition *left*, and one for trial condition *right* hand finger-tapping. The matrices are then subject to the ANOVA procedure (see Section 4.1).

The entire data set was analyzed with the ANOVA procedure. The initial hypothesis states that there is no significant activation. Assessing the F-critical value with the corresponding degrees of freedom (df), which for this experiment is $\mathrm{df}_{numerator}$=3 and $\mathrm{df}_{denominator}$ = 16, we find that the hypothesis can be rejected if F exceeds 9.00. This is the F critical value at a 0.1% level, which means that 0.1% of reported activation may be erroneously.

The results from this analysis were then compared to the results from the SPM analysis. Depending on the tresholding, all voxels labeled as activated by the SPM were also detected by ANOVA. ANOVA generally yielded a moderately larger number of activated voxels than the SPM. Basically, ANOVA compares several measures of the mean, and the null hypothesis states that there are "no difference" in the means. Any time series with significant deviations from the mean may therefore be labeled as active. This makes ANOVA equally good at detecting de-activations as activations. Normally, the results should therefore be subject to further investigation/analysis.

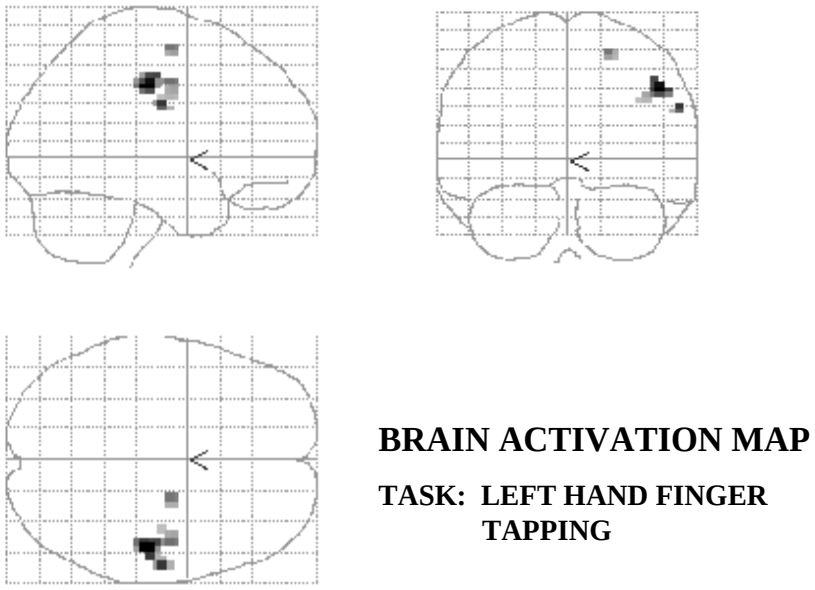

Figure 7.24: Real data, Experiment IV: activation plot. Trial type is *left* hand finger tapping.

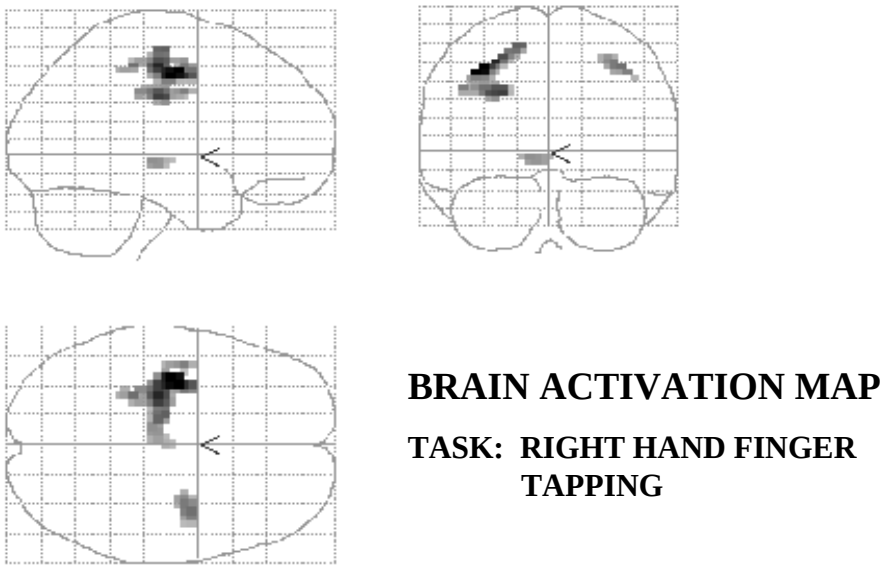

Figure 7.25: Real data, Experiment IV: activation plot. Trial type is *right* hand finger tapping.

ANOVA makes no assumptions about the time course of the BOLD-response. The procedure is therefore potentially capable of detecting responses with different shapes across the cortex. With the temporal resolution of the current experiment (4 observations per trial), however, there is little chance of further investigating such differences.

An example matrix from a voxel in the left hemisphere, *left* hand finger-tapping, is given in Table 7.5.

			Trial		
	712	713	714	706	703
Time	711	717	709	712	704
	710	714	704	716	704
	704	705	712	711	707

Table 7.5: Real data, Experiment IV, ANOVA: Voxel values in a activated voxel in the left hemisphere, *left* hand finger tapping. The F-ratio is 0.3053 and the null-hypothesis is not rejected

The F-value for the data in Table 7.5 was found to be 0.3053 and consequently the null hypothesis cannot be rejected. This was expected since *left* hand finger tapping basically leads to activation in the right hemisphere. Table 7.6 gives an example of an activated voxel in the right hemisphere, *left* hand finger tapping. The F-ratio for this voxel is 21.0648 and clearly indicates that the null hypothesis should be rejected. Figure 7.26 gives an illustration of the corresponding time courses.

			Trial		
	706	718	713	714	712
Time	729	727	718	730	723
	709	706	709	715	708
	700	704	703	699	712

Table 7.6: Real data,Experiment IV, ANOVA: Voxel values in a activated voxel in the left hemisphere (same voxel as in table 7.5, *right* hand finger tapping. The F-ratio is 21.0648 and the null-hypothesis is rejected at the 0.1% level.

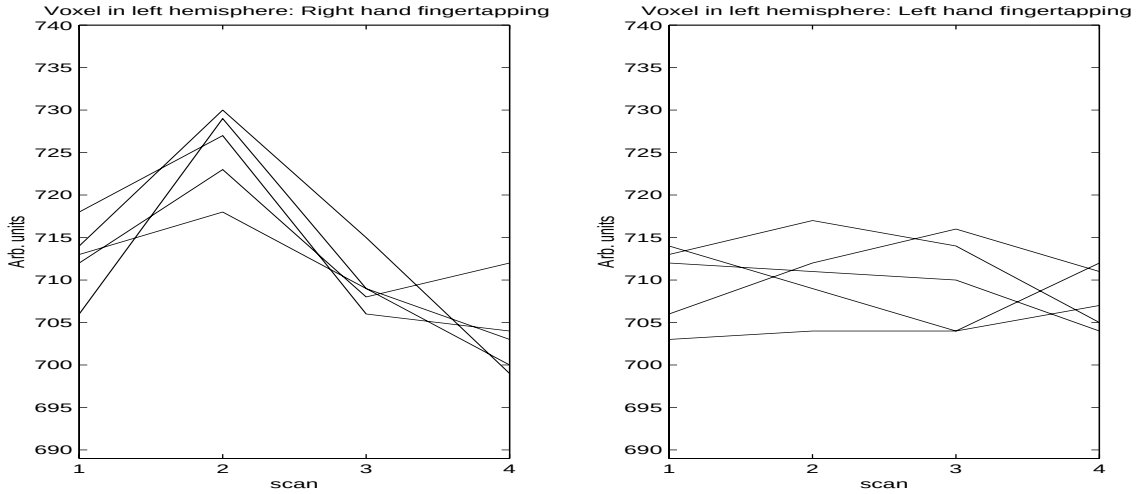

Figure 7.26: Real data, Experiment IV, time course for voxel in motor cortex of the left hemisphere, (a) *right* hand finger tapping, and (b) *left* hand finger tapping.

7.2.2 Experiment V : Signal Description

The fMRI dataset employed in this experiment was obtained for a language comprehension study. On a Siemens Vision Plus 1.5 Tesla scanner at Haukeland University Hospital, 501 echo-planar images (EPI, see Section 2.2.7) were collected (TE = 60ms, TR=0.6ms, flip angle 90°, FOV 200×200 mm, scan time 2 sec). Each volume consists of 20 slices of 64×64 voxels and a spatial resolution 3.13×3.13×4 mm. A corresponding anatomical image (3D FLASH, see Section 2.2.7) was acquired in the same session.

While in the scanner, Norwegian *words* versus *non-words* were presented randomly intermixed, to the subject on a visual display. The stimuli were presented with inter-stimulus interval ranging from 1-14 seconds. The subject was to respond to a *word* by pressing a right hand button, and to a *non-word* by pressing a left hand button.

The dataset was preprocessed and analyzed with the SPM99 software package (see Appendix A.3). Figures 7.27 and 7.28 illustrates the location of activated areas for trial types *non-word* and *word*, respectively. In locating areas of activation suitable for the signal description problem, the voxel time series for the activated areas were first subject to visual inspection. To reduce the effect of summation of closely spaced trials, only trials in which a *word* was followed by a *non-word* and visa versa, were selected for further investigations. Furthermore, trials with "long" inter-stimulus intervals (8-12 seconds) were chosen.

A total of 7 different ROI time series were chosen, 4 ROI time series for trial type *word* and three ROI time series for trial type *non-word*. In these ROI time series a total of 18 trials were selected for the experiments to follow. Baseline correction was performed separately for all voxels. Each trial is represented by a ROI of nine voxels in a 3×3 voxel grid and 12 time points. Activation were found to be in the order ∼2-4% relative to mean signal intensity level.

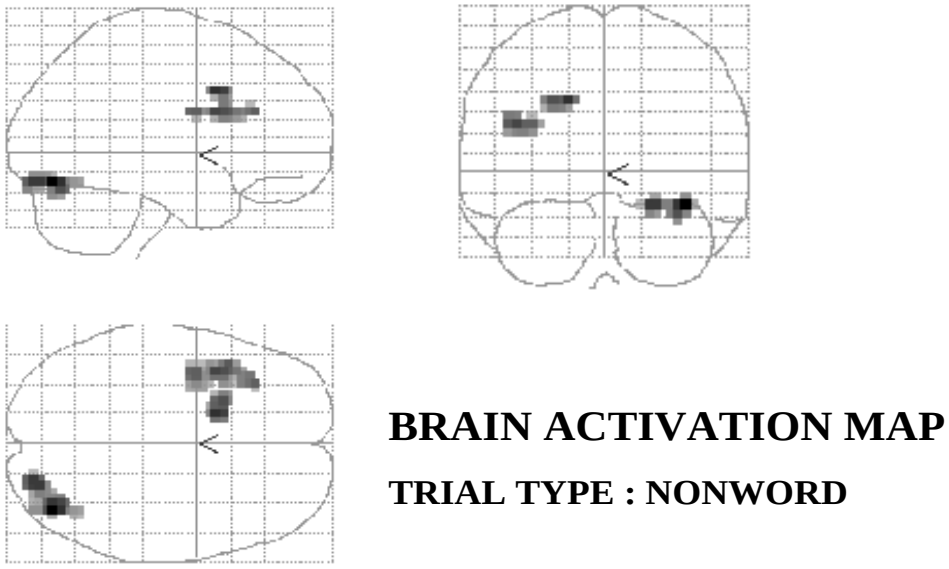

Figure 7.27: Real data, Experiment V: activation plot. Trial type *non-word*.

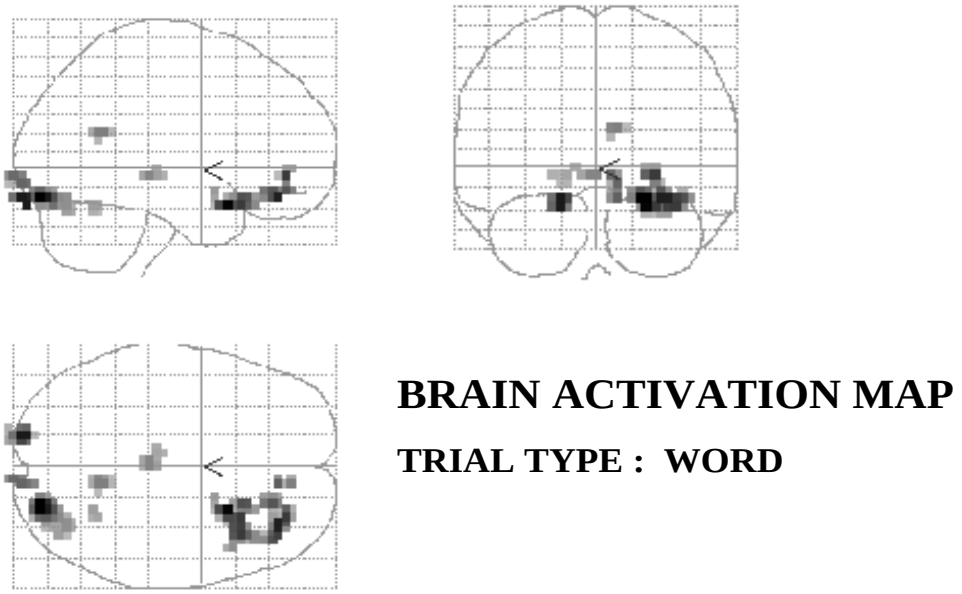

Figure 7.28: Real data, Experiment V: activation plot. Trial type *word*.

Nonlinear Least Squares Model on real data

The purpose of this experiment was to explore how well the Nonlinear Least Squares Model, as described in Sections 5.1 and 6.3, can model the observed BOLD-response and, furthermore, detect differences in the response for different trial types.

To reduce noise, averaging over all trials in the ROI time series was performed for each trial type, resulting in a 9×12 matrix for each trial type. One parameter vector was then obtained for each voxel in all ROI time series. As Table 7.7 illustrates, there is a pronounced difference in the averaged parameter estimates for the two trial types. The responses to *non-word* trials were found to have a shorter rise time and a lower signal intensity than *word* trials. Additionally, the response duration for *word* trials are generally wider/longer than for *non-word* trials. After having reached the maximum value, the observed signal in the case of *word* trials decreases rapidly at first, after which a more prolonged return to baseline is observed. This behaviour is rather difficult to modulate exactly with the Gaussian modeling function. Figure 7.29 shows the observed versus modeled signal for this trial type. As expected, the modeled signal differs from the observed signal especially in an interval around the maximum value. A better fit was found for the *non-word* trials. Figure 7.30 illustrates the observed versus modeled signal for the *non-word* trial type.

Trial : WORD				Trial : NON-WORD			
Gain	Dispersion	Lag	Baseline	Gain	Dispersion	Lag	Baseline
71.4789	5.6356	9.3513	-5.4529	46.9579	3.8239	7.8306	-4.2432
121.9622	7.7006	9.8671	-10.0641	38.5573	3.2713	7.6399	-3.4777
164.8185	8.9174	9.9756	-13.4761	25.8756	2.6165	7.4444	-2.1123
77.2050	5.8426	9.5321	-5.9962	44.3202	3.7315	7.6907	-3.6745
98.1077	6.9066	9.8297	-8.2650	35.0486	3.0951	7.5361	-2.7382
96.3070	7.0793	9.7886	-8.5887	25.5332	2.5856	7.4272	-1.7522
56.9126	4.9414	9.1135	-4.3880	36.3496	3.5507	7.6146	-2.7151
52.9905	4.9850	9.2223	-4.5205	32.1598	3.0040	7.4678	-2.2407
48.6270	5.0177	9.1735	-4.5024	24.9860	2.7060	7.4654	-1.6274
87.6010	6.3362	9.5393	-7.2504	34.4209	3.1538	7.5685	-2.7313

Table 7.7: Real data, Experiment V. Parameter estimates for the nine voxels in a ROI time series, averaged over 18 trials, trial types *word* and *non-word*. The bottom row shows the mean parameter values.

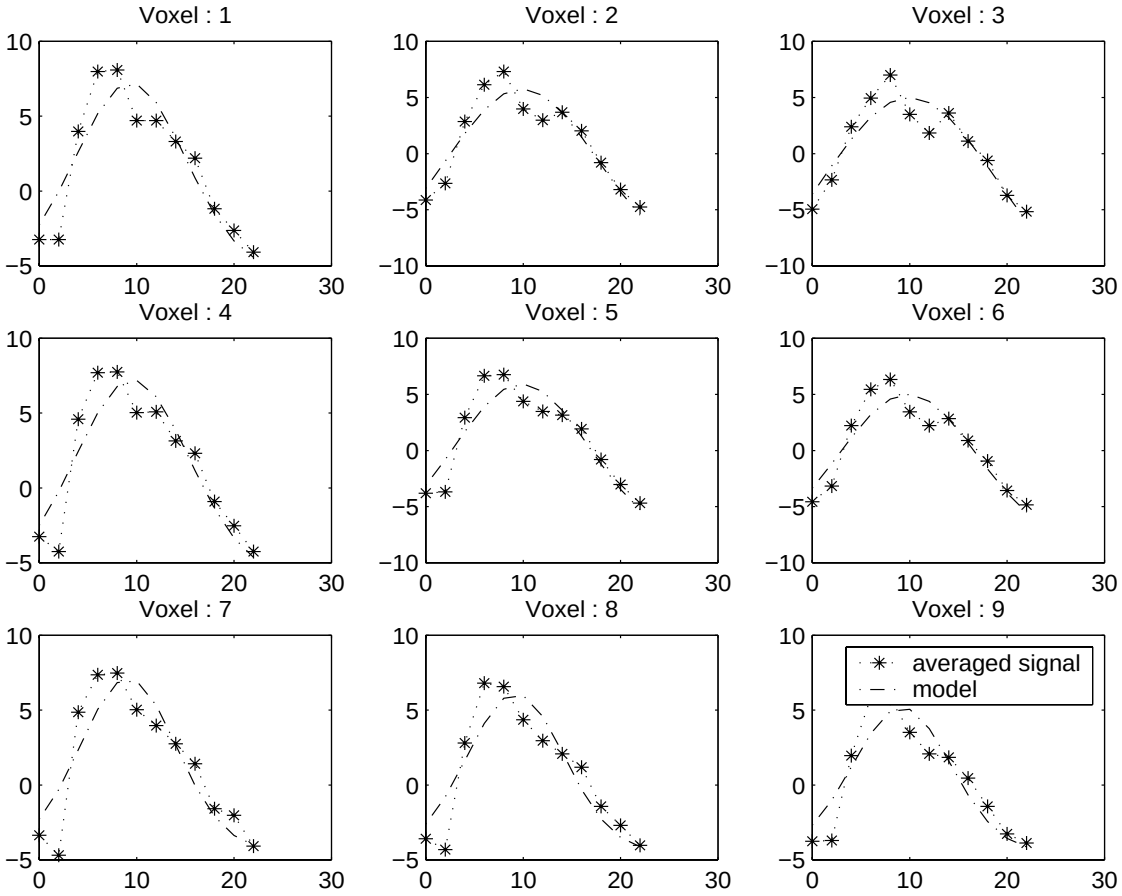

Figure 7.29: Real data, Experiment V, *word* versus *non-word* discrimination task. Parameter estimates for a ROI time series averaged over 18 trials, trial type: *word*. Time-locked to stimulus averaging of observed time course over all trials is denoted by star dots. The estimated model signal time course is denoted by solid line.

Figure 7.31 shows plots of single trials and the corresponding modeled signal constructed from the averaged parameter sets (cfr. Table 7.7). In Figure 7.32 the modeled signals for trial types *word* versus *non-word* can be visually compared. The differences between the two types of responses are clearly demonstrated.

QQ-plots were generated for a visual inspection of normality in the residuals. All plots conveyed residual distributions in good accordance with normality. An example plot is given in Figure 7.33, in which the residual distribution for trial type *non-word* is plotted versus a normal distribution. Normality tests according to Lilliefors and Bera-Jarque (see Appendix A.4) confirmed normality in all residuals for both trial types.

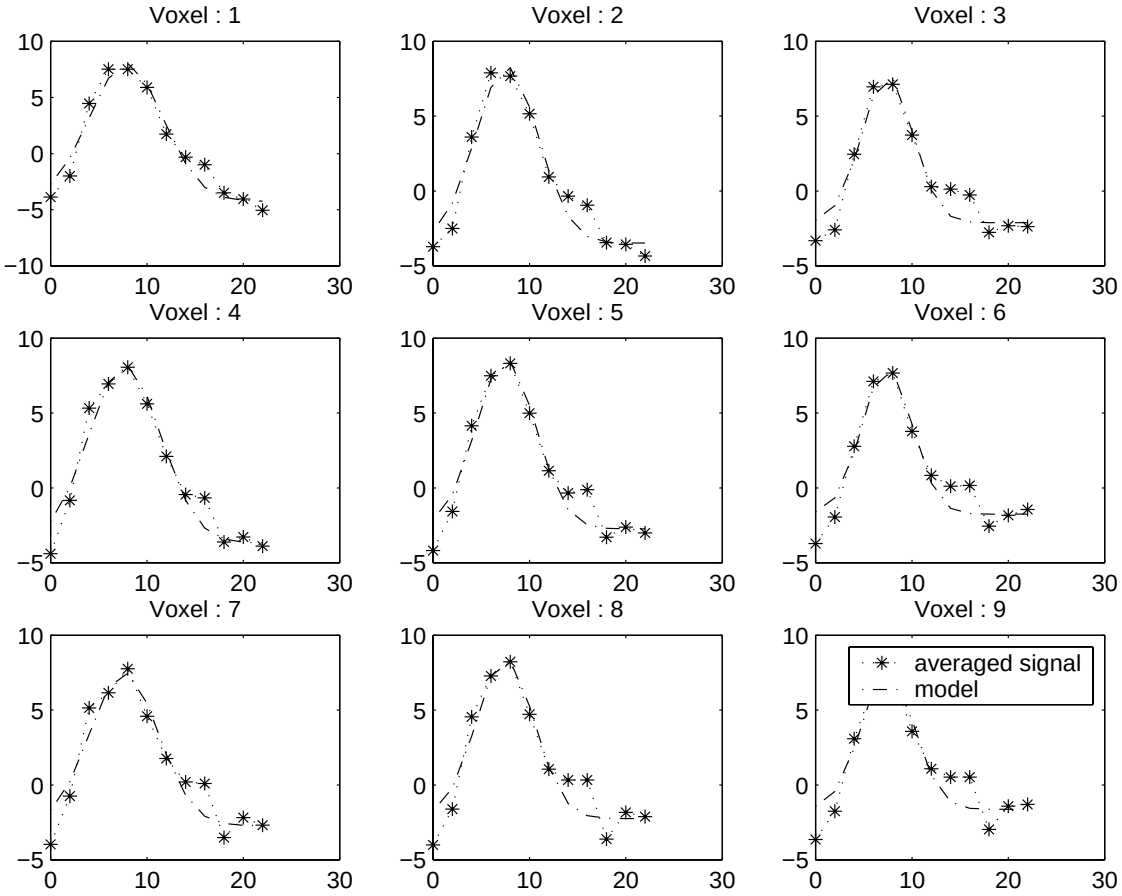

Figure 7.30: Real data, Experiment V, *word* versus *non-word* discrimination task. Results from estimation, averaged over 18 trials, trial type: *non-word*. Time-locked to stimulus averaging of observed time course over all trials is denoted by star dots. The estimated model signal time course is denoted by solid line.

The feature plot (see Figure 7.34) maps the estimated parameters $gain(\theta_0)$, $dispersion(\theta_1)$ and $lag(\theta_2)$ in 3D feature space. *non-word* trial characteristics can easily be identified. *word* trial characteristics are, however, more scattered but clearly (linearly) separable from *non-word* trials. To our knowledge, these findings in haemodynamic response features have not been reported before. However, data are sparse, just one er-fMRI experiment, and should be confirmed by a more extensive experimental study.

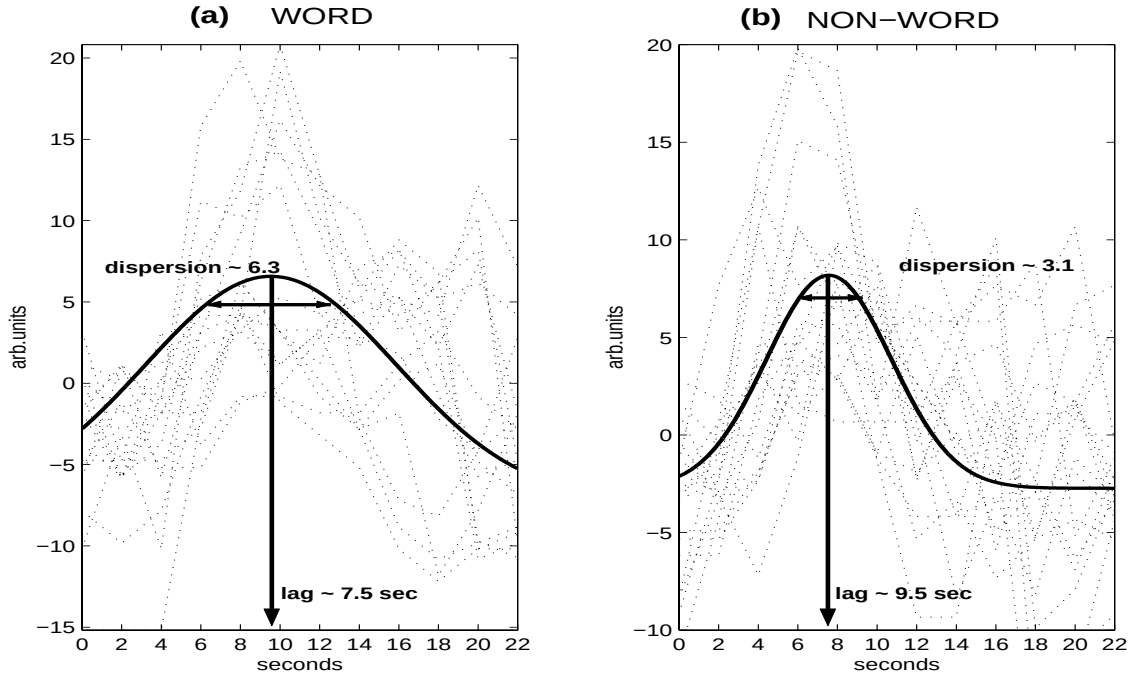

Figure 7.31: Real data, Experiment V, *word* versus *non-word* discrimination task, Nonlinear Least Squares Model: Plot of single trials (dotted lines) and averaged modeled signal (solid line). (a) Trial type *word*: "Height" of response is given by $\theta_0/\theta_1 \sim 87.6/6.3 = 13.9$ which yields a maximum value of 6.6 (baseline + θ_0/θ_1). This value is reached after approximately 7.5 seconds (lag). (b) Trial type *non-word*: "Height" of response is given by $\theta_0/\theta_1 \sim 34.4/3.1 = 10.9$ which yields a maximum value of 8.2 (baseline + θ_0/θ_1). This value is reached after approximately 9.5 seconds (lag). (cfr. Table 7.7 for the exact averaged parameter values.)

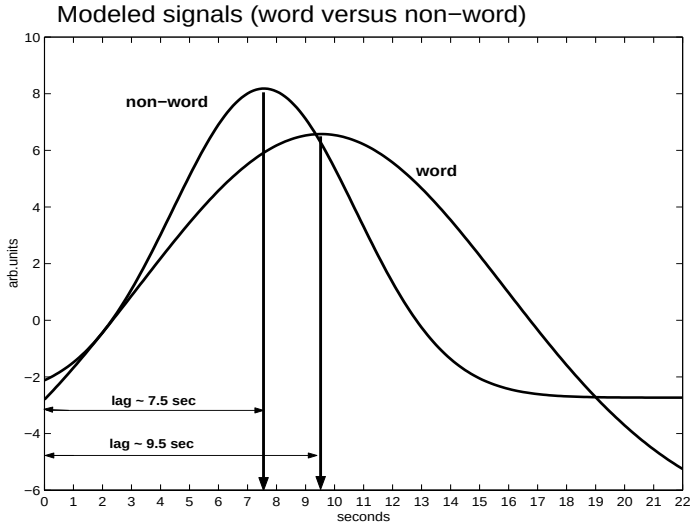

Figure 7.32: Real data, Experiment V, *word* versus *non-word* discrimination task, Nonlinear Least Squares Model: Signals constructed from averaged parameter estimates for the two trial types. (cfr. Table 7.7 for the exact averaged parameter values.)

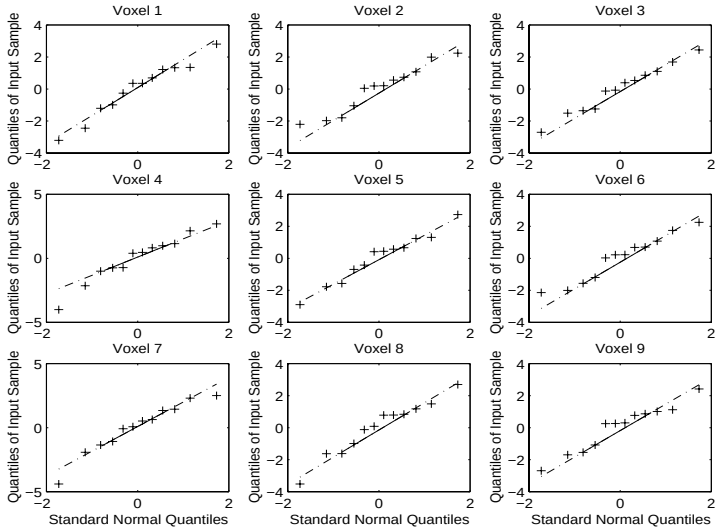

Figure 7.33: Real data, Experiment V, *word* versus *non-word* discrimination task. QQ Plot of Sample Data residual, averaged over 18 trials, versus Standard Normal. Trial type: *non-word*.

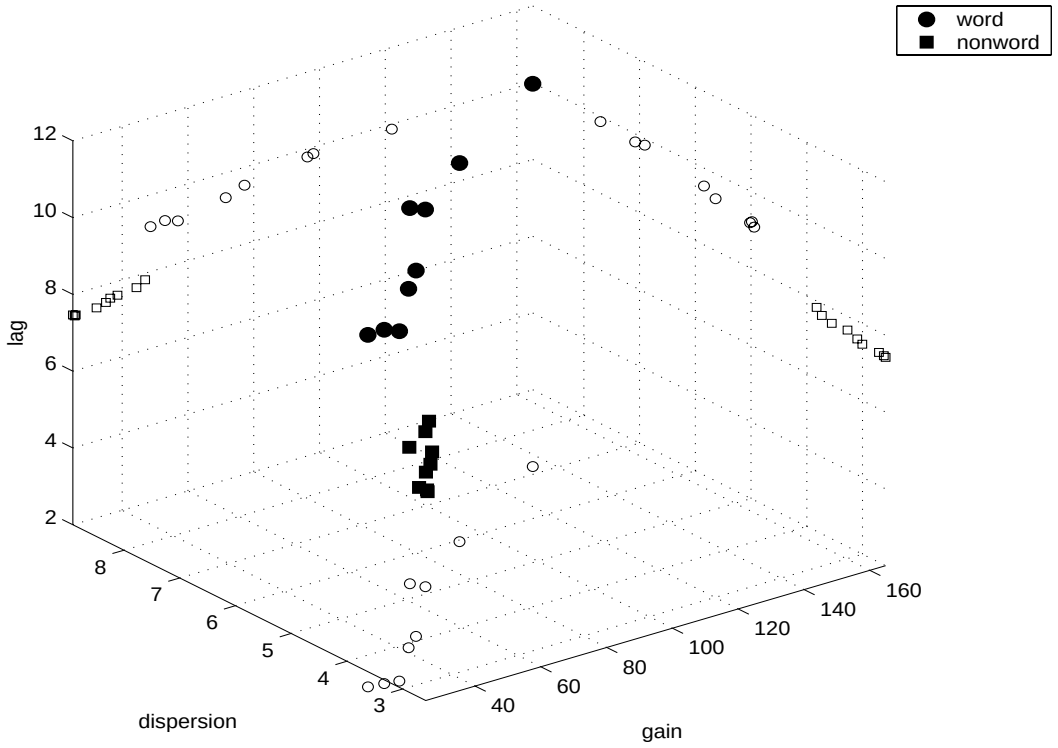

Figure 7.34: Real data, Experiment II *word* versus *non-word* discrimination task: feature plot. Each trial type is mapped in 3D feature space with a filled symbol. "Empty" symbols shows the projections from 3D feature space to each of the three planes.

Kruggel & Cramon Model on real data

The Kruggel & Cramon Model estimates one separate parameter set for each trial in a ROI time series. For the current dataset, 36 trials from 7 ROI time series were selected for further investigations. In some of the trials, especially with a low Signal to Noise Ratio (SNR, see Section 2.2.8), the BOLD-responses were severely distorted or too deviant in the sample region to warrant a good fit. The largest deviations were found with the trial type *word*. In approximately 30% of the trials the model failed to achieve a satisfying adaption to the sampled fMRI signal. Averaged parameter estimates for the remaining trials in all ROI's can be found in Table 7.8.

Example plots from two different ROI time series are presented in Figures 7.35 and 7.36. The feature plot in Figure 7.37 confirms that the largest departures from the mean is seen for trial type *word*. For the *non-word* trial type, parameter characteristics can to some extent be determined, whereas for the *word* trial type no such conclusions can be drawn. Normality tests according to Lilliefors and Bera-Jarque(see Appendix A.4) confirmed normality in all residuals for both trial types.

Trial : WORD				Trial : NON-WORD			
Gain	Dispersion	Lag	Baseline	Gain	Dispersion	Lag	Baseline
36.7180	2.7870	7.5791	-2.8746	35.3099	2.9224	7.0675	-6.8290
141.1739	9.0585	13.0306	-10.6258	46.6619	3.6117	5.6928	-3.8845
24.7125	3.4014	9.2410	-1.7730	23.8989	2.9400	7.4773	-0.1459
307.0840	13.9128	11.1069	-19.5104	24.5346	1.3925	6.9339	-4.0164
11.8436	0.7712	6.9187	-2.3905	92.8113	3.9233	7.2863	-8.7572
143.6619	6.0329	8.8314	-12.0236	18.5327	2.6634	9.1248	-1.6461
36.9821	4.1456	6.0373	-5.0625	17.0727	2.0756	5.2713	4.4137
51.0206	3.8475	5.0568	-7.5863	25.9019	2.3142	8.3210	-0.3818
28.5196	0.4991	8.8485	4.3434	26.6279	3.3094	6.6119	-4.6454
10.5259	3.2079	6.5549	-2.3878	40.7389	0.4324	9.0343	-1.0107
57.8554	33.8455	15.9449	-2.8446	22.1474	2.0190	8.2904	0.0726
				24.4007	2.2089	7.0327	-5.2576
				15.4340	2.5000	8.9578	-1.4843
				61.6032	2.9931	6.9350	-4.8931
				65.3580	5.3831	7.8529	-6.2393
			Mean Parameter Values				
77.2816	7.4099	9.0136	-5.7033	36.0689	2.7126	7.4593	-2.9803

Table 7.8: Real data, Experiment V, *word* versus *non-word* discrimination task, Kruggel & Cramon Model. Parameter estimates for trial types *word* (11 ROI's) and *non-word* (15 ROI's). The bottom row shows the mean parameter values for trial type *word* versus *non-word*.

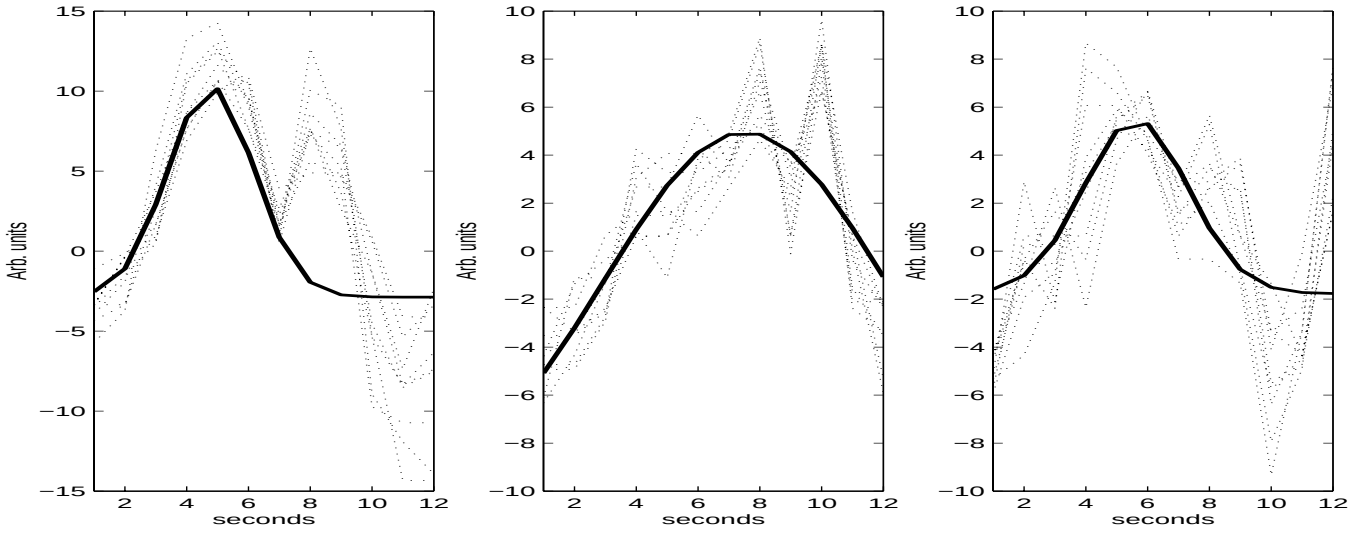

Figure 7.35: Real data, Experiment V, *word* versus *non-word* discrimination task, Kruggel & Cramon Model. Results from estimation in three trials, trial type: *word*. The observed signal is denoted by a dotted line and the modeled signal by a solid line.

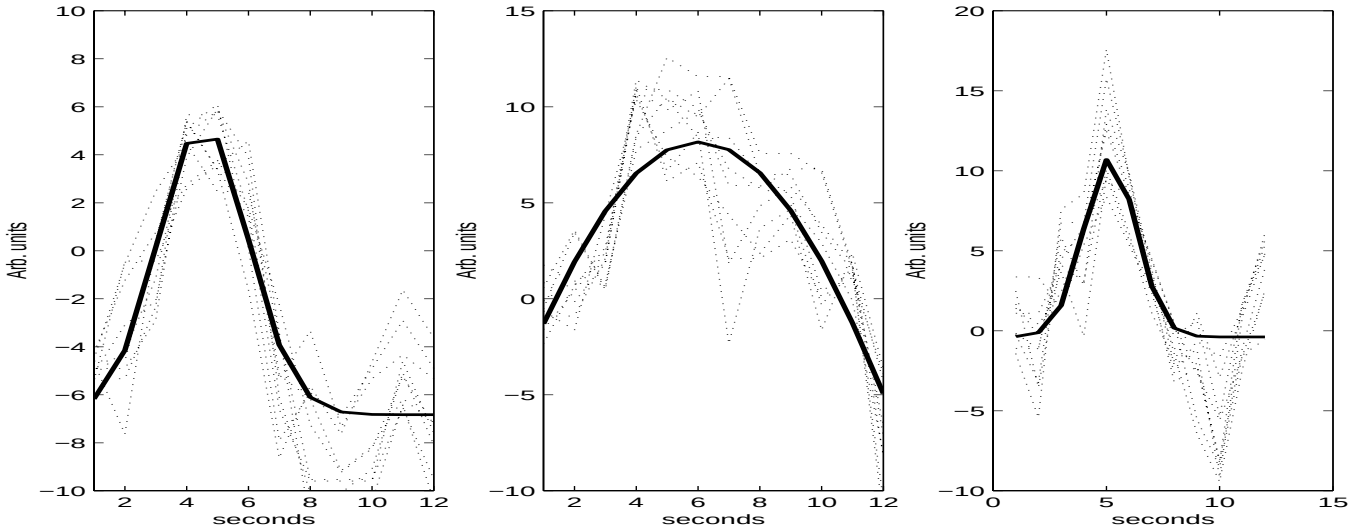

Figure 7.36: Real data, Experiment V, *word* versus *non-word* discrimination task, Kruggel & Cramon Model. Results from estimation in three trials, trial type: *non-word*. The observed signal is denoted by a dotted line and the modeled signal by a solid line.

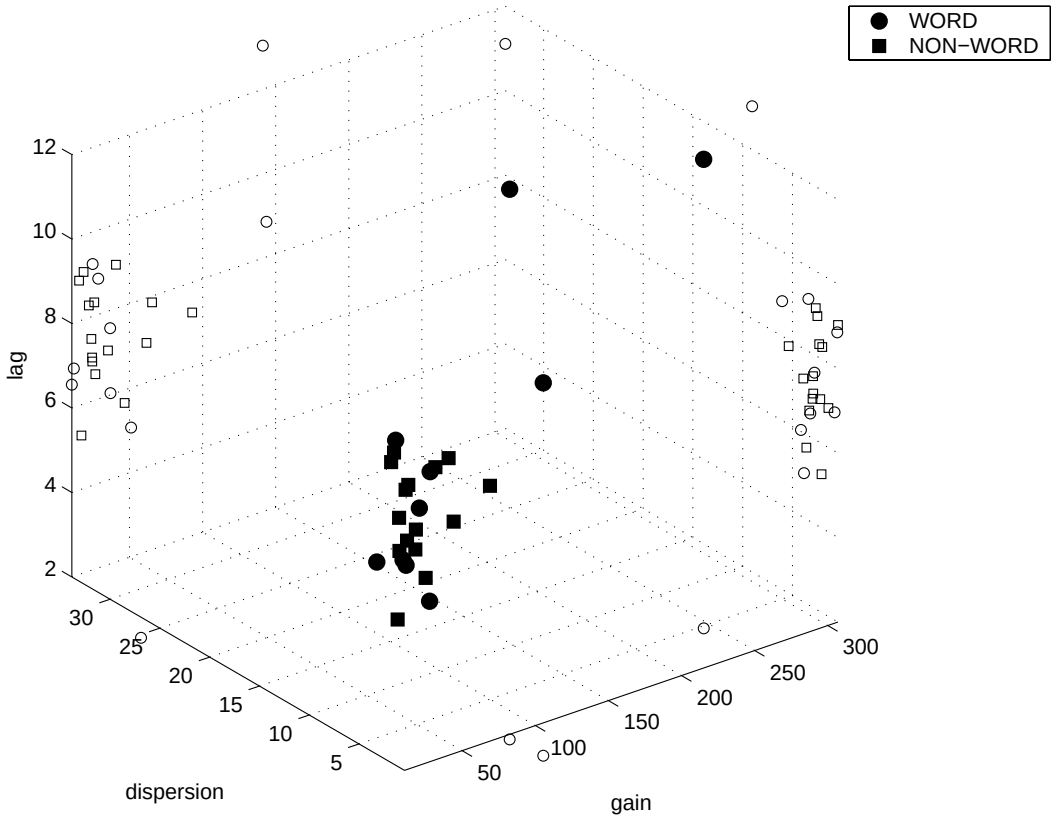

Figure 7.37: Real data, Experiment V, *word* versus *non-word* discrimination task, Kruggel & Cramon Model: feature plot. Each trial type is mapped in 3D feature space with a filled symbol. "Empty" symbols shows the projections from 3D feature space to each of the three planes.

Our test results suggests that the approach taken in the Kruggel & Cramon Model are not as suitable for describing the observed BOLD-response as the approach taken in the Nonlinear Least Squares Model. The responses approximated by the Kruggel & Cramon Model for the two trial types, especially for the *word* trial type, cannot readily be characterized. A high spatial correlation was revealed in the fMRI data set of this experiment. For the spatial pattern illustrated in Figure 7.4, correlation coefficients in the x and y-directions (see Section 5.2) were calculated to be in the range 0.95-1.0 for preprocessed and smoothed data. In the Nonlinear Least Squares Model averaging for each trial type was performed over 18 trials. The high spatial correlation found in the data and the fact that estimation in the Kruggel & Cramon Model is performed over only nine trials (from the nine voxels in a ROI) may explain some of the difference in results between the two models.

Chapter 8

Discussion and Conclusion

This work considers methods for the *detection* and *description* of stimulus induced brain activation in er-fMRI. The emphasis has been on methods for characterization of the evoked responses.

The chosen thesis subject is not only concerned with informatics, but deals also essentially with image processing, brain physiology, cognitive neuroscience, neuroradiology and aspects of MRI instrumentation and acquisition. Therefore, the work has evidently been an interdisciplinary enterprise. In evaluating the methods being described the aim was not only to consider issues related to mathematical modeling, but also an attempt to establish physiological interpretations of the model parameters. Physiological aspects are important both for the selection and evaluation of modeling functions. Parameters which are physiologically interpretable descriptors of the BOLD-response can readily be applied in multivariate analysis for comparison of for example duration of activation, reaction times and effects of learning, aging and different disease states.

The signal *detection* problem has been demonstrated with the ANOVA procedure, which basically locate activated regions by comparing estimates of the mean for all trials of the same type in a particular voxel. The signal *description* problem have been assessed on the basis of three models, the Nonlinear Least Squares Model and the Kruggel & Cramon Model, which both use a Gaussian function for the HRF, and the Convolved Compartment Model, in which the modeling function integrates both neuronal and vascular parameters. The fact that the neurovascular mechanisms behind the BOLD response is not well understood lead to models based on different physiological interpretations. In this work two such different models, the Convolved Compartment Model and the Balloon Model, have been described, with experimental work limited to the Convolved Compartment Model.

Most datasets acquired at Haukeland University Hospital have a sampling frequency of 4-8

time points (i.e brain volume acquisitions) per trial. These datasets are therefore not the best for the signal *description* problem. Due to the time limit on this work and the extensive resources needed in design, recording and analysis (signal detection) of fMRI experiments, we were only able to obtain one data set with a larger number of time steps per trial. This data set, based on a dichotic listening paradigm which was under construction, was described in Section 6.1. However, due to very low activation levels these data were not used in the signal *description* experiments.

Evaluation of the experimental results depends on whether the data are synthetic or real. For the synthetic data sets (observed fMRI time courses modulated with surrogate HRF functions), true parameters can be established prior to estimation procedures. Upon completion of the experiments the estimated parameters can be compared with the true parameters. Evaluation of results for the real data sets are somewhat more involved. Due to the lack of physiological experimental evidence these experiments should be regarded more as a feasibility study. However, results with our data were encouraging (especially on the word, non-word discrimination task) and follow-up studies of the signal *description* problem should therefore be conducted with better er-fMRI data, using carefully designed paradigms.

The main results can be summarized as follows:

Signal Detection using ANOVA

ANOVAs ability to detect activations have been tested on a real data set from an event-related fMRI experiment performed at Haukeland University Hospital. For comparison the data were also analyzed with the SPM software package (see Appendix A.3). We found that ANOVA and SPM detected voxel activation in the same brain regions. ANOVA, however, generally yielded a moderately larger number of activated voxels than the SPM, and the results should therefore be regarded as a starting point for further investigation.

Signal Description with the Nonlinear Least Squares Model

- A Gaussian function (see Equation (3.6)) was used in the modeling of the BOLD-response
- Noise reduction was performed by averaging over multiple trials time-locked to stimulus

- Parameter estimates were obtained with Nonlinear Least Squares by the Gauss-Newton method
- One set of parameters was estimated per voxel in all ROI time series

Experiments were performed on both synthetic and real data. The experimental results demonstrate that this model is stable against noise levels commonly observed in fMRI data. Considering the relatively high level of noise in our data, the parameter estimates for the synthetic data set are found to be highly satisfactory. Feature plots demonstrated that the three different prototypical BOLD-responses employed in this experiment could easily be distinguished even with signal amplitudes of only 2% relative to mean signal intensity level. For the experiments on real data, we were able to characterize differential responses in a *word* versus *non-word* discrimination task. Responses to *non-word* trials were found to have a shorter rise time and duration as well as a lower signal intensity than *word* trials (Figure 7.32). These results were illustrated in a feature plot of *word* versus *non-word* (Figure 7.34). To our knowledge, these findings in estimated haemodynamic response features in a word versus non-word discrimination task have not previously been reported.

Signal Description with the Kruggel & Cramon Model

- The Gaussian function (see Equation (3.6)) was used in the modeling of the BOLD-response
- Noise was collectively modeled in a covariance matrix and the temporal and/or spatial correlations in the residuals were applied as weights in a weighted least squares approach
- Parameter estimation was performed by the Levenberg-Marquardt method and/or the Nelder & Mead downhill simplex method
- One set of parameter estimates was obtained per ROI

Results from the experiments on synthetic and real data were not as good as in the Non-linear Least Squares Model, especially for the real data experiments. This model was also less robust in cases of low SNR (see Section 2.2.8). This was illustrated by plots in 3D feature space in which the three different prototypical BOLD-responses could easily be distinguished at a signal amplitude of 5%. With a signal amplitude of only 2%, however, the BOLD-responses could not be separated. Reasons for these difficulties may be found in

the high spatial correlation observed in our fMRI data sets. The Nonlinear Least Squares Model (Section 5.1) incorporates averaging over multiple trials ignoring any spatial correlation between voxels. For the Kruggel & Cramon Model, however, the high spatial correlation and the fact that the estimation of each parameter set is performed over only nine voxels (nine voxels in a ROI), are probable causes for the poorer parameter estimates. The Levenberg-Marquardt method was favored for the parameter estimation of the model concerned. We found this estimation procedure less likely to yield large departures from the true parameter values than the Nelder & Mead Downhill simplex method. Moreover, it was also approximately two times faster than the Nelder & Mead Downhill simplex method.

Signal Description with the Convolved Compartment Model

- A physiologically motivated response function (see Section 5.3), involving both "neuronal" and "vascular" parameters, was used in the modeling of the BOLD-response
- Noise was collectively modeled in a covariance matrix and the temporal and/or spatial correlations in the residuals were applied as weights in a weighted least squares approach
- Parameter estimation was performed by the Levenberg-Marquardt method and/or the Nelder & Mead downhill simplex method
- One set of parameter estimates was obtained per trial per ROI

In the initial evaluation of this model we found that two signals that per definition (see Section 6.5) were equal could be constructed from a number of relatively different parameter sets. Our test suggests that the landscape of the function to minimize (Equation (5.24)) is rather shallow for the vascular parameters. This may lead to similar sub-optimal solutions in a relatively wide parameter range. The uncertainty which arise from the high noise levels in fMRI data and the relatively few time points per trial may therefore influence the probability of multiple solutions (many local minima). It seems possible to give a physiological explanation, based on the dynamic relationship between the vascular transfer rates, of this phenomenon. Robust parameter estimates for the Convolved Compartment Model requires a large number of time points per trial. Therefore, the present rate at which time points can be sampled in er-fMRI experiments limits the performance of the Convolved Compartment Model. Consequently, only experiments on synthetic data were carried out. Using different pulse sequences (e.g Spin Echo and Gradient Echo EPI), which have their maximum sensitivity to specific aspects of the microvasculature [2], it could to

some degree be possible to obtain experimental evidence for the separation of "neuronal" and "vascular" parameters.
Our experiments with the Convolved Compartment Model confirmed the model's ability to approximate the prototypical BOLD-response and that neuronal response information can be derived from the (neuronal) parameters. As with the Kruggel & Cramon Model, the Levenberg-Marquardt method was less likely to yield large departures from the true parameter values than the Nelder & Mead Downhill simplex method. This estimation procedure was therefore also favored for the Convolved Compartment Model.

Main conclusions

- Simple averaging of time-locked to stimulus single trials combined with Nonlinear Least Squares estimation of model parameters have been found to be well suited for evaluating event-related fMRI data in terms of physiologically interpretable parameters.

- The Nelder & Mead Downhill Simplex Method has been suggested for the estimation of the physiological parameters in the Kruggel & Cramon Model [27]. We have successfully applied the Levenberg Marquardt Method for the parameter estimation thereby reducing computation times approximately with a factor of two per ROI.

- Our experience with the Convolved Compartment Model was not as successful as the two other signal description models. The main limitation for this model seems to be the insufficient number of observations that can be collected per trial with the currently available fMRI equipment. Our results imply that the model is stated more as a feasibility study than a "new method to evaluate the BOLD-response". This was also confirmed by Dr.Frithjof Kruggel at the Max Planck Institute of Cognitive Neuroscience (personal communication).

- Regarding physiological interpretations of the estimated parameters we selected three parameter estimates to be plotted in 3D feature space. This plot can potentially indicate if the joint distribution of the selected parameters are sufficiently separated to discriminate between different types of BOLD-responses. Feature plots may thus give information about underlying neuronal processing mechanisms. For the Nonlinear Least Squares Model and the Kruggel & Cramon Model we selected the parameters *lag*, *dispersion* and *gain* (which might express neuronal processing delay, processing duration or asynchrony and processing strength, respectively).

The main idea of extracting parameter feature vectors from the single trial responses depicted in feature plots (e.g. Figures 7.14 and 7.15) was to bring our estimation of physiologically interpretable parameter into a statistical classification framework. By statistical classification of different haemodynamic response types (shapes) it would be possible to distinguish and characterize neural information processing in different brain locations during a given paradigm. Each classified response could then give information about processing delay, number of neurons in the firing population and duration/asynchrony of firing at that particular brain location, and thus yield more information about functional anatomy than simple activation detection. We found that these plots are well suited for investigating different types of BOLD-responses. For visualization and easier interpretation, the different BOLD responses can be labeled and mapped to the corresponding anatomical images. To our knowledge findings in haemodynamic response features related to a word versus non-word discrimination task, as described in this work, have not been reported elsewhere. Such feature classification studies could therefore be an interesting follow up of the present signal description and estimation study.

Appendix A

Appendix

A.1 The convolution operator $\star$

In the signal processing litterature the symbol $\star$ is used for *convolution*, *mixed convolution*, and *discrete convolution*.

In case of $f, g : \mathbf{R} \mapsto \mathbf{R}$, the **convolution** $f \star g$ is defined as

$$(f \star g)(t) = \int_{-\infty}^{\infty} f(\tau) g(t - \tau)\, d\tau \qquad t \in \mathbf{R} \tag{A.1}$$

If $b = \{b_k\}_{k \in \mathbf{Z}}$ is a discrete sampled signal (i.e. a sequence) we define the **mixed convolution** $b \star f$ as

$$(b \star f)(t) = \sum_{k=-\infty}^{\infty} b(k) f(t - k) \qquad t \in \mathbf{R} \tag{A.2}$$

If $a = \{a_k\}_{k \in \mathbf{Z}}$ and $b = \{b_k\}_{k \in \mathbf{Z}}$ are discrete sampled signals, we define the **discrete convolution** $a \star b$ as

$$(a \star b)(m) = \sum_{k=-\infty}^{\infty} a(k) b(m - k) \qquad m \in \mathbf{Z} \tag{A.3}$$

In all cases we assume $f, g \in L_2(\mathbf{R})$, i.e. f and g are square-integrable real functions, and $a, b \in l_2$, i.e. a and b are square-summable discrete signals.

A.2 Fisher distribution

The F-distribution is given by

$$h(F) = \frac{\Gamma(\frac{v_1+v_2}{2})}{\Gamma(\frac{v_1}{2})\,\Gamma(\frac{v_2}{2})} \, (\frac{v_1}{v_2})^{\frac{v1}{2}} \, \frac{F^{\frac{v_1-2}{2}}}{(1 + \frac{F v_1}{v_2})^{\frac{v_1+v_2}{2}}}$$

where v_1 is the number of points per trial minus one, and v_2 is the total number of data points minus the number of points per trial. Γ is the gamma function in which

$$\Gamma(v) = \int_0^{+\infty} e^t t^{v-1} dt.$$

The F-distribution with various degrees of freedom in numerator and denominator is illustrated in Figure A.1.

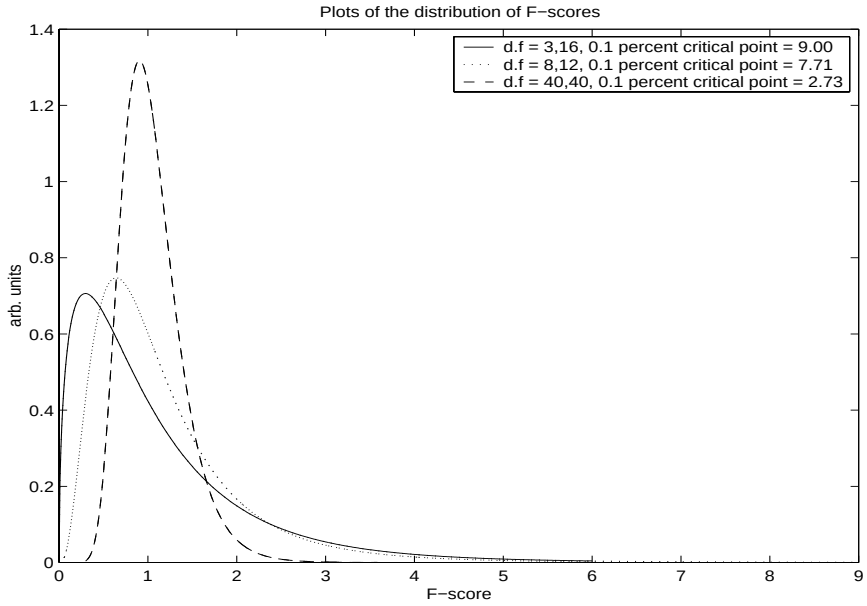

Figure A.1: F-distribution with various degrees of freedom in numerator and denominator. The 0.1% critical point (beyond which the null hypothesis is rejected) moves towards 1 as the degrees of freedom increase.

A.3 SPM99

The SPM (Statistical Parametric Mapping) software package is a suite of Matlab functions and subroutines (with some externally compiled C routines) which organizes and interprets functional neuroimaging data. Main features of the software are:

- Realignment of image sequences
- Automated non-linear spatial normalisation
- Image segmentation

- Coregistration
- Spatial smoothing
- Formation of statistic images
- Assessment of Statistic Images
- Interrogation of results (plots, local maxima, overlaying of statistical results onto structural images)
- Global adjustment and image averaging

Further information can be found at the SPM website: www.fil.ion.ucl.ac.uk/spm

A.4 Matlab functions [31]

- `chol`
  Cholesky factorization. `chol(X)` uses only the diagonal and upper triangle of X. The lower triangular is assumed to be the (complex conjugate) transpose of the upper. If X is positive definite, then `R = CHOL(X)` produces an upper triangular R so that $R' * R = X$. If X is not positive definite, an error message is printed.

- `fminsearch`
  Multi-dimensional unconstrained nonlinear minimization by Nelder & Mead downhill simplex method. Given an initial starting parameter vector `fminsearch` finds the minimum of a scalar function of several parameters. `X = fminsearch(FUN, X0, OPTIONS, P1, P2,...)` returns a vector X that is a local minimizer of the function that is described in FUN near the starting vector $X0$. FUN should return a scalar function value when called with feval: `F=feval(FUN,X)`. Optimization parameters are specified in the structure OPTIONS. Default values are used if an empty matrix is given for OPTIONS . P1,P2,... provides for additional arguments which are passed to the objective function, `F=feval(FUN,X,P1,P2,...)`.

- `jbtest`
  The Bera-Jarque test evaluates the hypothesis that X has a normal distribution with unspecified mean and variance, against the alternative that X does not have a normal distribution. The test is based on the sample skewness and kurtosis of X. The Jarque-Bera test is an asymptotic test, and should not be used with small samples. `H = jbtest(X,ALPHA)` determines if the null hypothesis of composite normality is a

reasonable assumption regarding the population distribution of a random sample X. The desired significance level, ALPHA, is an optional scalar input (default = 0.05). H indicates the Boolean result of the hypothesis test:

  - H = 0 $\Rightarrow$ Do not reject the null hypothesis at significance level ALPHA.
  - H = 1 $\Rightarrow$ Reject the null hypothesis at significance level ALPHA.

- `kron` Kronecker product. `kron (X,Y)` is the Kronecker product of X and Y. The result is a large matrix formed by taking all possible products between the elements of X and those of Y.

- `lillietest`
  The Lilliefors test evaluates the hypothesis that X has a normal distribution with unspecified mean and variance, against the alternative that X does not have a normal distribution. This test compares the empirical distribution of X with a normal distribution having the same mean and variance as X. It is similar to the Kolmogorov-Smirnov test, but it adjusts for the fact that the parameters of the normal distribution are estimated from X rather than specified in advance. [H,P] = `lillietest(X,ALPHA)` determines if the null hypothesis of composite normality is a reasonable assumption regarding the population distribution of a random sample X. The desired significance level, ALPHA, is an optional scalar input (default = 0.05). H indicates the result of the hypothesis test:

  - H = 0 $\Rightarrow$ Do not reject the null hypothesis at significance level ALPHA.
  - H = 1 $\Rightarrow$ Reject the null hypothesis at significance level ALPHA.

  P is computed via interpolation into the Lilliefors simulation table. A NaN is returned when P is not found within the interval $0.01 \leq \mathrm{P} \leq 0.20$.

- `lsqnonlin`
  Solves nonlinear least squares problems, including nonlinear data-fitting problems of the form $min\{\sum_x FUN(X)^2\}$ where X and the values returned by FUN can be vectors or matrices. `[X, RESNORM, RESIDUAL, EXITFLAG, OUTPUT] = lsqnonlin(FUN,` $X0$`, LB, UB, OPTIONS, P1, P2,..)` starts at the matrix $X0$ and finds a minimum X to the sum of squares of the functions in FUN. LB and UB defines a set of lower and upper bounds on the design parameters, X, so that the solution is in the range $\mathrm{LB} \leq X \leq \mathrm{UB}$. Optimization parameters are specified in the structure OPTIONS. Default values are used if an empty matrix is given for OPTIONS. P1,P2,... are

problem-dependent parameters and are passed directly to the function `FUN(X, P1, P2,...)`. RESNORM is the value of the squared 2-norm of the residual at X. RESIDUAL is the value of the residual at the solution X. EXITFLAG describes the exit condition of LSQNONLIN:

- EXITFLAG > 0 : LSQNONLIN converged to a solution X
- EXITFLAG $= 0$: the maximum number of function evaluations was reached.
- EXITFLAG < 0 : LSQNONLIN did not converge to a solution.

The structure OUTPUT returns the number of iterations taken in OUTPUT.iterations, the number of function evaluations in OUTPUT.funcCount and the algorithm used in OUTPUT.algorithm.

- `nlinfit`
  Nonlinear least-squares data fitting by the Gauss-Newton method. `nlinfit(t, g, 'MODEL', theta0)` finds the coefficients of the nonlinear function described in MODEL. MODEL is a user supplied function having the form `g = fun(theta,t)`. That is MODEL returns the predicted values of $g$given initial parameter estimates, beta, and the independent variable, t. `[theta, res, jac] = nlinfit(t, g, 'MODEL', theta0)` returns the fitted coefficients theta, the residuals, res, and the Jacobian matrix, jac, at the solution.

- `nlparci`
  Computes confidence intervals on parameters of nonlinear models. `ci = nlparci(X, res, jac)` returns the 95% confidence interval ci on the nonlinear least squares parameter estimate X, given the residual sum of squares, res, and the Jacobian matrix ,jac, at the solution. The confidence interval calculation is valid for systems where the number of rows of J exceeds the length of X.

A.5 Frequently used Abbreviations

2D,3D	{one, two, three}-dimensional
ANOVA	ANalysis Of VAriance
BOLD	Blood Oxygenation Level Dependent
Dispersion	Duration of BOLD-response
EPI	Echo Planar Imaging
er-fMRI	event-related functional Magnetic Resonance Imaging
FLASH	Fast Low-Angle SHot
fMRI	functional Magnetic Resonance Imaging
FOV	Field of View
Gain	Gain/strength of BOLD response / number of neurons in firing population
HRF	Haemodynamic Response Function
Lag	Time to peak / maximum intensity of BOLD response
LM	Levenberg-Marquardt Method
MRI	Magnetic Resonance Imaging
NM	Nelder & Mead downhill simplex method
Pixel	Picture Element
ROI	Region Of Intrest
SNR	Signal to Noise Ratio
SPM	Statistical Parametric Mapping (see Appendix A.3)
TE	Echo Time
TR	Repetition Time
Voxel	Volume element

Bibliography

[1] J. Ashburner and K. J. Friston. *Image Registration*, chapter 26, pages 285–299. In [35], 1999.

[2] P. A. Bandettini. *The Temporal Resolution of Functional MRI*, chapter 19, pages 205–220. In [35], 1999.

[3] J. Belliveau, D. N. Kennedy, R. C. McKinstry, B. R. Buchbinder, R. M. Weisskoff, M. Cohen, J. M. Vevea, T. J. Brady, and B. R. Rosen. Functional mapping of the human visual cortex by magnetic resonance imaging. *Science*, 254:716–719, 1991.

[4] F. Bloch. Nuclear induction. *The Physical Review*, 70:460–474, 1946.

[5] G. M. Boynton, S. A. Engel, G. H. Glover, and D. J. Heeger. Linear systems analysis of functional magnetic resonance imaging in human v1. *The Journal of Neuroscience*, 16:4207–4221, 1996.

[6] R. L. Buckner. Event-related fMRI and the hemodynamic response. *Human Brain Mapping*, 6:373–377, 1998.

[7] R. L. Buckner and T. S. Braver. *Event-Related Functional MRI*, chapter 36, pages 441–452. In [35], 1999.

[8] M. A. Burock and A. M. Dale. Estimation and detection of event-related fMRI signals with temporally correlated noise: A statistical efficient and unbiased approach. *Human Brain Mapping*, 11:249–260, 2000.

[9] R. B. Buxton, E. C. Wong, and L. R. Frank. Dynamics of blood flow and oxygenation changes during brain activation: The ballon model. *Magnetic Resonance in Medicine*, 39:855–864, 1998.

[10] R. B. Buxton, E. C. Wong, and L. R. Frank. *The Post-Stimulus Undershoot of the Functional MRI Signal*, chapter 23, pages 253–262. In [35], 1999.

[11] V. Calhoun, T. Adali, M. Kraut, and G. Pearson. A weighted least-squares algoritm for estimation and visualization of relative latencies in event-related functional MRI. *Magnetic Resonance in Medicine*, 44:947–954, 2000.

[12] S. Clare. *Functional MRI : Methods and Applications*. PhD thesis, Oxford University, 1997.

[13] S. Clare, M. Humberstone, J. Hykin, L. D. Blumhardt, R. Bowtell, and P. Morris. Detecting activations in event-related fMRI using analysis of variance. *Magnetic Resonance in Medicine*, 42:1117–1122, 1999.

[14] A. Dale and R. Buckner. Selective averaging of rapidly presented individual trials using fMRI. *Human Brain Mapping*, 5:329–340, 1997.

[15] A. M. Dale and M. I. Sereno. Improved localization of cortical activity by combining EEG and MEG with MRI cortical surface reconstruction: A linear approach. *Journal of Cognitive Neuroscience*, 5:162–176, 1993.

[16] E. A. DeYoe, P. Bandettini, J. Neitz, D. Miller, and P. Winans. Functional magnetic resonance imaging (FMRI) of the human brain. *The Journal of Neuroscience*, 54:171–187, 1994.

[17] K. J. Friston, P. Fletcher, O. Josephs, A. Holmes, M. D. Rugg, and R. Turner. Event-related fMRI: Characterizing differential responses. *NeuroImage*, 7:30–40, 1998.

[18] K. J. Friston, P. Jezzard, and R. Turner. Analysis of functional MRI time-series. *Human Brain Mapping*, 1:153–171, 1994.

[19] A. Gade. *Hjerneprocesser*. Frydenlund Grafisk, København, 1997.

[20] N. Gershenfeld. *The Nature of Mathematical Modeling*. Cambridge Univerity Press, 1999.

[21] R. H. Hashemi and W. G. Bradley. *MRI:The basics*. Lippincott, Williams & Wilkins, 1997.

[22] G. Hathout, B. Varjavand, and R. K. Gopi. The early response in fMRI: A modelling approach. *Magnetic Resonance in Medicine*, 41:550–554, 1999.

[23] R. E. Hendrick. *Image Contrast and Noise*, chapter 4, pages 43–67. Volume 1 of [41], 1999.

[24] A. M. Howseman and R. W. Bowtell. Functional magnetic resonance imaging : Imaging techniques and contrast mechanisms. *Phil. Trans. R Soc. Lond.*, 354:1179–1194, 1999.

[25] O. Josephs and R. N. A. Henson. Event-related functional magnetic resonance imaging : modelling, inference and optimization. *Phil. Trans. R Soc. Lond.*, 354:1215–1228, 1999.

[26] O. Josephs, R. Turner, and K. Friston. Event-related fMRI. *Human Brain Mapping*, 5:243–248, 1997.

[27] F. Kruggel and D. Y. von Cramon. Modeling the hemodynamic response in single-trial functional MRI experiments. *Magnetic Resonance in Medicine*, 42:787–797, 1999.

[28] F. Kruggel and D. Y. von Cramon. Physiological oriented models of the hemodynamic response in functional MRI. *Lecture Notes in Computer Science*, 1613:294–307, 1999.

[29] F. Kruggel and D. Y. von Cramon. Temporal properties of the hemodynamic response in functional MRI. *Human Brain Mapping*, 8:259–271, 1999.

[30] G. Lohmann. *Volumetric Image Analysis*. Wiley and Teubner, 1998.

[31] Mathworks. Statistic toolbox. Web.

[32] R. S. Menon and S. G. Kim. Spatial and temporal limits in cognitive neuroimaging with fMRI. *Elsevier science*, 3:207–216, 1999.

[33] K. Miller. Modelling the bold signal: Application of the balloon model to experimental fMRI data. Web, 1998.

[34] B. J. Mock, M. J. Lowe, and P. A. Turski. *Functional Magnetic Resonance Imaging*, volume 3, chapter 70, pages 1555–1574. Mosby, St. Louis,Missouri, 1999.

[35] C. Moonen and P. A. Bandettini. *Functional MRI*. Springer, Berlin,Germany, 1999.

[36] T. B. Parrish, D. R. Gitelman, K. S. LaBar, and M. M. Mesulam. Modelling hemodynamic response for analysis of functional MRI time-series. *Magnetic Resonance in Medicine*, 44:925–932, 2000.

[37] L. Pauling and C. Coryell. The magnetic properties and structures of hemoglobin. *Proc. Natl. Acad. Sci. USA*, 22:210–216, 1936.

[38] S. Pollmann, A. Dove, D. Y. von Cramon, and C. J. Wiggins. Event-related fMRI: Comparison of conditions with varying bold overlap. *Human Brain Mapping*, 9:26–37, 2000.

[39] J. C. Rajapakse, F. Kruggel, J. M. Maisog, and D. Y. von Cramon. Modelling hemodynamic response for analysis of functional MRI time-series. *Human Brain Mapping*, 6:283–300, 1998.

[40] A. Rosenfeld and C. K. Avinash. *Digital Picture Processing*, volume 1. Academic Press, 1982.

[41] D. D. Stark and W. G. Bradley JR. *Magnetic Resonance Imaging*, volume 1. Mosby, St. Louis,Missouri, 1999.

[42] J. Talairach and P. Tournoux. *Coplanar stereotaxic atlas of the human brain.* Thieme Medical, New York, 1988.

[43] C. Westbrook and C. Kaut. *MRI in practice, second edition.* Blackwell Science Ltd., London, United Kingdom, 1998.

[44] T. H. Wonnacott and F. R. Wonnacott. *Introductory Statistics, third edition.* John Wiley & Sons, Inc., New York, New York, 1977.

[45] M. L. Wood and R. M. Henkelman. *Artifacts*, chapter 10, pages 215–230. Volume 1 of [41], 1999.

[46] R. P. Woods, S. T. Grafton, C. J. Holmes, S. R. Cherry, and J. C. Mazziotta. Automated image registration: I. general methods and intrasubject, intramodality validation. *Journal of Computer Assisted Tomography*, 22(1):139–152, 1998.